

# Pattern Collapse

The Mechanical Stability and Solid Bridging of  
Semiconductor Nanostructures

Dissertation

zur Erlangung des Doktorgrades

der Mathematisch-Naturwissenschaftlichen Fakultät

der Christian-Albrechts-Universität zu Kiel

vorgelegt von

**Daniel Peter**

aus Laufenthal

Villach, 2010

---

Referent: Prof. Dr. Bensch

Korreferent: Prof. Dr. Kienle

Tag der Prüfung: 12.11.2010

Zum Druck genehmigt: 12.11.2010

---

# Erklärung

Hiermit erkläre ich daß ich die vorliegende Arbeit selbstständig und nur mit den angegebenen Hilfsmitteln angefertigt habe und erstmalig im Rahmen eines Prüfungsverfahrens vorgelegt wird. Die Arbeit ist nach Inhalt und Form abgesehen von der Beratung durch den Betreuer meine eigene Arbeit welche unter Einhaltung der Regeln guter wissenschaftlicher Praxis der Deutschen Forschungsgemeinschaft entstanden ist. Dies ist mein erster Promotionsversuch.

Villach den 09.09.2010

Daniel Peter

# Contents

Erklärung .....	iii
Contents .....	iv
Acknowledgements .....	vii
Abstract .....	ix
Zusammenfassung .....	x
List of Symbols .....	xi
Abbreviations .....	xi
Formula Symbols .....	xii
I Introduction.....	1
1.1 Background .....	1
1.2 Semiconductor history & Moore's law.....	3
1.3 Semiconductor Devices.....	7
1.4 Semiconductor Structures with High Aspect Ratios.....	9
1.4.1 DRAM Capacitors .....	9
1.4.2 Shallow Trench Isolation Structures.....	11
1.4.3 MEMS Structures.....	13
1.5 Wet Surface Processing of Silicon Wafers .....	14
1.6 Pattern Collapse .....	16
1.6.1 Definition and Standard Surface Tension Model.....	16
1.6.2 Pattern Collapse for MEMS Devices.....	18



---

1.6.3	Concepts for Prevention of Pattern Collapse in Microelectronics.....	19
1.6.4	Pattern Collapse Theories Other than Surface Tension.....	20
II	Theory .....	23
2.1	Forces at the Nanoscale during Drying .....	23
2.1.1	van der Waals Forces .....	23
2.1.2	Hydrogen Bonding .....	24
2.1.3	Solid Bridging.....	24
2.1.4	Electrostatic Forces .....	24
2.1.5	Centrifugal Forces.....	25
2.1.6	Capillary Force.....	26
2.1.7	Evaluation of the Forces .....	28
2.2	Beam Sway Models.....	31
2.2.1	Analytical Model.....	31
2.2.2	Stress Analysis .....	33
2.2.3	Pattern Collapse Analysis .....	34
III	Methods.....	36
3.1	Materials.....	36
3.1.1	Semiconductor Line Structures (ASAP 300) .....	36
3.1.2	AFM Tips and Experimental Setup .....	38
3.1.3	Silicon Nanoparticles and Preparation Methods .....	39
3.1.4	Chemicals .....	40
3.2	Analytical Techniques.....	42
3.2.1	Lateral Force Microscopy.....	42
3.2.2	Transmission Electron Microscopy .....	48
3.2.3	X-ray Photoelectron Spectroscopy (XPS) .....	50
3.2.4	Nuclear Magnetic Resonance Spectroscopy .....	50
3.2.5	Electro Spray Ionization – Mass Spectrometry .....	50
3.2.6	Analytical Equipment .....	51

---

IV	Results and Discussion .....	52
4.1	Pattern Collapse by AFM.....	53
4.2	Fracture Strength of Polysilicon in Nanostructures.....	62
4.3	Influence of the Chemicals Used for Semiconductor Drying on the Mechanical Stability of Nanostructures .....	72
4.4	Influence of the Bulk Liquid Media vs. the Solid-Liquid Interface.....	82
4.5	Influence of Alcohols and the Solid-Liquid Interface .....	92
4.6	Solid Bridging Studied with Silicon Nanoparticles .....	97
V	Conclusions and Outlook.....	104
	List of Figures .....	108
	Bibliography .....	111
	Curriculum Vitae .....	123

## Acknowledgements

First of all I would like to thank the company SEZ AG for initiating this PhD thesis and Lam Research Corporation for their continued and great support after the acquisition of SEZ AG.

I wish to thank my PhD advisor, Prof. Dr. Wolfgang Bensch, for his interest in this topic and his guidance especially for the experiments with the nanoparticles. For the examination of and his interest in this thesis, I would like to thank the co-referent Prof. Dr. Kienle. Additionally, I would like to thank him and Andriy Lotnyk for his great support with TEM analyses.

I am very grateful for the support and advice of Prof. Dr. Alfred Lechner, who initiated and promoted this thesis throughout its development. I would like to thank his team for the help with the experiments at the University of Applied Sciences Regensburg.

I would like to express my appreciation and gratitude to my company advisor, Dr. Michael Dalmer. Despite his full calendar, he always found some time to discuss the latest results with me. I am especially grateful that he allowed me to concentrate on my experiments. A big word of thanks goes to Hans Kruwinus for giving me the chance to work on this topic. Our fruitful discussions always resulted in new ideas.

In this place, I would like to thank Prof. Dr. Robert Stark and Dr. Alexander Gigler for the collaboration with the AFM measurements in liquid media. Especially, I would like to say thank you for the good discussions and the smooth collaboration with the whole group at the LMU Munich.

Furthermore, the support of the Institute for Electron Microscopy FELMI, Graz University of Technology in Graz, for TEM images is acknowledged. For the

numerous SEM images, I would like to thank Birgit Orel and Gale Hansen of SEZ / Lam Research who showed me the tricks of SEMing.

Without the careful proofreading and the competent comments of Christine Cyterski and Elizabeth Pavel, my thesis would not read as smoothly as it does now.

I owe big thanks to my co-worker PhD Glenn Gale for his comments on pattern collapse, especially in regards to current developments in the industry. For the great discussions on countless topics and support, I would like to thank PhD Harald Okorn-Schmidt and PhD Frank Holsteys.

Of course I do not want to forget to address my best regards to all current and former process members at Lam Research (SEZ). I enjoyed the great working atmosphere and the collaboration with all the team members. A special word of thanks goes also to Stefanie Preumel for the countless travel requests.

I would also like to thank my co-workers at the CAU Kiel, especially Bastian Dietl and Nicole Pienack for their input and help with the XRD experiments. I would like to express my appreciation for your patience with my poor "Hochdeutsch".

Last but not least, I would like to thank my parents and my sister for supporting me through my education and this thesis. It was always great to be able to come home.

Finally, I want to say "A herzlichs Vergelt's Gott" to all who supported me during my PhD thesis.

## Abstract

Pattern collapse is a damage phenomenon during the production of microelectronic devices. High aspect ratio structures like shallow trench isolation and capacitor-over-bitline are the most vulnerable patterns. The damage has a distinctive shape, where the tops of the structures are connected together with their neighbors either by rupture or bending. Normally, this issue is attributed to surface tension forces during the drying step of a wet clean process; however, in the past several years other influences have been discussed like an increased chemical reactivity of the nanoscale structures.

For the evaluation of these concepts, the measurement of the mechanical stability of the nanostructures was necessary which was hitherto only calculated. Sub-50 nm polysilicon line structures were measured with atomic force microscopy (AFM). The forces were in the range of several  $\mu\text{N}$ , depending on their line width. As the pattern collapse phenomenon happens when the structures are exposed to liquid media, the respective influence of the media was studied. The fracture force was found to be influenced by the solid-liquid interface, as much as an increase by 100 %. In contrast, the conchoidal damage was influenced by the viscosity, i.e., by the bulk of the liquid.

For very high aspect ratios, the structures become more vulnerable to pattern collapse via elastic bending. Permanent damage occurs only when the tops of the structures stick to each other. The concept of solid bridging, where dissolved material in the liquid accumulates between the structures and acts like an adhesive, was studied with silicon nanoparticles. Significant bridges of silicon oxide were observed for evaporative drying. In order to avoid pattern collapse, this formation of bridges, which was attributed to silicates, needs to be prevented.

## Zusammenfassung

Während der Produktion mikroelektronischer Bauteile kann das Phänomen „pattern collapse“ zu Defekten führen. Am meisten gefährdet sind Strukturen mit hohem Aspektverhältnis. Der charakteristische Schaden ist durch den Kontakt der Spitzen von benachbarten Strukturen, durch Verbiegung oder Bruch gekennzeichnet. Normalerweise werden Oberflächenspannungskräfte dafür verantwortlich gemacht, die während eines Trocknungsschritts nach einer naßchemischen Reinigung auftreten. Jedoch sind in den letzten Jahren auch andere Einflüsse wie die erhöhte chemische Reaktivität von Nanostrukturen diskutiert worden.

Für die Bewertung der alternativen Konzepte ist die Bestimmung der mechanischen Belastbarkeit der Nanostrukturen unerlässlich welche vorher nur theoretisch berechnet wurde. Polysiliziumstrukturen mit einer Breite von weniger als 50 nm wurden dazu mit dem Rasterkraftmikroskop vermessen. Die Kräfte befanden sich abhängig von der Linienbreite im Bereich von einigen  $\mu\text{N}$ . Eine veränderte festflüssig Grenzschicht konnte die Bruchkraft um bis zu 100 % erhöhen. Im Gegensatz dazu wurde die Größe der muschelähnlichen Bruchstücke durch die Viskosität, also einer Eigenschaft des Volumens der Flüssigkeit bestimmt.

Mit zunehmenden Aspektverhältnissen werden die Strukturen immer anfälliger für „pattern collapse“ durch elastische Verbiegung der Strukturen. Bleibende Schäden entstehen hierbei nur, wenn die Enden der Strukturen zusammenkleben. Die Theorie des „solid bridging“, wobei sich Silikate zwischen den Strukturen ansammeln und wie ein Kleber wirken, wurde mit Siliziumnanopartikeln untersucht. Signifikante Verwachsungen aus Siliziumdioxid sind beim Verdampfungstrocknen entstanden. Für das Verhindern von „pattern collapse“ ist es wichtig diesen Prozess der Silikaten zugeordnet wird zu unterdrücken.

# List of Symbols

## Abbreviations

AFM	Atomic force microscopy/atomic force microscope
CAPB	Cocamidopropyl betaine
CMC	Critical micelle concentration
CMOS	Complementary metal oxide semiconductor
CTAB	Cetyltrimethylammonium bromide
CVD	Chemical vapor deposition
DIW	De-ionized water
DRAM	Dynamic random access memory
EDX	Energy dispersive X-ray spectroscopy
EELS	Electron energy loss spectroscopy
EFTEM	Energy filtered transmission electron spectroscopy
ESI-MS	Electro spray ionization mass spectroscopy
FEA	Finite element analysis
FET	Field effect transistor
FIB	Focused ion beam
FinFET	Multiple gate transistor with a fin shaped source-drain path
FTIR	Fourier transformed infrared spectroscopy
HFE	Hydrofluoroether
HRTEM	High resolution transmission electron microscopy
HSG	Hemispherical silicon grain
IPA	Isopropanol/isopropyl alcohol
ITRS	International Technology Roadmap for Semiconductors
LFM	Lateral force microscopy/lateral force microscope
LOCOS	Local oxidation of silicon
MAS NMR	Magic angle spinning nuclear magnet resonance
MEMS	Micro-electro mechanical systems

MESH	Mechanically enhanced storage node height
MOSFET	Metal oxide semiconductor field effect transistor
n.a.	Not applicable
NMR	Nuclear magnet resonance
RCA	Radio Cooperation of America
S30	Sucrose mixed with de-ionized water at 30%w sucrose
S40	Sucrose mixed with de-ionized water at 40%w sucrose
SC1	Standard Clean 1 of RCA cleaning sequence
SC2	Standard Clean 2 of RCA cleaning sequence
SEM	Scanning electron microscope
STI	Shallow trench isolation
TEM	Transmission electron microscope
vdW	van der Waals
XPS	X-ray photoelectron spectroscopy
XRD	X-ray powder diffraction

## Formula Symbols

$\alpha$	Angle to the centerline introduced by the off center tip position
$\alpha_{con}$	Contact angle
$A_{cap}$	Area of the plates of a capacitor
$A$	Area
$A_{Ham}$	Hamaker constant
$\beta_i$	Angle of the surface
$\Gamma_i^f$	Imaginary part of the hydrodynamic function
$C_{cap}$	Capacity of a parallel plate capacitor
$\delta_{one}$	Displacement by one end load
$d_{dis}$	Displacement by distributed load
$d$	Distance between two surfaces
$d_A$	Distance A between structures
$d_B$	Distance B between structures
$d_{ox}$	Insulator thickness between the capacitor plates
$\Delta D$	Signal offset due to detector misalignment
$\Delta L_i$	Slope of lateral force distance curve in contact regime
$\Delta L_i^A$	Slope of lateral force distance curve in contact regime (approach)
$\Delta L_i^R$	Slope of lateral force distance curve in contact regime (retract)



---

$\Delta p_{Cap}$	Capillary pressure
$\Delta p_{dis}$	Distributed (area) load
$\varepsilon_0$	Vacuum permittivity
$\varepsilon_R$	Relative permittivity
$E$	Young's modulus
$f_{CapF}$	Area-specific capillary force with different filling heights
$f_{cen_1}$	Area-specific centrifugal force on the structure
$f_{cen_2}$	Area-specific centrifugal force on the structure with liquid
$f_{el}$	Area-specific electrostatic force
$f_{vdW}$	Area-specific force due to van der Waals interaction
$F_{Cap}$	Capillary force
$F_{CapF}$	Capillary force due to different filling heights
$F_{CapS}$	Capillary force due to different spacing
$F_{cen}$	Centrifugal force
$F_{el}$	Electrostatic force
$F_{one}$	One end load
$F_{vdW}$	Force due to van der Waals interaction
$F_{ST_x}$	Surface tension force component perpendicular to the structure
$\gamma_l$	Surface tension
$G$	Shear modulus
$I$	Moment of inertia
$l$	Length of the structure
$l_{line}$	Length of line structure
$L_{Cap}$	Length of a parallel plate capacitor
$L_{Can}$	Length of AFM cantilever
$\eta_{kin}$	Kinematic viscosity
$\eta_{vis}$	Viscosity
$h$	Height of the structure
$h_{line}$	Height of line structure
$h_A$	Difference in filling height
$h_B$	Filling height
$h_{Cap}$	Height of a parallel plate capacitor
$h_{Tip}$	Height of AFM tip
$k_N$	Normal spring constant of AFM cantilever
$\mu$	Friction coefficient
$\mu_{Di}$	Dipole moment

---

$m$	Mass of the body
$m_1$	Mass of the structure
$m_2$	Combined mass of body and liquid
$m_l$	Mass of liquid
$n$	Rotational speed
$p/p_0$	Relative vapor pressure
$Q_f$	Quality factor
$\rho_l$	Density of liquid
$\rho_{Si}$	Density of silicon
$r$	Radius
$r_{\parallel}$	Meniscus radius parallel to a line structure
$r_{\perp}$	Meniscus radius perpendicular to a line structure
$R$	Gas constant
$S_{lat}$	Lateral force constant determined by direct force balance
$S_{lat_u}$	Lateral force constant determined by updated direct force balance
$t_{Can}$	Thickness of AFM cantilever
$T$	Temperature
$v_{sound}$	Speed of sound
$V$	Voltage difference
$V_m$	Molar volume
$\omega$	Angular frequency
$\omega_f$	Resonant frequency of the fundamental resonance peak
$w$	Width of the structure
$w_l$	Width of liquid
$w_{line}$	Width of line structure
$w_{vdW}$	Area-specific van der Waals interaction energy
$w_{Can}$	Width of AFM cantilever
$W_{vdW}$	van der Waals interaction energy

# I Introduction

## 1.1 Background

The focus of the present PhD thesis is one of the most important steps in the semiconductor manufacturing processes: cleaning after dry etch and release of the structures by wet etch. Cleaning procedures become more important with shrinking size of the structures of the devices, and currently about 30 % of the overall process steps in the production of the silicon chip are related to cleaning. The first semiconductor devices contained structures in the sub-millimeter range. Obviously the ratio of the surface to bulk of these structures was low, and therefore, surface chemical reactions could more or less be neglected. During the last decades, the dimensions of the structures on typical semiconductor devices have significantly decreased. Today, structures as small as 20 nm in width with topography of 400 nm are found in silicon based devices. In addition, very thin layers of less than 5 nm become common for diffusion barriers or gate oxides. Thus, the aspect ratio of (surface to bulk) has significantly changed towards the surface, i.e., the surface chemical reactions are much more important.

During the production of silicon chips, a large variety of processes are utilized. Production procedures include vapor deposition for thin film creation, plasma and wet chemistry etching for film removal and pattern transfer, chemical mechanical polishing for planarization of the wafer, and ion implantation for doping of the semiconductor. A wide range of chemicals are used for these processes. Deposition and plasma etch processes use gases like silane and HBr. Wet etching and cleaning processes use potassium hydroxide solutions, solvents, and hydrofluoric acid. The process conditions are very diverse in temperature and pressure. Cleaning applications are usually done at room temperature up to 65 °C, while temperatures

up to more than 1000°C are used in oxidation and deposition processes. Pressure ranges from high vacuum in deposition and plasma processes to atmospheric conditions in annealing processes and wet cleaning. Additionally, wet chemistries are utilized for material-specific etching, such as diluted hydrofluoric acid for silicon oxide, ammonia for silicon, and H<sub>2</sub>SO<sub>4</sub> for photoresists. For the removal of photoresists from devices with high-k/metal gates solvents are required because H<sub>2</sub>SO<sub>4</sub> would remove the gate as well. Obviously, the chemical reactions inherent in these processes vary with the conditions and the corresponding chemistries.

A state-of-the-art semiconductor product can require around 300 process steps. As the size of the individual structures and layers decreases to the nanometer range, the interaction between the steps is large and partially not well understood. Additionally, only the electrical testing of the final product gives reliable data, whether all of the devices on a wafer are working properly. Furthermore, as the production of a device can take up to two months the respective data are usually not immediately available. For the case of defective devices, a detailed failure analysis is necessary. Root cause analysis can be very demanding if two or more processes interacted with each other.

The combination of process complexity with the long response times makes a detailed understanding of the processes and their interactions very valuable. In order to ensure a high percentage of working devices on a wafer, a good control over these processes is necessary. However, because of the enormous complexity, a trial and error approach based on the experiences of the manufacturers is employed in the semiconductor industry. The result of this approach is that issues that seemed to be solved are resurfacing again some years later with smaller technology sizes.

One of these issues is pattern collapse which has been known in the industry for more than 20 years for photoresist structures and for more than 10 years on capacitor devices. Some research has been done but the issue was mainly solved by optimizing some process parameters which eliminated the immediate problem for a time. The understanding of the phenomena is still basic so that when the issue appears again, as is happening today, the search for a solution of the problem starts again. In order to overcome this cycle, a research project was started with this PhD thesis to study the fundamentals behind the pattern collapse phenomena. The

knowledge gained in this thesis shall be used later as input for the design of a pattern collapse free semiconductor process cycle.

For a better understanding of the motivation of the work performed during the PhD thesis, a brief overview of the history of the transistor development is given and is continued by a detailed discussion of miniaturization trends. A more specific description of the relevant semiconductor products and the affected structures is presented in the subsequent sections. The need for cleaning with liquid chemistry and the resulting issue of pattern collapse with the corresponding models and prevention approaches are discussed at the end of this chapter.

## **1.2 Semiconductor history & Moore's law**

The transistor was invented by Shockley, Bardeen, and Brattain at Bell labs in 1947. The first transistor used two metal electrodes on a base of p-type germanium in a bipolar operation principle. P-type means that the holes are the majority carriers instead of the electrons, as in an n-type device or in a conductor. A bipolar transistor consists of three areas: the middle is the base and the two surrounding areas are the emitter and collector, which have opposite majority carriers compared to the base. The operation principle is that the electrical resistance between the emitter and collector can be controlled by the concentration of the minority carriers in the base, hence, the name transistor (from transfer-resistor).

Ge as base material has a bandgap of only 0.2 eV and is therefore prone to thermal runaway, i.e., the intrinsic charge carrier concentration exceeds the dopant concentration for Ge slightly above room temperature. The high density of intrinsic carriers reduces the transistor to a simple Ge resistor, which causes failure of the electrical circuit. Such effects can be minimized by using silicon, which has a bandgap of 1.1 eV. Transistors made of silicon became available only after impurities in the material could be sufficiently decreased to less than one part per billion by H. Theurerer with the zone refining process [1].

The design of the first commercial transistor was based on the Mesa design (Figure I.1), which had the disadvantage of sensitivity to particles on the exposed base/collector surface. Typically, such particles caused the electrical failure of the entire device. Therefore, the regions needed to be clean, already demonstrating the importance of cleaning procedures at the early stages of the semiconductor industry.

The introduction of the planar technology by Fairchild Semiconductor [2] in 1959 decreased the sensitivity to particles on the finished product because the interfaces inside the device were buried. The planar transistor, combined with thin film metal wiring allowed the design and manufacture of the first real integrated circuit (IC). An integrated circuit combines transistors, resistors, and capacitors to an electrical circuit on the same monolithic material, i.e., the silicon chip.

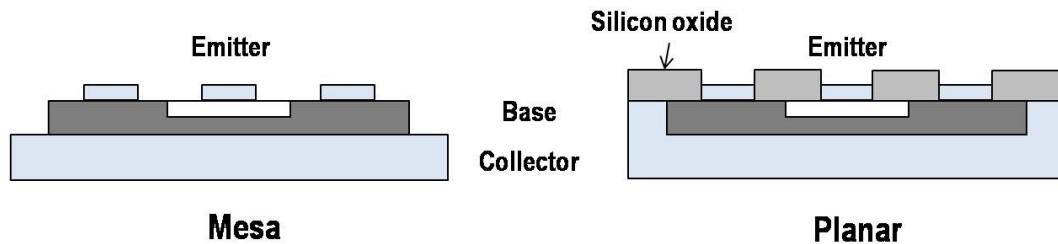


**Figure I.1 Simplified cross-section through early bipolar transistor geometries. Original drawings published by Riordan [1].**

The bipolar transistor was an intermediate discovery because the original goal was the production of a field effect transistor (FET) anticipated by Lilienfeld in 1926 [3]. The first such devices were obtained in the 1950s (by Weimer [4]), but these were very unstable. At that time it was not understood that metal contamination – especially sodium close to the gate – was significantly deteriorating device performance.

In the 1970s, the fundamental knowledge and efficient metal control led to the introduction of the metal oxide semiconductor field effect transistor (MOSFET) by Kang and Atalla from Fairchild [5]. The transistor was based on an aluminum gate (metal) with a silicon oxide (oxide) on a silicon substrate (semiconductor). Only one carrier type is used for the operation of a field effect transistor. This is achieved by applying an electrical field to the gate, which inverts the channel beneath the oxide from the majority carrier type to the minority carrier type. As the major carrier type of the channel turns into the same as in the source and drain region, the path between source and drain becomes conductive. The MOSFET has the advantage of high input impedance similar to a vacuum tube, instead of the low impedance of a bipolar transistor.

In 1967, Wanlass developed the complementary metal oxide semiconductor (CMOS) technology, which incorporates both n-type and p-type FET transistors [6]. The

CMOS offers far lower power consumption because it requires power only during switching the transistor from the on state to the off state or vice versa and none during static operation. During the 1980s, the CMOS became the dominant device design, which changed little in the subsequent 30 years, although the overall size decreased dramatically. The first commercial microprocessor (Intel® 4004) utilized structure sizes of 10  $\mu\text{m}$  [7], which was reduced to 32 nm in 2010. The reduction in size of the individual structures in a single chip allowed an ever increasing packaging density of transistors (Figure I.2).

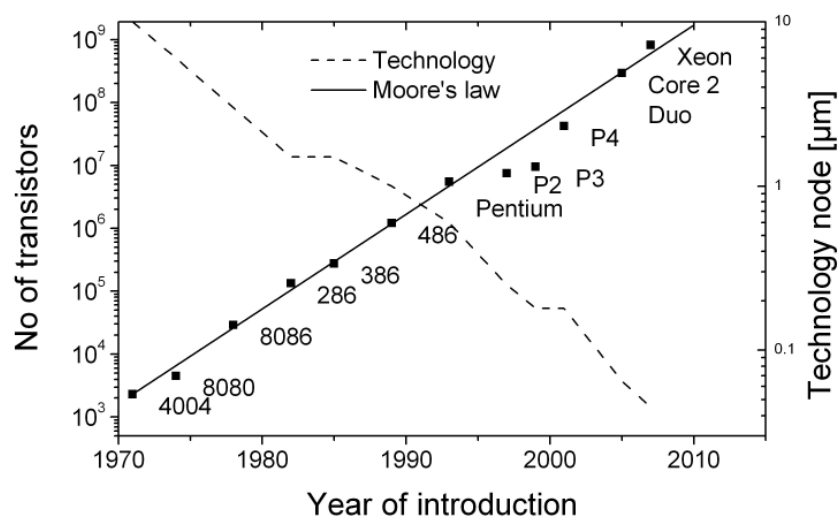


**Figure I.2 Historic review of Moore's Law (transistor count doubling every two years) with Intel® products and the corresponding technology sizes (node) [8].**

The increasing number of transistors on a single chip was accurately predicted by Gordon Moore (co-founder of Intel) in 1965 [9]. According to his prediction, the number of transistors on a single chip is doubled every eighteen months. Ten years later, Moore updated the 'law' to doubling of the transistor count every two years [10]. Starting from a mere 60 transistors on an IC in 1965, a state-of-the-art processor in 2010 contains around 1 billion transistors. Up until now, the prediction has been accurate (Figure I.2), [11] and became known as "Moore's Law" in the semiconductor industry. Besides the higher transistor density, the main advantages of the miniaturization are the shortened distance to the neighboring transistors and the reduced gate capacity, both increasing the speed of the IC and reducing the power consumption of the chip. Additionally, the smaller the IC, the more chips fit on a single wafer and production cost per chip is reduced, thus, increasing profitability.

For the characterization of the chip technology, the smallest feature size determined by photolithography is used and is called the technology node. The requirements to maintain Moore's Law are described in the "International Technology Roadmap for Semiconductors" [12]. An industry-wide collaboration creates the road-map in order to synchronize the development of devices between the semiconductor manufacturers and equipment suppliers. The ITRS roadmap specifies, for example, the acceptable contamination levels for metals and the critical particle size for the cleaning processes. Because the industry is using Moore's Law as the base for its operation planning, some researchers consider it a self-fulfilling prophecy.

The question of the end of Moore's Law has been raised by many (including Gordon Moore himself) and especially in combination with seemingly insurmountable barriers, e.g. using photolithography for structures smaller than the half of the incident wavelength or gate oxide thickness smaller than 0.5 nm [13]. Currently, structures as small as 20 nm are developed using 193 nm photolithography with the help of phase shift masks [14], immersion lithography [15], and double patterning techniques [16]. The barrier of unacceptable thermal noise created by the thin gate oxide has been resolved by using oxides with a higher dielectric constant than silicon oxide in order to provide the same electrical characteristics with a lower leakage current [17]. This example demonstrates the necessity for the introduction of new materials in order to overcome technology road-blocks. Further examples are the usage of Ge or SiGe alloys for higher electron and hole mobilities in the source-drain area and the use of TiN and Ru for DRAM (dynamic random access memory) capacitor electrodes [12]. Thus, it is believed that Moore's Law will continue to remain valid for several years.



### 1.3 Semiconductor Devices

In addition to the logic products like microprocessors mentioned in the previous section, there is the large sector of solid state memory chips which can be divided into volatile and non-volatile categories.

Volatile memory is dominated by DRAM for PCs and notebooks. The main purpose of the memory is to store binary information with rapid access to the microprocessor for further processing. Therefore, the DRAM cells are built into a matrix so that every single bit can be randomly accessed. In 1968, R. H. Dennard invented the principal design of a single DRAM cell, which consists of a capacitor for storing the information and a transistor for accessing [18] (Figure I.3). The capacitor design makes it necessary to refresh the information/electrical charge within the retention time of 64 ms [12], otherwise the information is lost. An overview of DRAM technology and challenges has been given by Faul et al. (Infineon/Qimonda) [19] and Kim (Samsung) [20].

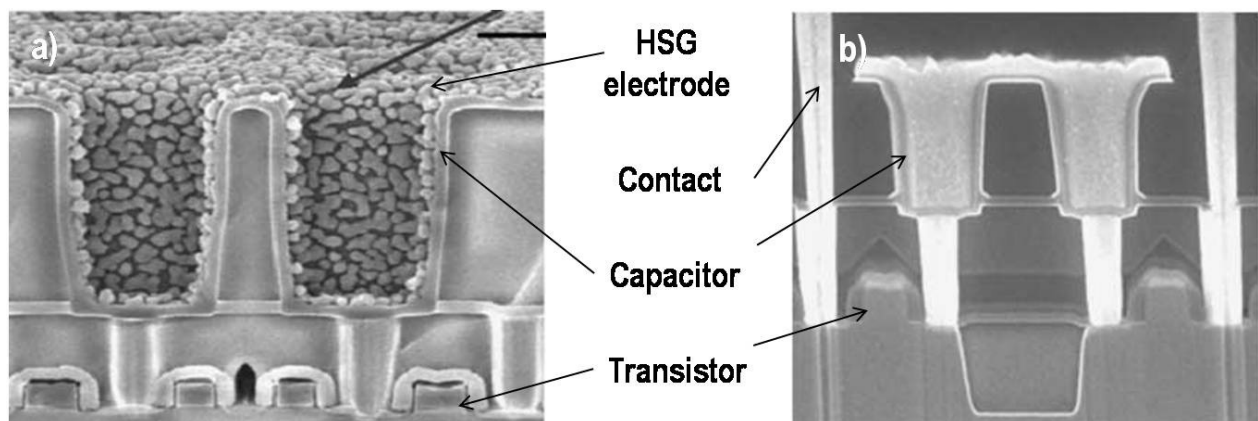


**Figure I.3 SEM cross sections of DRAM cells a) during production before the deposition of the dielectrics (includes hemi-spherical grained silicon (HSG) electrode), and b) post production with fully formed capacitor and contacts. SEMs courtesy of [21] with permission from Elsevier®.**

Over the last few years, flash memory has become popular in the form of USB sticks, MP3 players, memory cards, and as hard disk replacements in ultraportable notebooks. Flash is a non-volatile memory which was originally patented in 1984 by Masuoka [22] from Toshiba and commercialized in 1988 by Intel [23]. Storage of the information in flash memory is achieved by an electrical charge in a floating gate of a MOSFET transistor (Figure I.4). The floating gate is isolated in all three dimensions and as a result, retains the electronic charge/information for about 10 years. For reading the information, the transistor is either conductive or non-conductive. Write

and erase operations are performed via tunneling currents by using the control gate which overcomes the floating gate. The lateral isolation perpendicular to the source drain path is achieved with shallow trench isolation (STI) structures (Figure I.5) (section 1.4.2). More information on the development of flash memory and its operation can be found in the publications of Bez et al. [24], [25]. Current and future trends on memory devices are sketched by Kim et al [26] and Lu et al [27], which state that DRAM and flash memory will extend down to the 20–30 nm nodes. Beyond that, they expect the introduction of new gate geometries like charge trap devices and completely different technologies like phase change random access memory (PCRAM). Currently, the mainstream manufacturing technology is 45 nm with 32 nm in development.

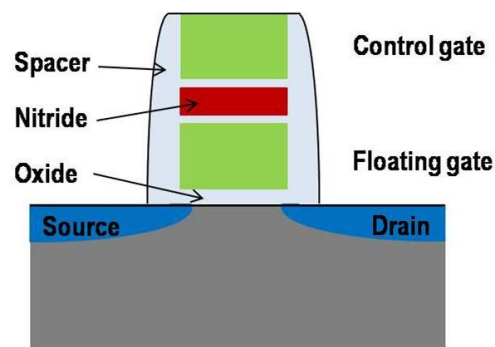


Figure I.4 Gate structure of a flash memory cell.

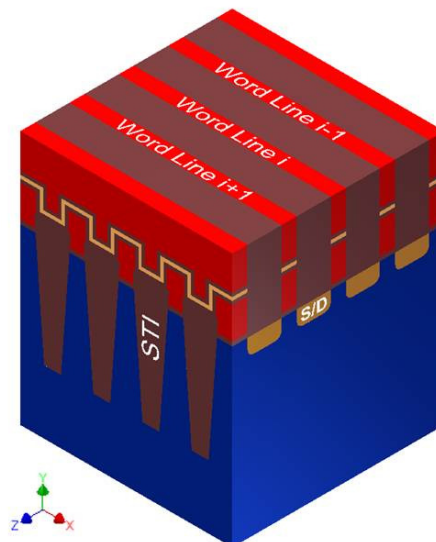


Figure I.5 Simplified 3D model of a flash memory cell. Note the isolation features around the floating gates (red) which are the STI in x-direction and the word line dielectric in y-direction. Model courtesy of D. Preiml (Lam Research AG) using the model of J. Postel-Pellerin et al. [28] as a guideline.

## 1.4 Semiconductor Structures with High Aspect Ratios

Lateral space on the silicon substrate is very valuable due to the increasing density of structures on an IC. Therefore, some structures are built into the third dimension, either buried inside the silicon substrate or built on top. The most important examples are capacitors on a DRAM chip and shallow trench isolation structures in flash memory devices. Proposed advanced gate structures like FinFETs also have high aspect ratios [29]. The aspect ratios of photoresist structures used for photolithography are limited by the ITRS because of pattern collapse (section 1.6). Nevertheless, photoresist is not considered in this PhD thesis due to existing research in the 2000s and their replacement by metal hard-masks in the applications prone to pattern collapse.

The aspect ratio is defined as the height of the structure ( $h$ ) vs. its line width ( $b$ ) both for line structures and cylinders (Figure I.6).

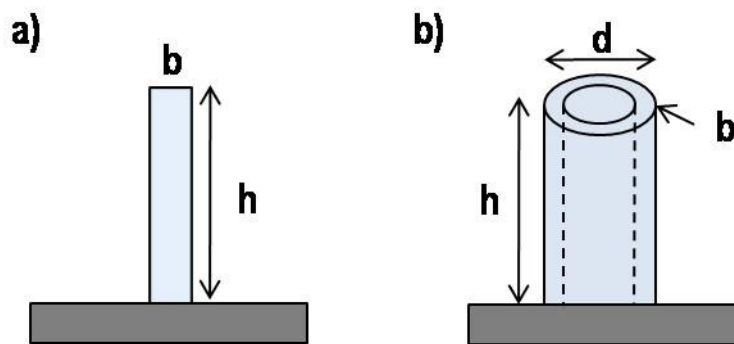


Figure I.6 Definition of the aspect ratio for line structures (a) and cylinders (b).

### 1.4.1 DRAM Capacitors

Currently, a DRAM cell consists of a transistor to access and a capacitor to store the binary information as an electrical charge. According to Moore's Law, the storage density increases with each new technology node and, therefore, the individual size of a single DRAM cell has to be decreased. Traditional scaling rules are applied to the transistor. At the same time the charge and the capacity is required to stay at the same level during device scaling ( $C = 25fF$ ) in order to assure stable circuit operation and sufficient soft-error immunity (i.e., immunity to cosmic X-rays) [12]. The capacity of a simple parallel plate capacitor is defined by equation [1]

$$C = \epsilon_0 \epsilon_R \frac{L_{cap} h_{cap}}{d_{ox}} \quad [1]$$

where  $\varepsilon_0$  is the vacuum permittivity,  $\varepsilon_R$  is the relative permittivity,  $A_{cap} = L_{cap}h_{cap}$  is the area of the plates, and  $d_{ox}$  is the thickness of the insulator between the plates. The state-of-the-art capacitor geometry on semiconductor chips is a cylinder (Figure I.7). An overview of the historic development of capacitor geometries can be found in the literature [21], which shows the trend of increasing aspect ratios for capacitors.

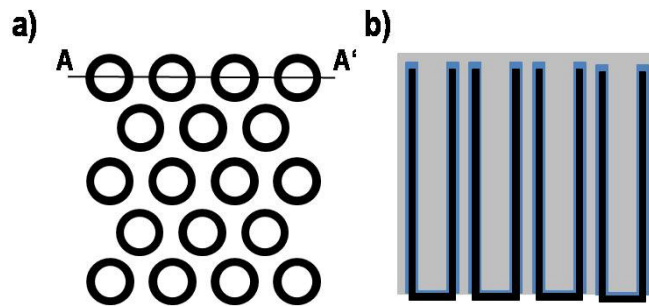


**Figure I.7 Cylindrical DRAM capacitors. a) top view of bottom electrode (black) and b) side view along AA' of finished capacitors with dielectrics (blue) and top electrode (grey).**

Scaling of the cylinder geometry also automatically decreases the capacity. In order to ensure a constant capacity, the other parameters have to be adjusted. The oxide thickness may be reduced, but only within the limit of acceptable leakage currents. The relative permittivity  $\varepsilon_R$  is determined by the choice of the insulator material. Originally silicon dioxide with a relative permittivity of 3.9 was used and has been replaced by  $\text{HfO}_2$ ,  $\text{ZrO}_2$  or  $\text{Ta}_2\text{O}_5$  with relative permittivities around 40.

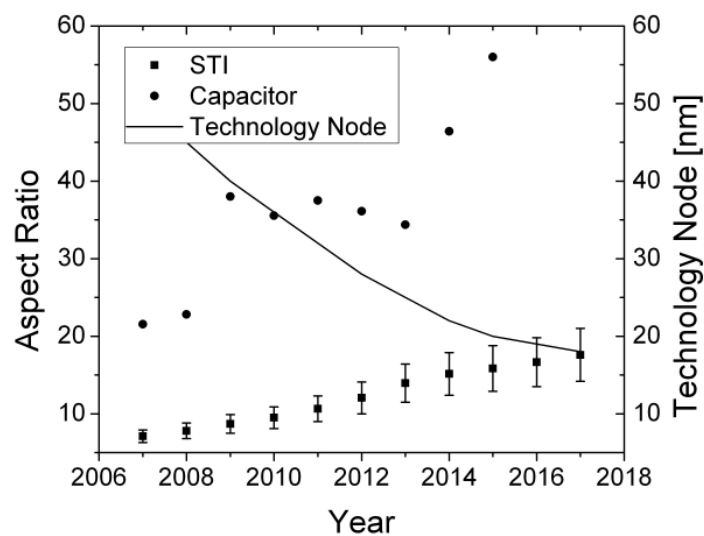


**Figure I.8 Aspect ratios of capacitor-over-bitline and STI structures based on data from ITRS [12].**

At the early stages, the cylinder consisted of polysilicon, but has since been replaced by TiN due to its higher conductivity, which decreases the time delay during read/write operations. For the future, several materials are under consideration as novel electrode materials, including Ru, RuO<sub>2</sub>, Pt, IrO<sub>2</sub>, and SrRuO<sub>3</sub> [12]. However, the incorporation of these proves to be difficult [30], and these materials have not been introduced to mass production as of 2010.

All the measures mentioned above are not sufficient to ensure enough capacity without an increase of the aspect ratio of the capacitor. Scaling of the cylinder height is predicted by the ITRS and shown in Figure I.8.

Two technologies were dominant over the past decade: one is burying the capacitor underneath the transistor inside the silicon substrate (trench) and the other is the stacked capacitor, which is placed above the transistor level (Figure I.9). The first approach has been abandoned.

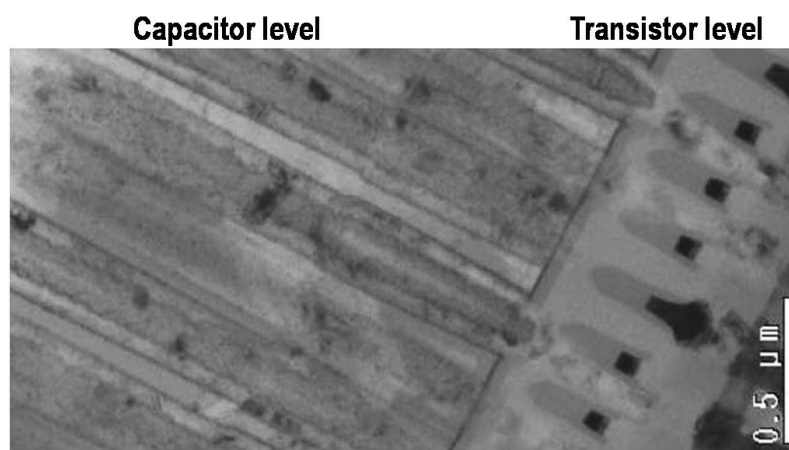
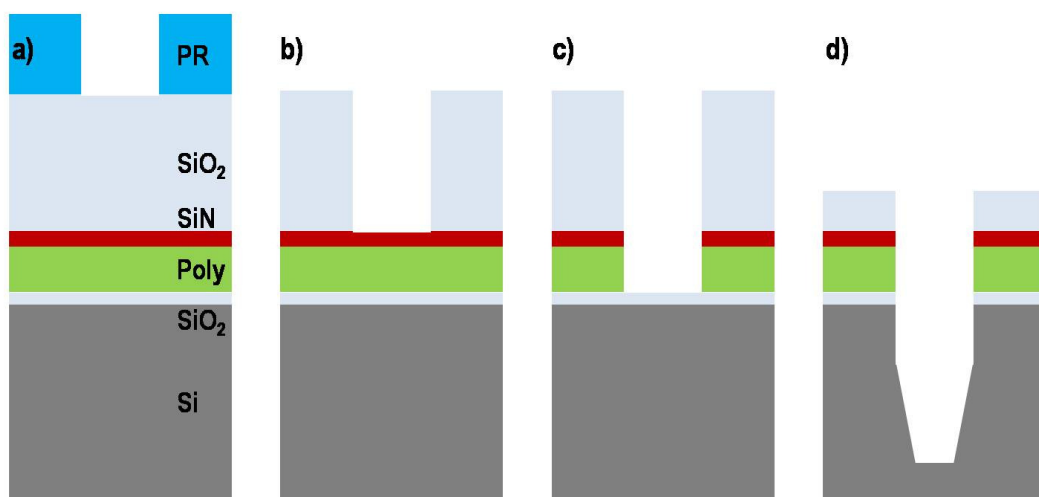


Figure I.9 TEM cross section of 110 nm stacked capacitor DRAM structures.  
Reprinted from [31] with permission from Elsevier®.

### 1.4.2 Shallow Trench Isolation Structures

Isolation between the transistors on a single chip has been traditionally achieved by the LOCOS (local oxidation of silicon) technology. Currently, this has been replaced by shallow trench isolation (STI) structures, especially for flash memory devices where the isolation and space requirements are most severe. In this application the term “shallow” in STI is misleading because the height of the STI exceeds its width by several times (Figure I.8).

For a better understanding of the semiconductor manufacturing cycle, a general outline is given for the formation of STI structures. An actual and more detailed example can be found in the literature from Applied Materials and Powerchip [16]. The manufacturing starts with growth of the gate oxide, followed by the deposition of a polysilicon and a silicon oxide layer. The latter is utilized as a hard-mask for the silicon substrate. Subsequently, a photolithography step is performed, which includes the deposition and the structuring of a photoresist layer (Figure I.10 a), which uses a double patterning technique for STI [32]. Transferring the structure from the photoresist into the silicon oxide hard-mask is achieved by a Bosch process [33] (Figure I.10 b). This process combines plasma etch with the deposition of an organic layer to protect the sidewalls and enables the manufacturing of high aspect ratio structures [34]. The hard-mask is necessary because photoresist would not be chemically stable enough for the subsequent Bosch process for structuring the polysilicon (Figure I.10 c) and the silicon substrate (Figure I.10 d). The final STI structure is shown in Figure I.11. However, some of the organic material on the sidewalls remains after the end of the dry etch processes (Figure I.12). If not removed, the post-etch residue would cause catastrophic device failure. Wet cleaning is generally used after both the hard mask and the STI etch. Finally, the trench is filled with silicon oxide by applying a high density plasma process [35].



**Figure I.10 Process flow for the formation of STI structures; a) starting with the patterned photoresist and ending with d) the fully etched STI trench. Please note: Schematics are not shown to scale.**

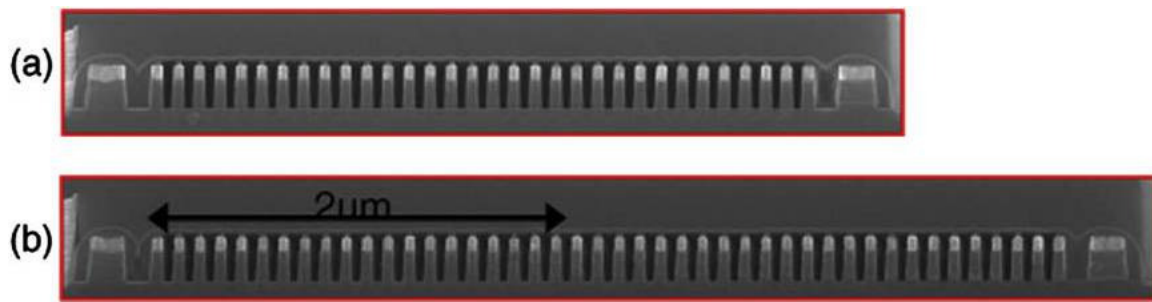


Figure I.11 SEM micrographs of STI structures from 51 nm flash memory from Samsung for 32 (a) and 44 (b) cell structures. Taken from [36] with permission from Elsevier®.

### 1.4.3 MEMS Structures

Micro-electro mechanical systems (MEMS) are small machines with a length scale of less than 1 mm and more than 1  $\mu\text{m}$  which are produced by using the wafer based processing procedures well established in the semiconductor industry. Important applications are pressure sensors [37], micro-mirrors for video projectors [38], and inertial moment sensors. The latter is found as yaw and accelerometer sensors in various applications, from the terminal guidance of re-entry vehicles of intercontinental ballistic missiles [39], to the rotation of cameras, and most commonly in the automotive industry, e.g., airbag control [40].

Inertial sensors are generally based on the principle of a mass attached to a spring. The suspended mass is deflected by acceleration due its moment of inertia. The deflection is usually measured by a change in the capacitance between an electrode on the suspended mass and a fixed reference electrode. In order to increase the sensitivity and the signal-to-noise ratio it is favorable to increase the capacity between the spring and the reference electrode. Thus, the designs include large areas and small gaps between the electrodes by using high aspect ratio structures and interleaving them. However, this creates the issue of stiction, which is described in section 1.6.2 in more detail.

## 1.5 Wet Surface Processing of Silicon Wafers

Surface processing of silicon wafers with liquid (wet) chemistry has two main objectives: etching and cleaning. Wet etching utilizes the more selective etch rates of liquid chemistries on different materials and crystallographic orientations compared to plasma (dry) etching. Cleaning is an important part of the semiconductor process cycle that improves the device yield by removing contaminants such as particles, metals, and post-etch residues (Figure I.12).

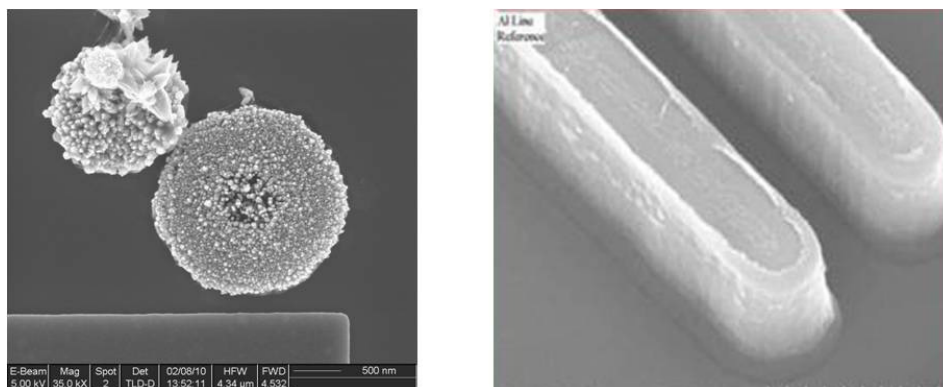


**Figure I.12 Particle (left) and post etch residue (right, courtesy of Lam Research).**

In 1970 Kern et al. from RCA (Radio Corporation of America) labs introduced a cleaning sequence that still remains the main cleaning approach in the semiconductor industry [41]. It consists of two parts: first, the “standard clean 1” (SC1) using ammonia, hydrogen peroxide, and de-ionized water and, second, the standard clean 2 (SC2), consisting of hydrochloric acid, hydrogen peroxide, and de-ionized water. The original recipe fixed the concentration; however, more recently the concentrations tend to be much more dilute than the originals due to environmental and economical concerns, as well as the limitation of attack on the surface (etch loss). The main purposes of SC1 are the removal of particles and post-etch residues, while, the main goal of SC2 is the removal of metal ions. These original processes are still widely used, though there are also other processes based on organic solvents, hydrofluoric acid, or sulfuric acid. After most cleaning processes a common procedure is rinsing the wafer with clean de-ionized water in order to remove the previously used chemicals.

Subsequently, a controlled drying process has to be performed in order to prevent re-deposition of the dispersed particles, as well as deposition of silica residues (“water-marks”) (Figure I.13) during the de-wetting/drying phase. Water-marks are particle



aggregations of silicon oxide or silicon (in case of a HF pre-clean process) [42], [43], [44] which would cause catastrophic device failure. Another source of damage during drying is called pattern collapse, which can be attributed to surface tension (section 1.6).

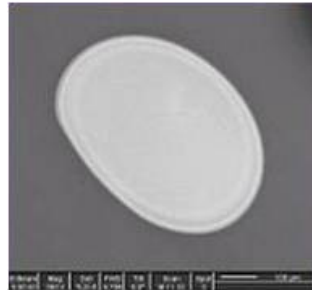


**Figure I.13 SEM micrograph of water mark on silicon surface. Diameter is approx. 0.5  $\mu\text{m}$ .  
Courtesy of Lam Research.**

## 1.6 Pattern Collapse

In this section, the phenomenon of pattern collapse in microelectronics is described, the current models are presented and the shortcomings of these are discussed. Additionally, research on this phenomenon with MEMS devices is mentioned and concepts for the prevention of pattern collapse are discussed.

### 1.6.1 Definition and Standard Surface Tension Model

Pattern collapse is a mechanical damage phenomenon occurring during the manufacturing cycle of a semiconductor device which can be attributed to wet chemical processes. The damage shows a distinct picture, typically two or more structures (patterns) stuck together at their free ends. Three different forms of pattern collapse can be distinguished due to the shape of the damage at the base of the structure (Figure I.14): the first form is a rupture inside the material (b); the second is delamination of, the structure at the interface to the substrate material beneath (c); and the third is no observable rupture, i.e., bending of the structures (d).

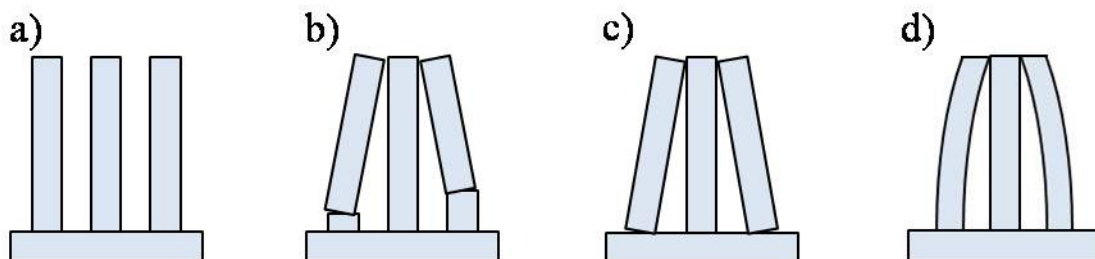


**Figure I.14** Principal shapes of pattern collapse: a) no collapse, b) ruptured in the material, c) delaminated at the interface, d) bending (elastically).

There is no distinctive nomenclature for the pattern collapse phenomenon which may also be known as stiction and leaning. The term stiction is mostly used for MEMS devices, whereas leaning is more commonly used for the collapse of DRAM capacitors. Only limited literature is available for the latter [45], [20], and no literature is available for STI, probably due to the sensitive corporate intellectual property involved in the formation of the structures. Nevertheless, Namatsu et al. [46] showed pattern collapse of <110> silicon structures with a similar shape as STI structures (Figure I.15).

The mechanical force responsible for pattern collapse is generally attributed to surface tension forces [47], [48]. If the wafer is fully covered with a liquid film, then

the liquid/gas interface is relatively far away from the wafer surface and, hence, from the structures. Thus, surface tension forces are only significant during the wetting and de-wetting phase of cleaning processes.

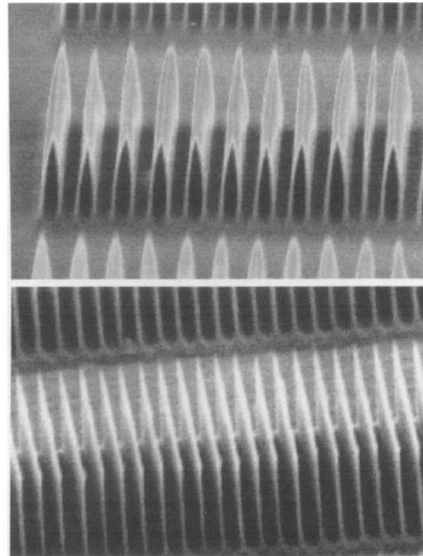


**Figure I.15 Pattern collapse of  $\langle 110 \rangle$  silicon test structures. Reprinted with permission from Elsevier® [46].**

In early studies, it was shown with atomic force microscopy (AFM) in liquid phase that pattern collapse happens during the de-wetting phase [47], [49]. The surface tension force is modeled with the Laplace equation, applying a geometric relation of the radius of the meniscus of the liquid and the space between the structures [48]. From the analysis of the forces (section 2.1), it is evident that high aspect ratio structures in combination with high surface tensions and mechanically weak materials (like photoresist) are most vulnerable to pattern collapse. Several more detailed numerical models have been proposed [50], [51], especially for more complex geometries [52], [53], [54], which seem to confirm surface tension as the major force for pattern collapse.

However, the big issue for all the models is the mechanical strength of the microelectronic structures. Most commonly, beam mechanics are used in order to analyze the force necessary for pattern collapse [55], [47], [48]. Finite element analysis (FEA) models are also based on the beam sway model; however, the real geometries are more complex. The models mentioned above are applicable only for the bending case of pattern collapse (Figure I.14 d). For the case of delamination and rupture, (Figure I.14 c, b), the corresponding forces were studied by AFM

measurements for photoresist line structures [56], [57], [58] and pillars [59]. Additionally, silicon dioxide nano-pillars were studied with AFM measurement [60], and it was found that delamination occurs at the interface [61], with some dependence on the surrounding chemistry [62]. There was only very limited experimental data at the beginning of this thesis on the mechanical stability of semiconductor nanostructures from device materials (i.e., non photoresist materials).

### **1.6.2 Pattern Collapse for MEMS Devices**

The pattern collapse phenomenon is known not only for the nanosized structures mentioned before, but also for MEMS devices (section 1.4.3), which include high aspect ratio structures as well. There is a significant difference between MEMS and microelectronics. In the latter case, the trenches between the structures are filled with material, and therefore, the structures are only vulnerable to pattern collapse for a certain number of process steps. In contrast, MEMS devices need to have freely moving parts (e.g., in inertial sensors), and therefore the prevention of pattern collapse needs to be ensured over the entire lifetime of the device. Significant research has been done to study this pattern collapse phenomenon in MEMS. A mechanical analysis of micro-beams was given by Mastrangelo and Hsu [63], [64]. The mechanical resistance of the beams depends on the respective aspect ratios and can therefore be used to characterize the “sticking forces”. Arrays of micro-beams with different aspect ratios were used experimentally for the quantitative analysis of capillary and adhesion forces.

These sticking forces prevent the elastically deformed structures from relaxing into their original positions after the liquid is removed. The sticking forces for MEMS devices are van der Waals type for hydrophobic and hydrogen bonding for hydrophilic silicon surfaces [65]. Additionally, the phenomenon of solid bridging [66], [65], [67] can occur where residues are formed between the structures thereby increasing the adhesion forces considerably [68].

The elastic nature of the bending-type pattern collapse allows for the concept of reducing the adhesion forces to a level below the restoring elastic force, which ensures detachment after the liquid is completely removed. A decrease of the adhesive energy can be achieved via the application of low surface energy organic coatings, reduction of the contact area via sidewall spacers, as well as increased

surface roughness [69]. For a review of the adhesion and stiction phenomena see [70] where all major concepts and aspects are presented and discussed.

STI structures (section 1.4.2) approach similar aspect ratios as MEMS devices, and therefore, the bending case with stiction may become important for microelectronics as well. For the prevention of (expected) future stiction in STI structures, it is important to understand whether the solid bridging phenomena may become more important with decreasing size of the structure due to nanoscale effects

### 1.6.3 Concepts for Prevention of Pattern Collapse in Microelectronics

In addition to the prevention of water marks, the prevention of pattern collapse [43] has been a major issue in the development of drying processes used in the microelectronic industry. Traditional single-wafer processes include spin drying and air flow drying, whereas more recent approaches use alcohols or alcohol/de-ionized-water mixtures (typically isopropanol (IPA)) for achieving lower surface tension and, therefore, are expected to cause less pattern collapse (Figure I.16). Low surface tension developers for photoresist have also been discussed [71].

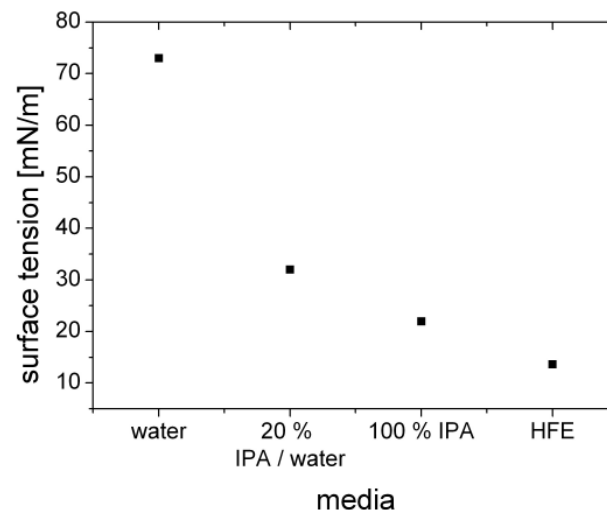


**Figure I.16** Surface tension of typical and proposed drying liquids in the semiconductor industry.

Additionally, the use of ultra-low surface tension liquids like hydrofluoroether (HFE) are considered, and the use of supercritical CO<sub>2</sub> has been studied and promoted by some groups [46],[72], [73], [74]. The latter would eliminate any surface tension forces and, therefore, would be theoretically ideal for the prevention of pattern

collapse. However, there are several issues for introducing these solvents into the semiconductor process-flow due to the level of cleanliness required (i.e., the solvent is more contaminated than the surface to be cleaned) and also because of economical reasons. Thus, no supercritical drying is used in the microelectronic industry today, and its introduction continues to be pushed out to the future.

The second promising concept is to strengthen the structures instead of decreasing the surface tension. One early example is to increase the mechanical resistance by a post-bake of the photoresist prior to the drying step [75]. Another example is the introduction of additional support structures. The prominent example of this is the MESH (mechanically enhanced storage node height) structure in DRAM products from Samsung (Figure I.17) [26], which provides a mechanical spacer ring between the cylinders. This structure is expensive due to the additional process steps in the manufacturing process, and it also decreases the electrical isolation between the DRAM cells. As a result, a solution without support structures would be beneficial. Additionally, support structures for STI structures seem to be not economical at the moment.

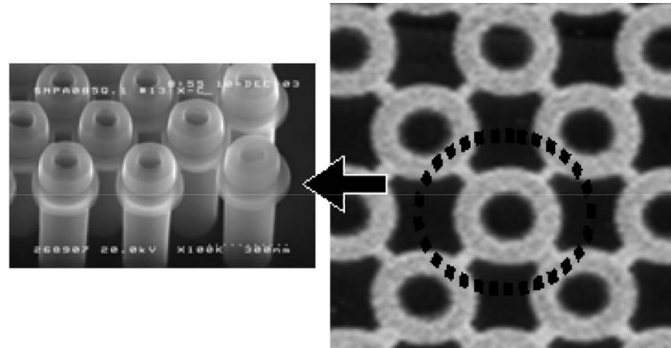


Figure I.17 DRAM capacitors with MESH structure. Reprinted with permission from Elsevier® [26].

#### 1.6.4 Pattern Collapse Theories Other than Surface Tension

During the last years, additional theories have been discussed in the industry related to pattern collapse; however, none of these were published. In this section the “new” hypotheses are briefly named and discussed.

Post-etch residues, have been observed to increase pattern collapse, which may be due to a reduced contact angle compared to hydrophobic silicon. Chemical reactions between the post-etch residues may be possible as well. However, the residues

would cause device failure without pattern collapse, which make this hypothesis secondary.

A very sensitive issue is electrostatic charging during wet chemical processes, which can lead to catastrophic device failures due to electrostatic discharge. Additionally, localized electrostatic charges may also introduce mechanical forces sufficient for pattern collapse. In this case, the defect is already generated by the electrical discharge, and so mechanical collapse does not matter anymore.

The reduction in physical size of the structures also decreases the mechanical stability sufficiently against forces that could be previously neglected. In addition, mechanical stress at an interface introduced by high temperature deposition of a layer with different coefficient of thermal expansion can lower the collapse force significantly. The force models discussed include air flow over the rotating wafer, hydrodynamic forces, centrifugal forces [76], and mechanical shocks due to wafer handling. For the centrifugal and hydrodynamic forces, a damage picture following the force geometry would be expected. In case of the former, all damaged structures should be bent towards the wafer edge, which has not been observed. The largest uncertainty when discussing the force models is the mechanical stability of the nanostructures. Mostly beam mechanics, in combination with material constants measured in the micron scale, are used. It was unknown whether these parameters and the models can be extended to the nanometer scale. Additionally, surface chemical reactions may influence the mechanical stability of the structures via a corrosion process.

Vibrations have also been proposed as being sufficient for bringing the structures statistically into contact. This case is more closely related to stiction in MEMS devices, where sufficient adhesion forces have to keep the structures together for pattern collapse (section 1.6.2). However, it is assumed that the structures in vibration may touch neighboring structures but usually also detach again. A similar effect could also happen during a drying process when the capillary force is finally removed through evaporation. Thus, there must be either a line width variation or an additional “sticking” force for the cases where permanent pattern collapse occurs. The most probable case would be a solid bridging process, which has not yet been observed in microelectronic structures.

As the size of the structures approaches atomistic levels, previously unknown or disregarded effects may become important. Capillary condensation may introduce a lower level in terms of structure size for ambient processing and storage. In such a case humidity would immediately condense into the trenches of the structures which would then lead to pattern collapse even before a cleaning process is attempted.

Pattern collapse is a serious issue for the most advanced products of the semiconductor industry (like flash and DRAM), which progress into structure sizes of 40 nm and below. Traditional models attribute pattern collapse to the surface tension force. In order to get a better understanding of the phenomena, especially in light of the proposed models other than surface tension, two major points for further studies were identified: the mechanical stability of nanostructures and solid bridging of nanosized structures. However, first an evaluation of the forces between nanostructures is performed in order to evaluate the traditional surface tension theory.



## II Theory

The interactions between nanostructures in close proximity, with application to pattern collapse are described in this chapter. In addition to surface tension forces, van der Waals forces, spin forces, and hydrodynamic forces are considered, as well as hydrogen bonding and solid bridging (see section 1.6.2). Body forces such as gravitation are neglected due to the small size of the structures; however, for single-wafer cleaning, centrifugal forces could be an issue, and so these are included. In the second part, these forces are discussed with respect to the mechanical stability of silicon structures.

### 2.1 Forces at the Nanoscale during Drying

Here the most prominent forces for nanoscale structures are described and compared in terms of their significance during a drying process (section 2.1.7). The geometry of two parallel plates is employed, which is most suitable for line structures. For ease of comparison, the forces are normalized with respect to the area. A similar comparison can be found in the literature for MEMS devices [65]. For the structures, the material data from silicon is used.

#### 2.1.1 van der Waals Forces

The term van der Waals (vdW) forces summarizes interactions between dipoles, which consist of three parts: orientation, induction, and dispersion [77]. The interaction of permanent dipoles is considered under orientation. Induction describes the forces between a permanent dipole and an induced dipole based on the electromagnetic field from the permanent dipole. The dispersion force is quantum mechanical in origin and can be intuitively understood as the instantaneous finite dipole moment of a non-polar atom. Nevertheless, the time average of this dipole

moment is zero [77]. All three parts interact with the surrounding material resulting in a finite force.

The interaction energy of two flat surfaces  $w_{vdW}$  is given in equation [2] for the non-retarded regime ( $d < 20$  nm) according to ref. [77]

$$w_{vdW} = \frac{W_{vdW}}{A} = -\frac{A_{Ham}}{12\pi d^2} \quad [2]$$

where  $A_{Ham}$  is the Hamaker constant and  $d$  the distance between the surfaces. The Hamaker constant for two silicon oxide surfaces interacting through water is given as  $0.83 \cdot 10^{-20}$  J [77]. The corresponding force due to van der Waals interaction yields

$$f_{vdW} = \frac{F_{vdW}}{A} = \frac{A_{Ham}}{6\pi d^3} \quad [3]$$

per unit area (equation [3]).

### 2.1.2 Hydrogen Bonding

When the separation between hydrophilic silicon surfaces becomes small, hydrogen bonds can be formed. The energy of such bonds is determined by the type of acceptor and donor atoms, density of hydroxyl groups on the surface and their geometric orientation. Considering only Si-OH groups, depending on the density, the usual adhesion energies are calculated to be in the range of 90–350 mJm<sup>-2</sup> [65], [70]. The experimental data from wafer bonding experiments on hydrophilic silicon confirms this energy range, and values between 50 and 200 mJm<sup>-2</sup> are reported [78].

### 2.1.3 Solid Bridging

Non-volatile impurities in the rinse liquid can be deposited on the surfaces if the drying process is governed by evaporation [66]. These impurities can originate from a previous etch process or silicates directly dissolved in the rinse liquid (de-ionized water). In small gaps or holes, the deposition is increased and can act as glue holding the structures together. The bonding strength exceeds forces exerted by the vdW interaction and hydrogen bonding forces at the contact [68].

### 2.1.4 Electrostatic Forces

It is necessary to prevent electrostatic charging on a wafer in order to prevent electrostatic discharge. Furthermore, the electrostatic charges can also exert forces on the structures on the wafer. The electrostatic force per unit area  $A$  between two conducting plates is given by equation [4]

$$f_{el} = \frac{F_{el}}{A} = \frac{\varepsilon_0 V^2}{2d^2} \quad [4]$$

where  $\varepsilon_0$  is the vacuum permittivity,  $d$  is the distance between the plates, and  $V$  is the voltage difference between the two plates. As there is a conductive path between the structures, only very small voltage differences are possible. The voltage is set to 0.5 Volts, which is a worst case assumption; this would cause a significant current of 1 mA/cm along the conductive path. Nevertheless, when the structures are subject to extreme local charging conditions like a SEM electron beam with high acceleration voltages in the 10 kV range, higher potential differences between two opposing structures are also possible.

### 2.1.5 Centrifugal Forces

During spin drying of silicon wafers, rotational speeds of up to 2000 rpm may be applied in order to dry the wafer surfaces. Additionally, alcohol-based dryers on spin tools operate usually in the range of 500 rpm. Centrifugal forces on the structures itself also need to be considered. The centrifugal force  $F_{cen}$  is defined as (equation [5])

$$F_{cen} = m \cdot \omega^2 \cdot r = m \cdot (2 \cdot \pi \cdot n)^2 \cdot r \quad [5]$$

where  $m$  is the mass of the body,  $\omega$  is the angular frequency,  $n$  is the rotational speed, and  $r$  is the radius of the respective body from the center. Thus, a structure at the edge of the wafer experiences the highest forces.

For the mass of the body, two different scenarios are considered. The first describes only the mass of the structure itself according to equation [6]

$$m_1 = \rho_{Si} \cdot h \cdot l \cdot w \quad [6]$$

where  $\rho_{Si}$  is the density of silicon (2.329 g/cm<sup>3</sup>),  $h$  is the structure height (e.g., 150 nm),  $l$  is the length of the structure and  $w$  is the line width of the structure (e.g. 40 nm).

For the second model, the liquid next to the structure is added to the mass. This situation corresponds to a dam holding back the fluid that is pressed towards the wall by centrifugal forces. A reasonable value for free distances on a silicon chip is about 10  $\mu$ m. The combined mass with the structure is given by equation [7]

$$m_2 = m_1 + m_l = m_1 + \rho_l \cdot h \cdot l \cdot w_l \quad [7]$$

with  $\delta_l$  being the density of the liquid, in our case water ( $1 \text{ g/cm}^3$ );  $h$  the height of the dam, i.e., the structure (150 nm);  $l$  the length of the structure; and  $w_l$  the width of the liquid. As the mass of the liquid is exceeding the mass of the structure, the later can be safely neglected. Inserting equations [6] and [7] into [5] and assuming that  $r$  is exceeding  $w_l$  by several times and normalizing to the respective area gives the following equations

$$f_{Cen_1} = \frac{F_{Cen_1}}{h \cdot l} = (2 \cdot \pi \cdot n)^2 \cdot r \cdot \rho_{Si} \cdot w \quad [8]$$

$$f_{Cen_2} = \frac{F_{Cen_2}}{h \cdot l} = (2 \cdot \pi \cdot n)^2 \cdot r \cdot \rho_l \cdot w_l \quad [9]$$

### 2.1.6 Capillary Force

After the wet (cleaning) process, the remaining liquid film is removed by drying. When the liquid-air interface gets close to the surface of the structures, it breaks up into menisci. An example of menisci in nanoscale structures has been visualized by TEM for carbon nanotubes [79]. The pressure difference across a meniscus,  $\Delta p_{Cap}$ , is described by the Young-Laplace equation [80] [10]

$$\Delta p_{Cap} = \gamma_l \left( \frac{1}{r_{\parallel}} + \frac{1}{r_{\perp}} \right) \quad [10]$$

where  $\gamma_l$  is the surface tension, and  $r_{\parallel}$  and  $r_{\perp}$  are the radii parallel and perpendicular to the line structures, respectively. The radius parallel to the structure exceeds the perpendicular radius by orders of magnitude and is therefore negligible for the pressure difference. Thus, equation [10] is reduced to equation [11]

$$\Delta p_{Cap} = \frac{2 \cdot \gamma_l \cdot \cos \alpha_{con}}{d} \quad [11]$$

when taking the contact angle into account. Here  $\alpha_{con}$  is the contact angle, and  $d$  is the distance between the lines. The pressure difference across the interface tends to pull the structures together if the contact angle is less than 90 degrees. If the liquid is homogeneously distributed between the structures, then there is no resulting force (structure C in Figure II.1). In that case, capillary forces on either side of the structure cancel each other. A net force only exists if the forces are unbalanced by different filling heights of the trenches on the opposite sides of a structure (A) or by dissimilar spacing of the structures (B) (Figure II.1). The capillary force is defined as the capillary pressure in combination with the respective area (equation [12]).

$$F_{Cap} = \Delta p_{Cap} \cdot A \quad [12]$$

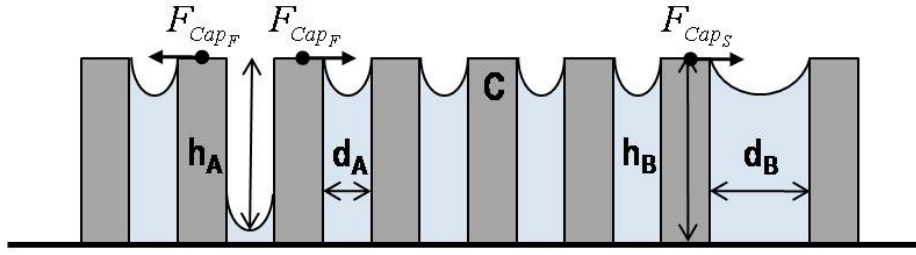


**Figure II.1 Scheme of balanced (C) and unbalanced capillary forces in dense structures (dark) by a variation in fill height (A) or spacing (B).**

For the case of different filling heights, the resulting force  $F_{Cap_F}$  is determined by the variation of the wetted area. In the case of different spacings  $F_{Cap_S}$  is given by the difference in capillary pressure due to the larger meniscus radius in the trench on the right side compared to the one on the left side of the structure (b) (see equations [13] and [14])

$$F_{Cap_F} = \frac{2 \cdot \gamma_l \cdot \cos \alpha_{con}}{d_A} \cdot h_A \cdot l \quad [13]$$

$$F_{Cap_S} = 2 \cdot \gamma_l \cdot \cos \alpha_{con} \cdot h_B \cdot l \cdot \left( \frac{1}{d_A} - \frac{1}{d_B} \right) \quad [14]$$

where  $l$  is the length of the line structure. All other parameters are illustrated in Figure II.1.

The line width variation for STI structures is very small, and the edges of the STI arrays are typically covered by the larger bitline transistors. Therefore, the case of different spacing is negligible, and, only the case with different filling heights is considered. For the force analysis in section 2.1.7, a worst case scenario is assumed where the trench on one side of a structure is completely filled with water ( $\gamma_l = 72$  mN/m) or isopropanol ( $\gamma_l = 22$  mN/m) and the opposite trench is filled with air. A hydrophilic situation is assumed for both liquids with contact angles less than 10 degrees, giving a  $\cos \alpha$  close to 1, which yields  $f_{Cap_F}$  (equation [15])

$$f_{Cap_F} = \frac{F_{Cap_F}}{h_A l} = \frac{2 \cdot \gamma_l \cdot \cos \alpha_{con}}{d_A} \quad [15]$$

Recently, Farshid Chini et al. [81] introduced a new model for pattern collapse that added the lateral surface tension to the capillary pressure (Figure II.2). Only the component perpendicular to the structure of the surface tension  $F_{ST_x}$  force adds to the overall force.

$$F_{ST_x} = \gamma_l \cdot l \cdot \sin \alpha_{con} \quad [16]$$

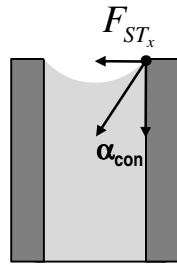


**Figure II.2 Horizontal component of the surface tension force.**

Comparing the surface tension force  $F_{ST_x}$  with the capillary force  $F_{cap_F}$  [13] gives an indication of its importance by using the same parameters. The ratio of both forces is defined as

$$\frac{F_{cap_F}}{F_{ST_x}} = \frac{2 \cdot h_A \cdot \cos \alpha_{con}}{d_A \cdot \sin \alpha_{con}} \quad [17]$$

For the case of STI structures with an aspect ratio  $h_A/d_A$  of 20 and a low contact angle as for isopropanol on silicon structures it is safe to assume that the capillary force exceeds the surface tension force by at least an order of magnitude. Thus, the latter can be neglected in this case. However, for photoresists with lower aspect ratios and higher contact angles it may be different.

### 2.1.7 Evaluation of the Forces

The different possible forces discussed above are now compared to each other and with respect to their relevance in pattern collapse. The main forces between two structures are shown in Figure II.3 for electrostatic, van der Waals, and capillary forces. The latter are calculated for de-ionized water and isopropanol, which are the liquids most commonly utilized in drying processes in the semiconductor industry. From Figure II.3, it is obvious that capillary forces significantly exceed van der Waals and electrostatic forces.

Another concern are the spin forces acting on the structures during spin processing. These do not depend on the distance between the structures and are in the negligible range of  $10^2 \text{ Nm}^{-2}$ , for a 40 nm structure (at the edge of the wafer with a speed of 500 rpm). Adding the weight of the liquid of the adjacent  $10 \mu\text{m}$  increases the spin forces only to  $10^4 \text{ Nm}^{-2}$  which is still far lower than the surface forces.

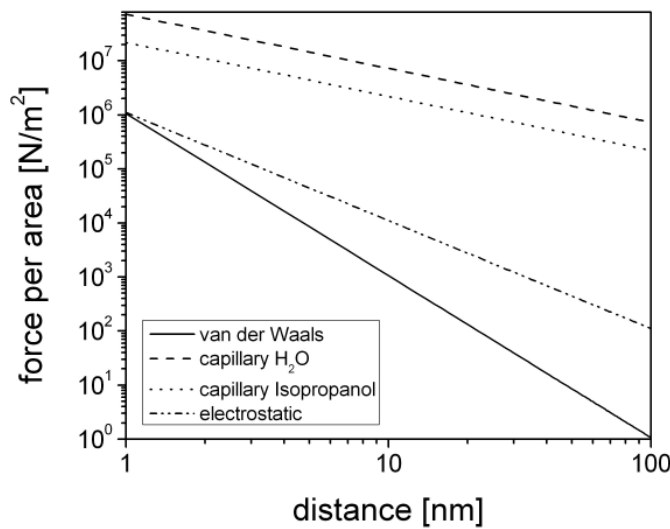


**Figure II.3 Comparison of van der Waals, electrostatic, and capillary forces between two plates.**

For the case of pattern collapse with elastic bending of the structures (Figure I.14 d), an adhesion force at the contact point of the structures (Figure II.4) compensates the elastic deformation energy. Initially, this is probably the capillary force which is reduced by evaporation down to the equilibrium Kelvin radius  $r_k$  (equation [18])

$$r_k = \frac{2 \cdot \gamma_l V_m}{R \cdot T \cdot \ln \frac{p}{p_0}} \quad [18]$$

where  $V_m$  is the molar volume of the liquid,  $R$  is the gas constant,  $T$  is the temperature, and  $\frac{p}{p_0}$  is the relative vapor pressure.

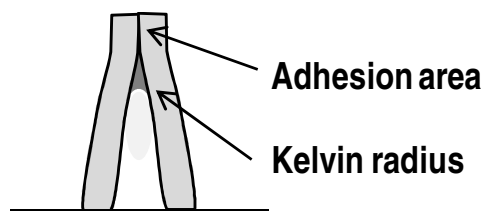


**Figure II.4 The bending case of pattern collapse with the area of adhesion and the Kelvin radius.**

Finally, it was found for MEMS devices that after drying, capillary forces are no longer significant. The hydrophobic silicon structures are bonded by vdW forces and for hydrophilic surfaces hydrogen bonding is dominant [65]. The theoretical and experimental energies are shown in Table 1. Additionally, the effect of solid bridging can significantly increase the adhesion forces.

**Table 1 Interaction energy of silicon surfaces (theoretical and experimental) as published by Legtenberg et al. [65] and Maboudian et al. [70].**

Theoretical	type of force	van der Waals	hydrogen bridging
	interaction energy [ $\text{mJ}/\text{m}^2$ ]	29	90 – 350
Experimental	surface	hydrophobic	hydrophilic
	interaction energy [ $\text{mJ}/\text{m}^2$ ]	$50 \pm 50$	$260 \pm 100$

The theoretical comparison of forces indicates that capillary forces are dominant during a drying process. Once collapse has occurred for the case of bending experiments with MEMS devices, van der Waals forces and hydrogen (bond) bridging become the dominant adhesion forces that keep the structures together. The unknown parameter in terms of formation and magnitude is the phenomenon of solid bridging.

For the evaluation of the relevance of the forces discussed in this chapter, a comparison with the mechanical stability of the respective structures is necessary.



## 2.2 Beam Sway Models

The mechanical stability of silicon nanostructures will be discussed using continuum mechanics with application to the forces discussed in section 2.1. First, the forces are calculated using Euler Bernoulli beam mechanics. Second, the stress introduced into the structures is studied by finite element analysis. Two types of structures will be considered: a future 20 nm STI structure and the ASAP structures (test structures, see section 3.1.1) that were used for the mechanical stability measurements. The respective dimensions can be found in Table 2. For the ASAP and STI structures, the Young's modulus of <100> silicon [82] is used to demonstrate the effect of the geometry. The length of the line was chosen as 500 nm which is the lower limit for damages of point forces in air for the ASAP structures (section 4.1).

**Table 2 Dimensions and material properties of the continuum mechanics models**

	ASAP	STI
Young's modulus $E$ [GPa]	130	130
width $w_{line}$ [nm]	40	20
length $l_{line}$ [nm]	500	500
height $h_{line}$ [nm]	150	400

### 2.2.1 Analytical Model

The STI and ASAP structures resemble small thin plates where Euler Bernoulli beam mechanics are applied. For the mechanical load two models are distinguished: distributed loading and one end load (Figure II.5). The latter resembles the case of AFM measurements whereas the former is appropriate for capillary and vdW forces.

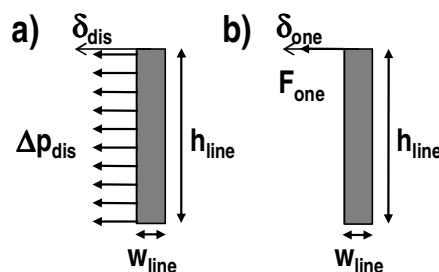


**Figure II.5 Distributed load (a) and one end load (b) model for beam mechanics.**

The relationships between the forces and the deflections are given by equations [19] and [22]

$$\delta_{one} = \frac{F_{one} \cdot h_{line}^3}{3 \cdot E \cdot I} \quad [19]$$

$$\delta_{dis} = \frac{\Delta p_{dis} \cdot l_{line} \cdot h_{line}^4}{8 \cdot E \cdot I} \quad [20]$$

where  $I$  is the second moment of area depending on the cross-section of the beam (equation [21])

$$I = \frac{l_{line} \cdot w_{line}^3}{12} \quad [21]$$

Combining the equations [19] and [20] with the moment of area [21] gives

$$\delta_{one} = \frac{4 \cdot h_{line}^3}{E \cdot w_{line}^3} \cdot \frac{F_{one}}{l_{line}} \quad [22]$$

$$\delta_{dis} = \frac{3 \cdot h_{line}^4}{2 \cdot E \cdot w_{line}^3} \cdot \Delta p_{dis} \quad [23]$$

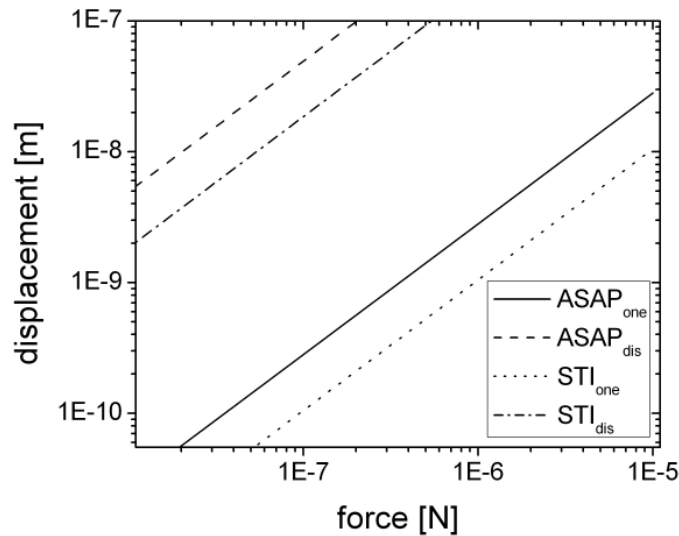


**Figure II.6 Beam deflections of ASAP and STI structures (Table 1) calculated with Euler Bernoulli beam theory (equations [22] and [23]).**

Clearly the structures are more easily deformed the higher the aspect ratio and the farther the force is applied from the bottom. The condition for pattern collapse is usually a displacement of half of the line width, which corresponds to 10 nm for the STI and 20 nm for the ASAP structures. The forces were equal to 30 nN (100 nN) for STI and to tens of  $\mu$ N for ASAP structures. In order to decide which type of pattern

collapse can happen, i.e., rupture vs. bending for these structures, it is necessary to estimate the internal stress.

### 2.2.2 Stress Analysis

Finite element analysis is used for the internal stress determination of the structures described in the previous section. For the geometry, the one end model is used as it is the more severe case in terms of displacement. In order to convert the stress tensor to a scalar number, the von Mises stress [83] criterion is used. The general stress distribution shows a maximum at the bottom edges of the line where it is clamped to the substrate (Figure II.7).

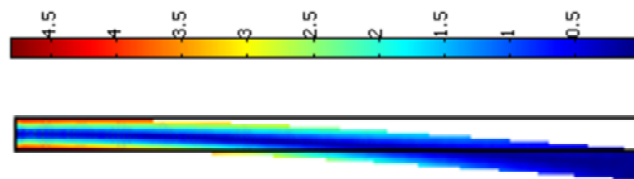


Figure II.7 STI structure simulated by finite element analysis using the one end load model (rotated by 90 degrees, i.e., clamped on the left, force on the right). The deformed shape is shown with the von Mises stress criterion (scale corresponds to  $10^8$  Pa) and the original shape in denoted in the background.

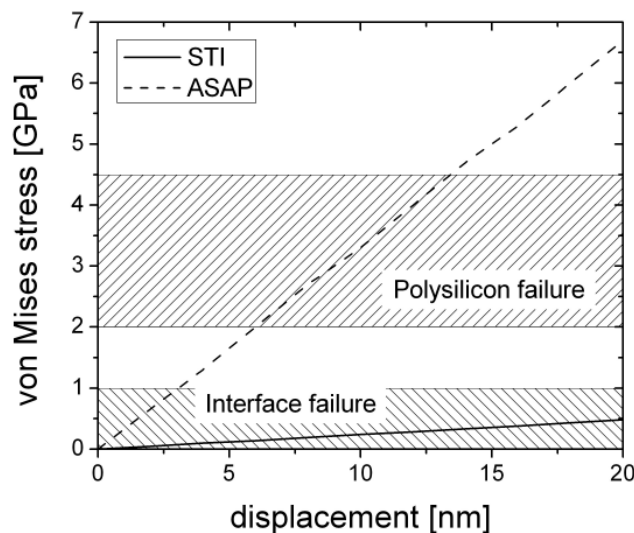


Figure II.8 Maximum mechanical stress during displacement  $\delta_{one}$  of the beam with one end loading.

Using the pattern collapse criterion, which corresponds to 20 nm for the ASAP and 10 nm for the STI structure, different results in terms of internal stress are obtained

(Figure II.8). For the former, the internal stress exceeds the fracture strength for polysilicon, which is reported between 2 and approximately 4.5 GPa [84], [85], [86]. The latter corresponds to the lower fracture strength reported for single-crystal silicon.

For the STI case the stress is small and, actually lower than the fracture strength usually attributed to interfaces (<1 GPa). A pattern collapse with fracture is expected for the ASAP structures due to the brittle nature of the material, and a bending case is expected for the STI structures. The reported fracture strengths are measured on micrometer-sized specimens, which may not be applicable to nanometer-sized structures. Additionally, interfaces may decrease the fracture strength considerably. Therefore, the ASAP structures were chosen to measure the fracture strength and the corresponding forces.

### 2.2.3 Pattern Collapse Analysis

By comparing the nanoscale forces (section 2.1) with the deformation strength of the structure, an indication can be given whether or not pattern collapse can happen. The capillary forces and the corresponding restoring forces for the ASAP and STI structures are summarized in Figure II.9.

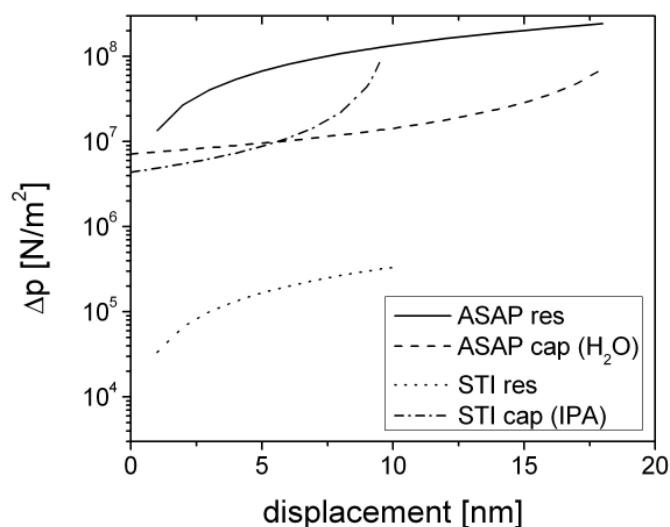


**Figure II.9 Comparison of relevant forces during drying with the corresponding restoring forces (equation [23]) for the ASAP and STI structures.**

The restoring forces exceed the capillary forces at all separations for the ASAP structures, thus making pattern collapse during drying unlikely except for the case of

limited fracture strength, e.g., due to bad adhesion at the interface. For the STI structures, the capillary forces exceed the restoring forces at all times, hence 100 % pattern collapse (bending case) would be expected during drying. Analysis of such structures does not follow this expectation which shows only local bending pattern collapse events. van der Waals and hydrogen bonding are possible candidates for the sticking forces; however, these forces are homogenous and should give also either zero or 100 % collapse. On the other hand, solid bridging is a much more localized event and consequently is a prime candidate for explaining this behavior. However, no such bridging on STI structures has been reported up to now.

## III Methods

The chapter on methodology is divided into two parts. The first part describes the materials used for the experiments and the second focuses on the analytical techniques utilized for the characterization of the materials in the experiments.

### 3.1 Materials

Semiconductor line structures were used for the characterization of the mechanical stability of nanostructures with lateral force microscopy (LFM). The design of the line structures and the cantilevers are described in the following sections. For the verification of the solid bridging phenomenon, silicon nanoparticles were utilized. Finally, the physical properties of the relevant chemicals are summarized.

#### 3.1.1 Semiconductor Line Structures (ASAP 300)

A set of wafers was obtained from IMEC (IMEC, Kapeldreef, Belgium; IMEC = Interuniversity Microelectronics Centre) for the evaluation of the stability of silicon nanostructures with AFM. The wafers carry polysilicon structures that resemble real device structures in terms of mechanical characteristics. The mask set for the structures is commonly called “ASAP 300”, where the number indicates the wafer size of 300 mm (12 inch). The lines on this maskset are organized in sets of ten lines with a length of 9500  $\mu\text{m}$  (Figure III.1).

Three layers are deposited onto the wafer prior to the photolithography step. First, a silicon oxy-nitride layer with a thickness of 2.4 nm is grown by co-nitridization [87]. Second, 100 nm of polysilicon are deposited by a chemical vapor deposition (CVD) process using silane gas at a temperature of about 700°C, which results in the deposition of coarse grained polysilicon. The average grain size is between 200 nm and 500 nm.

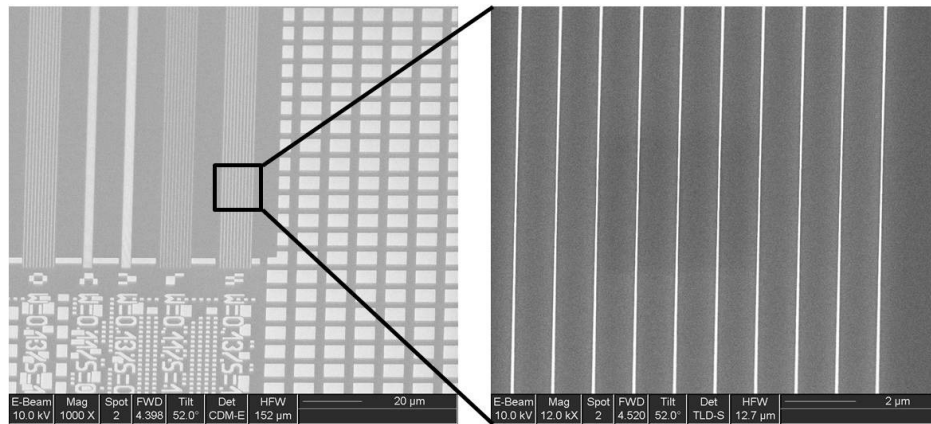


**Figure III.1 SEM micrograph of line structures defined with the ASAP 300 mask. The lines are organized into sets of ten lines with different spacing per set (here: 1  $\mu\text{m}$ ).**

Third, another CVD process is used to deposit a silicon oxide hard mask layer on top of the polysilicon. Finally, a photolithography step is performed consisting of the deposition of photoresist, exposure to light via a reticle, and subsequent development of the photoresist. The negative pattern of the resist is transformed into the material stack by means of plasma etching. Because IMEC was not able to resolve 40 nm structures with its photolithography equipment at the time of production of the structures, they used a trim etching technique. Hence, the structures originally developed and etched have a much larger line width (130 nm) than the targeted 40 nm. Subsequently a trim etch process was used to reduce the structures to the designated line width. The final structure is shown in Figure III.2.

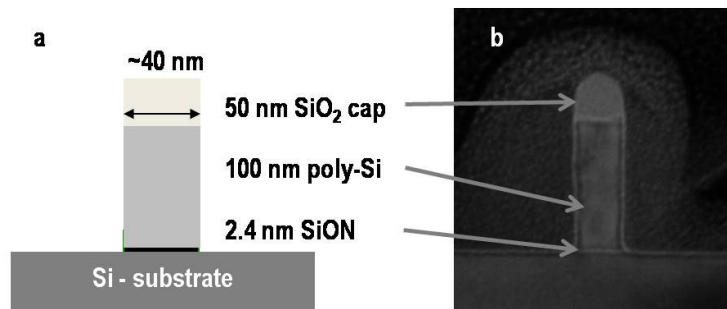


**Figure III.2 (a) Schematic cross-section through the line structures and (b) a TEM micrograph. The structure in (b) was covered with platinum for mechanical protection. TEM image courtesy of FELMI TU Graz.**

The trim etch technique also invokes some constraints on the minimum density of the structures. When the spacing between the structures is small, the trim etch process results in nominal 50 nm lines for the small spacing (170 nm) and 40 nm for the large spacing (1  $\mu\text{m}$ ) (Figure III.3 b). Moreover, there is a set of 110 nm wide lines on the

mask that turn into 25 nm lines after the trim etch (Figure III.3 a). The relative line width variation of the 25 nm lines is significantly higher (10 – 40 nm) than for the 40 nm lines (35 – 50 nm) as measured by SEM. As a result, most tests were done with the 40 nm lines. The local line width variation over tens of microns is as large as the variation on the entire wafer as measured on multiple locations on the wafer. Therefore no pre-selection of the position for testing with the AFM was necessary.

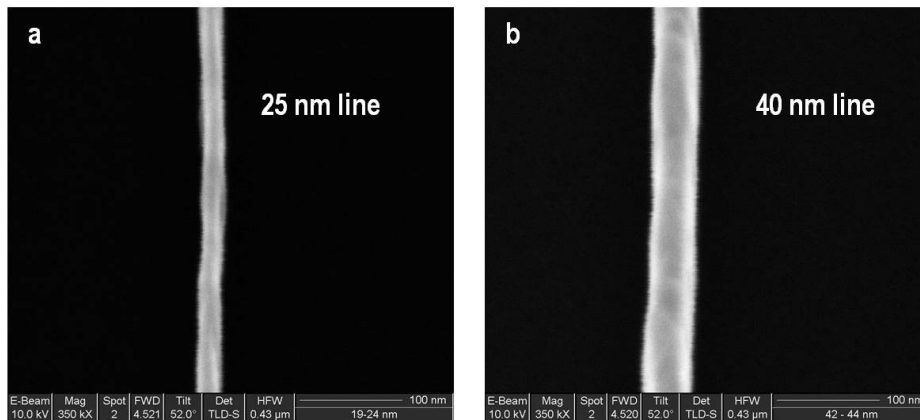


Figure III.3 High magnification SEM micrographs of (a) a nominal 25 nm line and (b) of a 40 nm line.

### 3.1.2 AFM Tips and Experimental Setup

A variety of probes were tested at the beginning for the measurement of the mechanical stability of nanostructures. For the ASAP 300 structures, stiff cantilevers in the normal and lateral direction were necessary, otherwise the cantilever is only deflected without damaging the structures. Regular LFM probes, most commonly silicon nitride probes, do not provide sufficient stability in the normal direction. Thus, silicon cantilevers with reflective coating originally designed for tapping mode were used for the AFM collapsing tests.

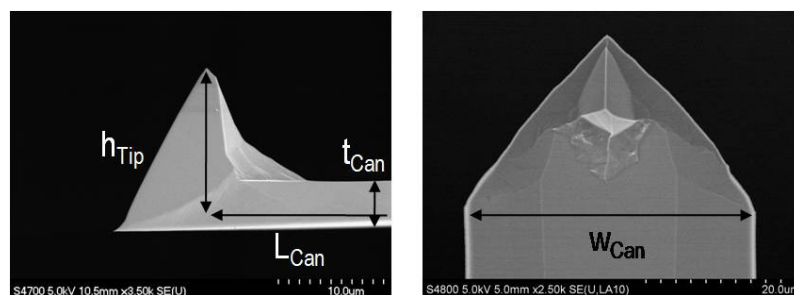
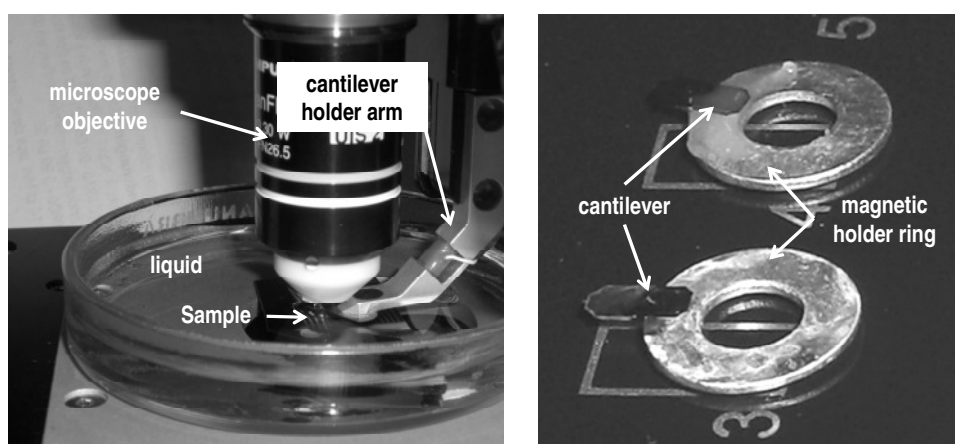


Figure III.4 SEM micrographs of AFM tip (side view and bottom-up view).



The drawback of the silicon tips is their vulnerability to wear when used on silicon samples. Regular dimension are  $130\ \mu\text{m}$  for the length ( $L_{can}$ ),  $30\ \mu\text{m}$  for the width ( $w_{can}$ ),  $4\ \mu\text{m}$  for the thickness ( $t_{can}$ ) of the cantilever, and  $15\ \mu\text{m}$  for the height of the tip ( $h_{Tip}$ ) (Figure III.4).

For the tests, several commercial AFMs were used, including the D3100 and D5000 (Digital Instruments, Veeco, Santa Barbara, Ca, USA) and the WITec alpha 300A (WITec GmbH, Ulm, Germany). All tests in liquid media were performed with the latter instrument, which requires the attachment of the cantilever to a magnetic holder ring (Figure III.5).



**Figure III.5 Setup of AFM in liquid media (left) and cantilevers fixed to the magnetic holder ring with adhesive (right).**

As the AFM part of the setup will be immersed into liquid (Figure III.5), the adhesive for the attachment needs to be compatible with the liquid in order to prohibit swelling of the bonding agent. Typically a nitrocellulose-based nail polish is used as an adhesive, except for the alcohols (section 3.1.4) where the former is not chemically stable enough. Thus, it was replaced by a special two-component silicon polymer (Reprorubber<sup>®</sup> Thin Pour from Flexbar Machine Corporation, Islandia, NY, USA). The drawback of this material is a limited adhesion on the magnetic holder ring which prevents its use in de-ionized water. Additionally, the microscope objective has to be compatible with the liquid, which excludes liquids like acetone.

### 3.1.3 Silicon Nanoparticles and Preparation Methods

Studying solid bridging (2.1.3) with real device structures is difficult because of the small overall area in contact with the neighboring structure. Nanoparticles were chosen as a test material because of their high surface-to-volume ratio. The relatively

large quantity of surface allows a large number of contact points between the particles and, therefore, sites for solid bridging. Additionally, the overall material volume involved in the solid bridging is large enough for the measurement with standard bulk methods such as X-ray powder diffraction.

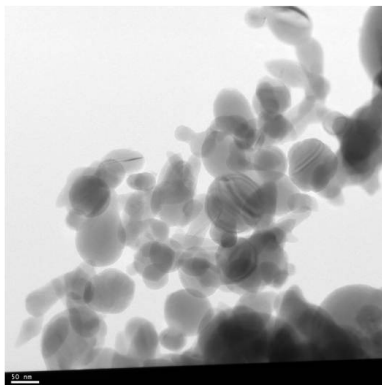


**Figure III.6 TEM brightfield image of the silicon nanoparticles. The length scale marked on the lower left corner equals 50 nm. TEM image courtesy of Technical Faculty CAU Kiel.**

For a comparable length scale to STI structures, 50 nm silicon particles were chosen and purchased as a powder from Nanoamor (Nanostructured & Amorphous Materials, Inc., Houston, TX, USA). The manufacturer claims a purity of 99.5 %, with copper as the major impurity. A pure silicon surface is not stable in an ambient atmosphere due to the oxygen and water vapor causing surface oxidation [88]. The particles were stored in a desiccator in order to reduce this oxidation.

For the solid bridging tests, the particles were dispersed in de-ionized water with the help of ultrasonics (Allpax, Type Palsson) for ten minutes in order to mimic a cleaning process and to have a reproducible starting point. The concentration was adjusted to be close to the dispersion limit of  $0.3 \text{ gL}^{-1}$  in order to ensure sufficient testing material. The experiments were carried out with 420 mL liquid in standard 500 mL polyethylene flasks.

### 3.1.4 Chemicals

The most important properties of the chemicals used for the experiments are listed in this section (Table 3) to provide a comprehensive overview to the reader. The properties include density, surface tension, viscosity (dynamic and kinematic), speed of sound, and the electrical permittivity.

**Table 3 Physical properties of the liquid chemicals used for the AFM experiments from [89] at standard conditions (T = 298 K, p = 1013 hPa) unless otherwise noted.**

category	media	density	relative permittivity	dipole moment	viscosity	surface tension	kinematic viscosity	speed of sound
symbol		$\rho$	$\epsilon_R$	$\mu_{Di}$	$\eta_{vis}$	$\gamma_l$	$\eta_{kin}$	$v_{sound}$
units		g/cm <sup>3</sup>		10 <sup>-30</sup> Cm	kg/m s	mN/m	m <sup>2</sup> /s	m/s
gas	air	0.001	1		0.02		15.7 10 <sup>-6</sup>	331 <sup>13</sup>
alcohols	methanol	0.791	32.7	5.67	0.55	22.6	0.70	1103
	ethanol	0.789	24.6	5.77	1.06	22.8	1.34	1207
	isopropanol	0.785	19.9	5.54	2.27	22.8 <sup>3</sup>	2.89	1272
	butanol	0.810	17.5	5.84	4.21	25.2	5.20	1239 <sup>12</sup>
water based	water	1	80.4 <sup>1,2</sup>	6.07	0.89 <sup>3</sup>	72.8 <sup>3</sup>	0.89	1497 <sup>8</sup>
	S30 <sup>10</sup>	1.121	76.7 <sup>1,2</sup>	n. a. <sup>9</sup>	2.9 <sup>7</sup>	74.2 <sup>6</sup>	2.59	1591 <sup>8</sup>
	S40 <sup>11</sup>	1.196	73.1 <sup>1,2</sup>	n. a.	6.0 <sup>7</sup>	74.9 <sup>6</sup>	5.02	
surfactant	CTAB <sup>4</sup>	1	n. a.	n. a.	0.89	35 <sup>4</sup>	n. a.	n. a.
	CAPB <sup>5</sup>	1	n. a.	n. a.	0.89	~35 <sup>5</sup>	n. a.	n. a.
isopropanol/water	4 %	0.99	77.5 <sup>1,2</sup>	n. a.	1.3 <sup>3</sup>	50 <sup>3</sup>	n. a.	n. a.
	7.5 %	0.98	74.9 <sup>1,2</sup>	n. a.	1.5 <sup>3</sup>	42 <sup>3</sup>	n. a.	n. a.

<sup>1</sup> T = 293 K;

<sup>2</sup> [90];

<sup>3</sup> [91];

<sup>4</sup> Cetyltrimethylammoniumbromid (CTAB) concentration:  $c = 1$  mmol [92];

<sup>5</sup> Cocamidopropyl betaine (CAPB)  $c = 2.5$  %vol [93];

<sup>6</sup> [94];

<sup>7</sup> [95];

<sup>8</sup> [96];

<sup>9</sup>n. a. = not applicable;

<sup>10</sup> S30 = mixture of sucrose with de-ionized water at  $c = 30$  %w;

<sup>11</sup> S40 = mixture of sucrose with de-ionized water at  $c = 40$  %w;

<sup>12</sup> T = 298 K [97];

<sup>13</sup> T = 273 K

## 3.2 Analytical Techniques

The analytical techniques used for the characterization of the materials are reviewed in the following paragraphs. Emphasis is put on the non-standard techniques, whereas the standard ones are only briefly mentioned.

The mechanical stability of nanostructures is analyzed with the lateral force microscopy (LFM) technique which is based on the atomic force microscope (AFM). A calibration of the LFM is necessary in order to convert the voltage outputs of the AFM into force values, which is described more closely in section 3.2.1. The test sites on the sample and the respective damage are investigated by electron microscopy, both scanning (SEM) and transmission (TEM). The former is seen as a standard method; the latter is described in more detail in combination with the focused ion beam (FIB) preparation procedure and the elemental analysis techniques such as electron energy loss spectroscopy (EELS) and energy dispersive X-ray spectroscopy (EDX).

The characterization of the solid bridging phenomena with the silicon nanoparticles (section 3.1.3) is mainly based on the measurement of the size of the particles and the silicon oxide formation. The average size was estimated from X-ray powder diffraction (XRD) patterns in combination with Rietveld refinement and the microstructure module of the Fullprof software [98]. The average size was confirmed by TEM analysis on specific areas. Additionally, the TEM was used to visualize the location of the oxide on the particles with shape analysis and the energy filtered TEM (EFTEM) technique. The overall silicon oxide formation was studied on the surface with X-ray photoelectron spectroscopy (XPS). The qualitative analysis of the silicon oxide was performed with  $^{29}\text{Si}$  nuclear magnetic resonance (NMR). The dispersion liquid (de-ionized water) was inspected for silicates with electro spray ionization mass spectrometry (ESI-MS).

### 3.2.1 Lateral Force Microscopy

The lateral force microscopy evaluates the friction (torsion, or left – right) signal in contact mode AFM. It allows the application and measurement of mechanical forces parallel to the surface. This was utilized for the measurement of the mechanical stability of nanostructures. In the following, the most common calibration procedures are reviewed with respect to rectangular cantilevers (Figure III.7) and reasonable

experimental effort. The latter is important because of the large numbers of cantilevers (overall >200) necessary for the tests. Emphasis is given to the relative accuracy between cantilevers, rather than the absolute values. Finally, the chosen direct force balance calibration [99] is explored with experimental data. For a wider and more general overview, the reader is referred to the reviews of Palacio and Bhushan [100] and Munz [101].

The AFM has to be calibrated for the conversion of the voltage output from the segmented photodiode into the respective force values. The calibration factor consists of two terms: first, the spring constant of the cantilever and second, the conversion constant from the optical system into the voltage of the photodiode. Both values can vary significantly from cantilever to cantilever due to manufacturing tolerances. Therefore, each single cantilever has to be calibrated.

A large number of methods for the calibration of the LFM are proposed in literature. These can be roughly divided into three categories: separate estimation of torsional spring constant and optical conversion constant, testing against a calibrated reference spring, and force balance between normal and lateral forces measured on differently sloped surfaces.

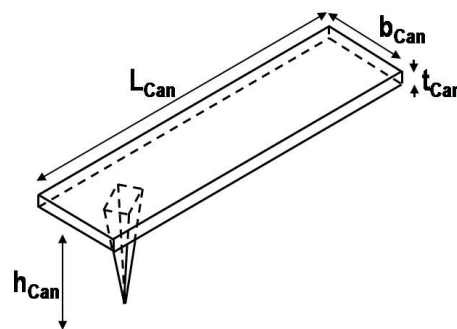


**Figure III.7 Scheme of a rectangular cantilever with a sharp tip.**

### 3.2.1.1 Normal Calibration

In the normal direction, the calibration is straight forward when using the generally accepted Sader method [102], especially for stiff cantilevers (several N/m). The measurements required for the Sader method are limited to the resonance curve and the plane view dimensions of the cantilever. For flexible cantilevers, the Hutter method [103] is more applicable, which depends on the agitation through thermal

noise. The normal spring constant  $k_N$  as determined by the Sader method is (equation [24])

$$k_N = 0.1906 \rho_{fl} b_{can}^2 L_{can} Q_f \omega_f^2 \Gamma_i^f(\omega_f) \quad [24]$$

where  $\rho_{fl}$  is the density of the surrounding fluid (air);  $b_{can}$  and  $L_{can}$  are the width and length of the cantilever, respectively;  $Q_f$  is the quality factor;  $\omega_f$  is the resonant frequency of the fundamental resonance peak; and  $\Gamma_i^f$  is the imaginary part of the hydrodynamic function introduced by equation [20] in reference [102]. The optical conversion constant in the normal direction can be derived by a force distance curve via the slope in the contact regime.

### 3.2.1.2 Separate Estimation of Spring Constant and Optical Conversion Factor

The lateral spring constant of a homogenous rectangular cantilever can be calculated from its geometry and shear modulus of the cantilever with beam theory as given in equation [25] [101]

$$k_\phi = \frac{G \cdot b_{can} \cdot t_{can}^3}{3 \cdot L_{can} \cdot h_{Tip}^2} \quad [25]$$

where  $G$  is the shear modulus,  $t_{can}$  is the thickness of the cantilever, and  $h_{Tip}$  is the height of the AFM tip. The measurement of the plane view dimensions ( $b_{can}$  and  $L_{can}$ ) can be done easily with a SEM. The thickness of the cantilever ( $t_{can}$ ) is in the range of a few microns and needs to be determined with high precision within a few nanometers. This accuracy can only be achieved by field emission SEM or indirectly through the use of beam mechanics in combination with the measurement of the normal resonance frequency [104]. However, this still requires the use of the shear modulus, which may not be known exactly for the cantilevers to be calibrated. Alternatively, the measurement of the torsional resonance frequency in combination with the plane view dimensions allows the calibration of the lateral spring constant without using the shear modulus [105]. This frequency is in the 1.5 MHz range for the cantilevers used (section 3.1.2) and could not be measured with the standard AFM equipment.

Additionally, the optical conversion factor has to be determined from the geometry of the optical path [106], lateral force vs. distance curves [107], or scanning across a vertical step [108]. The optical geometry is not an option because the optical path from the AFM systems used is not known in full detail. The lateral force distance

curves require a colloidal probe instead of the sharp tip as used for the experiments. Scanning across a vertical surface involves the very end of the tip moving across the edge of the structure. This exposes the most fragile part of the tip to the mechanical forces, which imposes a high risk of damaging the tip.

An independent determination of the lateral force calibration factor is not feasible due to the uncertainties involved in the calculation of the flexural spring constant and the experimental difficulties of establishing the optical conversion factor.

#### 3.2.1.3 Reference Spring

The concept of a calibrated reference spring shifts the calibration issue from the cantilever to a special device which can be more easily calibrated. The calibration of the cantilever itself is done by measuring the lateral forces that the AFM tip exerts on the calibration device during the scan. Several designs have been put forward and can be distinguished by the physical principle for the calibration of the reference: mechanical, electrical [109], and magnetic [110]. The mechanical method only shifts the calibration issue to another cantilever, which is desirable for complex cantilever geometries, like v-shaped ones. The advantage of electrical and magnetic systems is the introduction of independent physical properties that can be measured directly. For example, the microbalance of Cumpson et al. [109] based on a suspended MEMS structure with electrostatic comb drives, is a device that could be mass produced with reasonable cost and could profit from the considerable knowledge of MEMS design. However, these devices are non-trivial to design and not sold commercially today but if commercialized in the future, may offer a reliable and accurate way to characterize the lateral forces of the AFM.

#### 3.2.1.4 Force Balance

A force balance between normal and lateral forces can be obtained by measuring the forces on sloped surfaces in addition to the flat surface of a substrate. The relationship between the forces is defined by the angle enclosed by the surfaces. The “wedge” method [111] introduced this concept in 1996, with an addition for colloidal probes published in 2003 [112]. The advantage is the low experimental effort in terms of required equipment. A calibration grid with defined surfaces is the only necessary additional equipment, which can be (100) silicon with (111) surfaces etched by potassium hydroxide (Figure III.8).

The calibration data is acquired by scanning across the respective surfaces and evaluating the friction response. The scanning process induces significant wear especially for the silicon-on-silicon contact of the tip and the calibration grating. In addition, it is necessary to have a significant number of scans in order to get reliable data. A test was performed with five scans on each surface, with the result of an imaginary friction coefficient. Thus, more data and therefore more scans would be necessary with the disadvantage of increased tip wear. The latter could not be afforded, and so the method was disregarded.

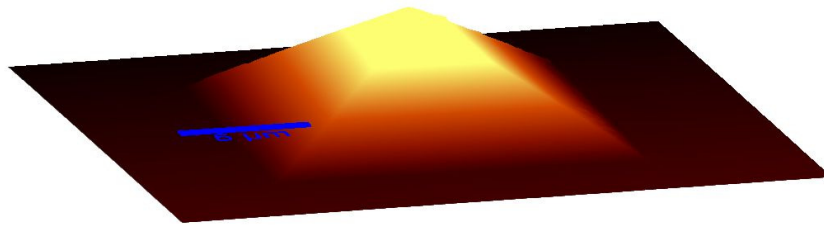


**Figure III.8 AFM measurement of the pyramidal calibration structure consisting of (111) surfaces in (100) silicon. The picture is inverted for better visibility (the pyramid is actually etched into the silicon). Blue scale bar corresponds to 5  $\mu\text{m}$ .**

### 3.2.1.5 Direct Force Balance

A similar method is the direct force balance [99], which requires force distance curves on the respective surfaces, with recording of the lateral signal instead of scanning over them (Figure III.9). The slopes of the force distance curves  $\Delta L_i$  in the contact regime are evaluated in combination with the normal spring constant and the angles of the surfaces  $\beta_i \in [-54.73^\circ, 0^\circ, 54.73^\circ]$  for (100) silicon with (111) etched surfaces.

The overall angle of the surface of the sample is considered negligible due to the high quality of silicon wafers. In addition to the lateral force constant  $S_{lat}$ , equation [26] also accounts for the detector misalignment  $\Delta D$  and the angle to the centerline of the force introduced by the off-center tip position on the cantilever  $\alpha$

$$(\Delta D + \Delta L_i)S_{lat} = k_N[\cos(\beta_i) \sin(\beta_i - \alpha)] \quad [26]$$

Five force distance curves on each surface were sufficient to create reliable data for the calibration procedure. The evaluation of the slopes was automated with a least squares fit on the approach curves in the contact regime (Figure III.9). These values were inserted into the equation system from the calibration reference, which was solved numerically [99].



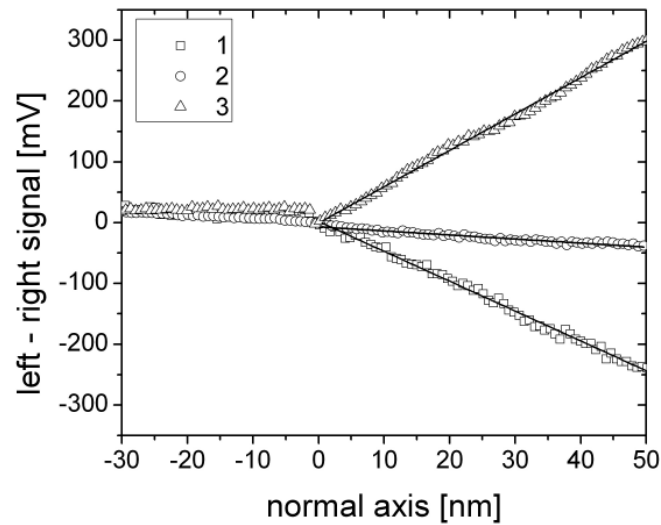


**Figure III.9 Lateral signal (approach part only) of the force distance curves on three different surfaces. The linear curve of the contact part is denoted with solid lines.**

For the evaluation purpose of the calibration procedure, it is also indicative to compare the average collapse forces (measured in one medium with different cantilevers). In the case of sugar solutions (S30 and S40), the deviation of the single cantilever values from the average collapse force is about 5 % (Table 4). The mechanical stability of the line structures also has some variations, which are included in the previous comparison. Thus, it is reasonable to assume a relative calibration uncertainty of 5 %.

**Table 4 Average collapse forces as tested with three different cantilevers**

Cantilever	A	B	C	Combined
Collapse force (average) [ $\mu\text{N}$ ]	4.5	4.0	4.3	4.3

More recently, an update for the evaluation procedure was published [113] that adds a sliding motion to the vector analysis of the forces during the force distance curves. This changes the equation for the lateral calibration factor [26] to two equations ([27] and [28]) (one for the approach and one for the retract curve) for the updated lateral calibration factor  $S_{lat_u}$

$$(\Delta L_i^A + \Delta D)S_{lat_u} = k_N[\tan \beta_i + \tan \alpha] - \frac{k_N \mu}{\cos(\beta_i)^2 + \mu \cdot \sin \beta_i \cos \beta_i} \quad [27]$$

$$(\Delta L_i^R + \Delta D)S_{lat_u} = k_N[\tan \beta_i + \tan \alpha] - \frac{k_N \mu}{\cos(\beta_i)^2 + \mu \cdot \sin \beta_i \cos \beta_i} \quad [28]$$

where  $\Delta L_i^A$  and  $\Delta L_i^R$  are the slopes of the lateral force distance curves on the approach and retract curves respectively, and  $\mu$  is the friction coefficient. In the case of negligible friction ( $\mu \rightarrow 0$ ) and an ideal placement of the tip ( $\alpha \rightarrow 0$ ), the equations [27] and [28] simplify to equation [29]

$$(\Delta L_i + \Delta D)S_{lat} = k_N \tan \beta_i \quad [29]$$

Comparing equation [29] with the original equation [26] for the same parameters ( $\Delta L_i, \Delta D, k_N$ ) gives equation [30]

$$\frac{S_{lat_u}}{S_{lat}} = \frac{\tan(\beta_i)}{\sin(\beta_i) \cos(\beta_i)} \quad [30]$$

This reduces to a factor of 3 for an angle of 54.73 degrees. The comparison of experimental calibration values (including friction) gives factors between 2.8 and 3.2, which are in reasonable range with the theory.

The sliding motion introduces the issues of the correct friction model and friction coefficients. Additionally, the analysis does not consider adhesion forces, which the tip needs to overcome before sliding. The absence of stick-slip friction behavior indicates that the original method is valid for the calibration presented in this work.

Another factor that could influence the calibration is tip wear. The main influence is the reduction of the moment arm, i.e. the height of the AFM tip ( $h_{Tip}$ ) by repetitive shearing of the end of tip. Typically, the calibration data is acquired prior to any collapse experiment, but when adding a post-calibration, only a small difference of 5 % compared to the pre calibration is seen. The post- vs. pre- calibration difference is in the range of the initial calibration uncertainty. Thus, the influence of tip wear on the calibration is minimal. Taking the initial measurement uncertainty into account, a relative error of less than 10 % can be assumed due to the fact that no other major influences are expected and have also not been observed.

The direct force balance calibration method is the method of choice because it is an experimentally reliable method in combination with economical experimental effort.

### 3.2.2 Transmission Electron Microscopy

For images with nanoscale resolution, the transmission electron microscope (TEM) is the tool of choice. Higher resolution is offered by the scanning TEM (HRTEM) which

uses a very sharp tip as an electron source that is scanned over the sample. Both techniques were used for the visualization of the damage on the tested line structures. Additionally, the size of the silicon nanoparticles and the location of the silicon oxide were analyzed by TEM.

High energy electrons are transmitted through the sample and are used for the analysis. In order to achieve sufficient signal strength in combination with reasonable acceleration voltages, the thickness of the sample is usually limited to a few 100 nm. As semiconductor samples exceed this thickness a special preparation technique was necessary. The focused ion beam (FIB) lift-out technique was used for the site-specific sample preparation, which is described as follows. First, a protective layer is deposited on top of the sample (e.g., carbon, platinum). Next, a trench is milled around the whole site of interest except for two small pieces that secure the membrane-shaped TEM sample to the substrate. After attaching a probe to the sample, the two connections to the substrate are cut with the FIB, and the sample is transferred to a TEM grid for analysis [114]. The previously described technique was used to study the damage produced by the LFM on the line structures. Specifically, it was used in combination with analysis of the materials in order to identify where the damage occurred inside the stack of materials of the line structure.

For a material-specific analysis, it is necessary to measure the energy loss of the transmitted electrons or to analyze the X-rays generated in the sample. When passing through the sample, some of the electrons interact with the electrons of the material (e.g., K shell) resulting in the ionization of the respective atoms. The energy loss of the high-energy electrons correspond to the ionization energies of the material atoms and can be used to identify the atoms and over a larger area via electron energy loss spectroscopy (EELS). An energy filter can be used to detect only those electrons with an energy loss of a specific element, which allows the generation of elemental maps as in energy filtered TEM (EFTEM). The ionized atoms are in an unstable state, and electrons from outer shells can jump relax into inner shells. During this process, the energy difference has to be emitted, which can be in the form of an X-ray quantum. An energy dispersive solid state detector is used to measure the number and the energy of the X-rays and also allows the identification of the material. For the visualization of the silicon dioxide on the silicon nanoparticles, the EFTEM and EDX techniques were used.

### 3.2.3 X-ray Photoelectron Spectroscopy (XPS)

An X-ray beam is used to illuminate the sample in order to generate photoelectrons from core levels or the outer orbitals. Only the irradiated surface layer with depth information of about 10 nm contributes to the measured signals. Photoelectrons are also generated in the bulk material, but these do not reach the surface without incoherent energy loss. Hence, these electrons do not carry the element-specific information and are not used in XPS. Analyzing the kinetic energy of the emitted electrons allows the identification of the material and the evaluation of the chemical state of the surface atoms.

The resolution of the XPS is sufficient to discern between the oxidation states of silicon by using the Si 2p signal. For the measurements performed during this PhD work an X-ray source with 1487 eV (Al  $K_{\alpha}$ ) was used. A more detailed analysis allows the estimation of the thickness of a silicon oxide film on top of a silicon material by a quantitative assessment of the respective peaks [115]. Also non-stoichiometric oxides can be distinguished from the silicon dioxide [115]. This technique was used to estimate the thickness of the oxide shell of the particles, as well as the identification of the oxide species.

### 3.2.4 Nuclear Magnetic Resonance Spectroscopy

The composition of the silicon and the silicon oxide in the nanoparticles was analyzed by the magic angle spinning NMR technique (MAS NMR). Lippmaa et al. demonstrated this possibility by measuring the chemical shift between the oxidized states of silicon with NMR [116]. The existence of sub-oxides was also studied with this technique. More specifically, a solid-state magic angle spinning method on the  $^{29}\text{Si}$  core was employed. 5 % of silicon consists of the  $^{29}\text{Si}$  isotope that is suitable for NMR experiments. Magic angle spinning is necessary in order to get sharper peaks than without spinning. NMR in liquid media was disregarded due to the expected dissolution and hydrolysis effects of the silicon oxide. For an explanation of MAS NMR, the reader is referred to the literature, e.g., reference [117].

### 3.2.5 Electro Spray Ionization – Mass Spectrometry

The dispersion of silicon nanoparticles was measured with electro spray ionization mass spectrometry (ESI-MS) in order to investigate whether silicates are present in the dispersion and to identify the dissolved species.

Mass spectrometry in combination with the electro spray ionization technique allows the measurement of non fragmented molecules, in contrast to the more established atomization ion sources like inductive coupled plasma. The material is dispersed in a liquid medium which is moved through a capillary into an electro spray where charged droplets are formed. In the spray, the droplets lose solvent and emit the charged molecules into the gas phase. There are two models for the emission process: the ion evaporation model, where charged jets extract the solute and the charged residue model, where all solvent evaporates and the charged residues remain and are then measured by the mass spectrometer.

For the formation of solid bridging, it has been speculated that residue in the form of silicates helps in the formation of bridging silicon oxide. Silicates in water can be measured by the ESI-MS, as shown by Pelster et al. [118], [119] and Schaack et al. [120].

### 3.2.6 Analytical Equipment

**Table 5 List of the main analytical tools used for this thesis.**

Technique	Model	Manufacturer / Lab
AFM	D5000	Veeco, Digital Instruments, Santa Barbara, CA, USA
	D3100	
	alpha 300A	WITec, Ulm, Germany
SEM	S4700, S4800, S5200	Hitachi High-Tech, Tokyo, Japan
	Expida 1265	FEI, Hillsboro, OR, USA
TEM	Tecnai F30 G <sup>2</sup> ST	FEI, Hillsboro, OR, USA; CAU Kiel
	3 <sup>rd</sup> party TEM labs contracted to measure the ASAP line structures	FELMI, Graz, Austria
		Nanolabs, San Jose, CA, USA
	EAG, Sunnyvale, CA, USA	
XRD	X'Pert	Panalytical, Almelo, The Netherlands
ESI-MS	Applied Biosystems (Applera), Mariner ESI-TOF	Life Technologies Corp., Carlsbad, CA, USA
NMR	3 <sup>rd</sup> party	University Bayreuth, Group: Prof. Senker

## **IV Results and Discussion**

Our research on the pattern collapse phenomenon of device structures can be divided into two fields: 1) the mechanical stability of nanostructures and its dependence on the surrounding media and 2) the phenomenon of solid bridging. In the following, a short summary of the most interesting results is given.

When the forces responsible for the pattern collapse phenomenon exceed the mechanical stability of the nanostructures, the respective structures will rupture. In order to analyze the breaking behavior, it was essential to measure this critical force. In the present work, an AFM was used in contact mode on 40 nm ASAP structures (section 3.1.1) to determine the breaking force of nanostructured polysilicon, a standard material in the semiconductor industry (section 4.1).

The AFM measurements were extended to 20 nm and 50 nm wide lines for the evaluation of the influence of the line width. In combination with finite element analysis, the experimentally obtained forces were used to calculate the internal stress at rupture and subsequently compared to the reported fracture strength (section 4.2).

As pattern collapse occurs when the structures are still wetted with the media, the influence of standard drying liquids (isopropanol and de-ionized water) on the fracture strength was studied (section 4.3). An increase in fracture strength was observed in alcohol. The importance of the solid-liquid interface vs. the bulk liquid was estimated in section 4.4. The solid-liquid interface was further evaluated by extending the range of tested chemicals to other alcohols, surfactants, and a self-assembled monolayer (section 4.5).

The solid bridging concept has been proposed, which bonds the free ends of the structures together after the removal of the liquid, for the elastic case of pattern

collapse (i.e., no rupture) (section 2.1.3). Silicon nanoparticles (section 3.1.3) were used to study solid bridging by exposing them to de-ionized water used by Si-based device manufactures (section 4.6).

#### **4.1 Pattern Collapse by AFM**

The mechanical stability of nanostructures was measured by atomic force microscopy. The AFM tip was scanned across the surface of the specimen. Instead of following the surface with the AFM tip, as in normal imaging, the AFM was used with low feedback settings in order to generate lateral forces on the structures in the path of the AFM tip. The contact point of the forces was always at the top section of the structure because of the higher aspect ratio of the structure compared to the AFM tip. The lateral forces were measured by the left–right (friction) signal of the segmented photo diode of the AFM. The direct force calibration procedure was used for the conversion of the voltage into forces.

The 40 nm ASAP structures (section 3.1.1) were tested and their collapse forces were in the range between 2-5  $\mu\text{N}$ . Euler beam mechanics using the reported fracture strength of polysilicon in combination with the measured line width variations (36–50 nm) yield similar values for the experimentally determined forces. Thus, when the structure is damaged, a fracture of the polysilicon is likely and not an interface failure, as expected initially.

Post-damage SEM investigations gave clear indications that the rupture occurred in the polysilicon structure. In the SEM pictures, a socket of several nanometers could be seen at the damaged sites. The rupture itself has a characteristic round shape indicating a conchoidal (clam-shell like) fracture. Thus, the fracture depended more on the stress distribution and less on material defects.

The size of the damage was between 500 nm and 1000 nm, increasing with the tip wear. There was always one round piece with a length of 500 nm, and if the damage was larger, additional sickle-shaped pieces were generated. The radius of the damaged sites was around 180 nm. Bended lines as reported by T. Kim et al. have not been observed. The closest resemblance to this was found for pieces that remained close to the original line structure. Nevertheless, high resolution SEM shows a clear fracture between the separated piece and the original line.

D. Peter, M. Dalmer, H. Kruwinus, A. Lechner, L. Archer, E. Gaulhofer, and W. Bensch; *ECS Trans.*, vol. 13, no. 2, p 323, 2008.

Reproduced by permission of ECS – The Electrochemical Society.

ECS Transactions, 13 (2) 323-330 (2008)  
10.1149/1.2908645 ©The Electrochemical Society

### Measurement of the Stability and Investigation of the Rupture Behavior of Semiconductor Line Nanostructures by AFM

Daniel Peter<sup>a</sup>, Michal Dalmer<sup>a</sup>, Hans Kruwinus<sup>a</sup>, Alfred Lechner<sup>b</sup>, Leo Archer<sup>a</sup>, Ernst Gaulhofer<sup>a</sup> and Wolfgang Bensch<sup>c</sup>

<sup>a</sup> SEZ AG, SEZ Str. 1, 9500 Villach, Austria

<sup>b</sup> Department of Microsystems Engineering, University of Applied Sciences Regensburg, Seybothstr. 2, 93049 Regensburg, Germany

<sup>c</sup> Department of Chemistry, Christian-Albrechts-Universität zu Kiel, Olshausenstr. 40, 24098 Kiel, Germany

The measured lateral stability of polysilicon line structures on a Silicon Oxy-Nitride layer is presented. This has been measured by Lateral Force Microscopy (LFM) in order to understand how much force can be applied to the structure during a wet cleaning process with subsequent drying. The measured values in the lateral dimension are between 2 and 5  $\mu\text{N}$  which is in the same range as expected by mechanical calculations. SEM micrographs of the damaged sites confirm a round breaking shape. The length of the broken line is around 0.5 to 1  $\mu\text{m}$  with a lower limit of 0.5  $\mu\text{m}$  which is similar to previously reported results on real damage produced by cleaning processes supported with Megasonic energy. The rupture in the AFM experiments occurs clearly in the polysilicon and not at the interfaces of the structure.

### Introduction & Background

The semiconductor industry is pursuing ever smaller technology nodes at the rate set by “Moore’s Law”. The drive to smaller structures has been accompanied by rising aspect ratios of several layers including stacked capacitors in DRAMs (e.g. AR = 20:1 (1)), shallow trench insulator (STI) structures and gate structures. Furthermore, possible post CMOS gate structures like FinFET are also high aspect ratio structures. The high aspect ratio makes these structures increasingly vulnerable to lateral forces which are for example generated in wet cleaning processes supported by Megasonic or spray systems. Additionally, a phenomenon called “pattern collapse” or “stiction” finally causes structures to stick together at the top. Pattern collapse in photoresist structures is attributed to surface tension effects in the drying step after the wet cleaning (2, 3). Cao’s model (3) assumes an unbalanced lateral force on a single structure due to either different spacing between the structures or different fill heights of the fluid inside the structures. Originally, the pattern collapse was attributed to a lack of adhesion of the photoresist on the layer beneath. This resulted in the improvement of the adhesion for example by micro roughening (4). Photoresist structures smaller than 0.2  $\mu\text{m}$  in width have also been reported to break inside the structure itself (5), thus not experiencing a lack of adhesion. Therefore, the breaking behavior of the polysilicon structures is also analyzed in order to identify the weakest spot in the line. However, the surface tension effect (capillary force) is just one explanation for pattern collapse. Other effects for example are the spin speed (i.e. centrifugal force) or the drag force of the fluid flowing around the structures or a lift



off process. To evaluate their influence on this effect it is necessary to compare the resulting force of these effects to the actual stability of the structure itself. In the present contribution we report the results of our measurements of the lateral stability of polysilicon line structures applying a LFM technique and compare the results with established theoretical models.

### Materials and Methods

Atomic force and lateral force microscopy (AFM/LFM) (figure 1, left) can be used to measure the (lateral) stability of nanostructures (6, 7). The main idea is to apply a lateral force with the cantilever tip to the structure. This force has to be sufficient to collapse the structure. The technical procedure used to cause pattern collapse is described in the following paragraph.

#### Collapsing Principle

In normal AFM imaging, the tip traces the surface when the height of the sample changes. Therefore, the z-Piezo voltage is adjusted so that the normal deflection of the cantilever stays constant (figure 1, right). When the AFM tip is scanning over a patterned sample, the AFM tip comes in contact with a structure at a distinct point. The point of the first contact is at the top part of the structure because the aspect ratio of the pattern is larger than the aspect ratio of the AFM tip. At this point the AFM tip is deflected because the cantilever keeps moving. This deflection causes the cantilever to twist like a torsional spring which can be measured by the lateral signal (left side – right side) of the 4 segment photo diode in the AFM. In normal imaging the z-Piezo would now be adjusted so that the tip moves over the structure. Instead for the collapsing procedure the z-Piezo is only minimal adjusted. Thus, the tip is deflected up to the point where the lateral force is larger than the stability of the line (figures 1 and 2).

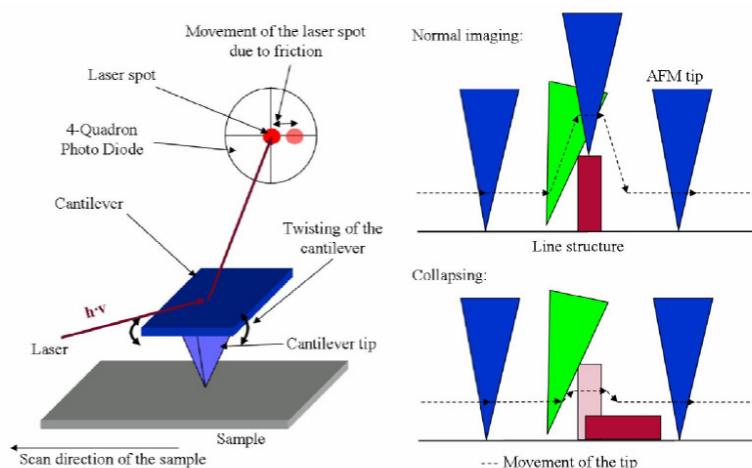


Figure 1. Principle of LFM (left) and proposed method of collapsing (right).

ECS Transactions, 13 (2) 323-330 (2008)

The structure collapses at this point and the tip deflection goes back to the friction values on the silicon surface. Thus, the maximum deflection voltage ( $U_{\text{Peak}}$ ) is a measure of the stability of the structure (figure 2). However, this voltage has to be converted into a force value through a calibration of the AFM. This calibration is necessary for each single cantilever since the alignment of the laser beam on the cantilever changes after each tip replacement. Additionally, there are significant manufacturing tolerances for the cantilever. After the calibration the voltage can be easily converted into the applied force ( $F$ ) by multiplying the maximum lateral voltage with the lateral calibration factor ( $S_l$ ) as given in formula [1].

$$F = S_l \cdot U_{\text{Peak}} \quad [1]$$

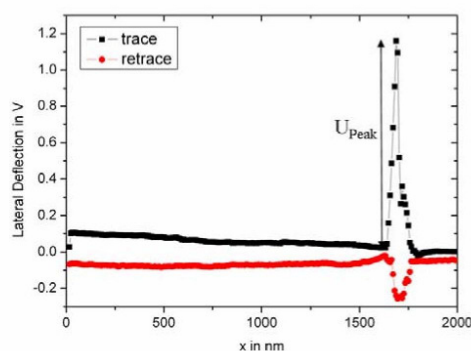


Figure 2. Lateral Deflection Signal of the AFM during the single line collapsing procedure.

#### Calibration of the LFM

Literature data agree on the calibration of the AFM in the normal direction but not in the lateral dimension. There are a lot of different suggestions in the literature for the lateral calibration which can be distinguished in three different approaches. Experimentally, by using a reference spring or by obtaining a defined mixture of normal and lateral signals or theoretically by combining the calculation of the spring constant and the constant for the optical system. The different models are briefly described in the following paragraph to explain the choice of the calibration method for the presented experiments.

The theoretical calculation of the spring constant is based on either the geometry and the material constant (8) or the thermal noise (9). However, these calculations require some critical measurements of the geometry e.g. the height of the AFM tip. Furthermore, the calibration of the optical constant (10) is not straightforward because it requires data from the manufacturer about the optical setup of the AFM head. The reference springs introduced in the literature (11, 12) share the common disadvantage of a very extensive

experimental setup either by producing and/or operating the reference spring. Therefore, we concentrated on the wedge methods (13, 14), which rely on a fixed mixture of normal forces and lateral forces on sloped surfaces. The original method is based on scanning over different crystal surfaces which require in the final analysis the correct estimation of the friction coefficient  $\mu$ . A variation of the wedge method is the direct force balance (15) which is based on force-distance curves on three different surfaces with a known angle to each other. This method has the advantages of a non scanning method which limits also the tip wear.

#### Investigated structures

The structures under investigation are the “damage lines” of the “ASAP300” wafers obtained from IMEC. The patterns are very long polysilicon lines (9500  $\mu\text{m}$ ) consisting of a stack of 100 nm polysilicon on top of a thin silicon oxy-nitride (2.4 nm) layer with a  $\text{SiO}_2$  cap of 50 nm. The line width is nominal 40 nm for the investigated structures. 10 lines are always grouped together with variable spacing (in our case 1  $\mu\text{m}$ ) as can be seen in figure 3. The experiments were performed on a DI Dimension 5000 using cantilevers with a lateral spring constant of approximately  $k_1 = 1000 \text{ N/m}$  (figure 3)

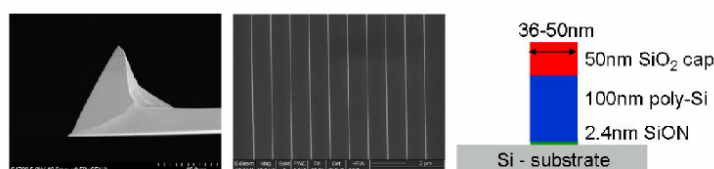


Figure 3. SEM micrograph of the type of AFM tip used for the collapsing experiments (left), SEM micrograph of the ASAP line structures investigated (middle) and the principle design of the patterns on the right side.

#### Experimental set-up

The general experimental set-up after the calibration consists of a pre-tapping mode scan, followed by the collapsing of the structure and the post analysis. The set-up is explained in more detail in the following paragraphs.

It is necessary to perform one pre-tapping mode scan over the area of interest for the positioning of the AFM tip. Additionally, the shape of the lines gives an indication of the size and therefore the wear of the AFM tip because an AFM image is always a convolution of the shape of the tip and the sample. In our case the convolution is dominated by the size of the AFM tip since the aspect ratio of the structure is higher than the aspect ratio of the AFM tip. However, this just gives an indication of the size of the AFM tip perpendicular to the line and not along the line, which is an important parameter because it can influence the length of the broken line. For the case of symmetric wear this is not as significant as it is for asymmetric wear. Therefore, a SEM post analysis of each AFM tip is performed to measure the exact sizes of the AFM tips.

Two different methods to collapse a pattern have been employed. The first one consists of scanning in contact force mode over a set of 10 lines with increasing normal force at the same spot similar to the method of Kawai et al. (6). The lateral force increases

ECS Transactions, 13 (2) 323-330 (2008)

linearly with the normal force and allows a good control of the lateral force which is applied to the structure. This procedure has the advantage of a straightforward comparison of the stability of the 10 lines (at one site) but the multiple scans over the lines could pre-damage the lines and therefore decreases the final force necessary for pattern collapse. Also, the tip wear is significant using this approach due to the relative large normal force. The second method consists of a single constant force mode scan through the pattern and back. The advantage of this approach is the limited number of scans in combination with a minimum normal force. This limits the tip wear to a minimum and avoids the formation of defects developed during previous contact mode scans.

Finally, a post tapping mode scan is performed on the collapsed line(s) to give a first indication on the shape of the fracture. For more detailed information SEM analyses were performed (Hitachi S5200, S4800 and FEI 1265).

All experiments were conducted in a class 100 clean room with 50 % rel. humidity.

### Results & Discussion

The direct force balance calibration method requires force-distance curves on three different surfaces (flat, positive and negative tilted) with a known angle to each other (figure 4). These surfaces were provided by a custom calibration grid, which is based on a (100) silicon wafer with anisotropically etched pits. On each surface five force-distance curves were recorded and an average was taken from their slopes, which resulted in overall calibration factors between  $S_1 = 2.8$  and  $4.4 \mu\text{N/V}$  for the used cantilevers with a max. experimental deviation of 10 % at  $1\sigma$  for each calibration.

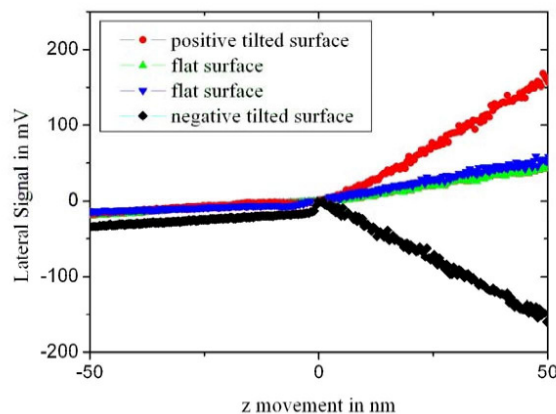


Figure 4. Lateral force distance curves on the three surfaces used for calibration, which is based on the direct force balance method.

Combining the calibration and the collapsing procedures described before yields collapsing forces between 2-5  $\mu\text{N}$ . These values are lower than the previously reported

values of around 23  $\mu\text{N}$  (16) and scatter over a larger range. A deviation of a factor of two between the weakest and strongest line can be easily found when using the first method.

The difference of the values obtained during our study to the previously reported results is attributed to the different calibration and measurement procedures. If one measurement is considered and the raw data evaluated with both procedures, the collapse force is 4  $\mu\text{N}$  for the direct force balance and 60  $\mu\text{N}$  for the method used by Kim. The main experimental difference is the scan speed where a speed of 2  $\mu\text{m/s}$  is used in this experiments compared to the previously reported speed of 0.1  $\mu\text{m/s}$ . However, our data does not indicate an influence of the collapsing speed (in the range between 0.4 and 10  $\mu\text{m/s}$ ) on the quantitative results.

A comparison between the experimentally obtained collapse values and the theoretically calculated values can be done using fracture mechanics. Polysilicon is a brittle material and shows fracture at a certain level of stress. The maximum stress at the bottom of a free standing line is calculated using the following formula with the assumption of a constant force along the length of the line (17)

$$\frac{F}{L} = \frac{\sigma_f \cdot w^2}{6 \cdot h} \quad [2]$$

with  $\sigma_f$  being the fracture stress,  $w$  is the line width and  $h$  the height of the line. A wide range of fracture stress for polysilicon lines is reported in literature, typically between 1 GPa (18) and 4.5 GPa (19). A mean value of 2.7 GPa for the fracture stress leads to collapse forces per length between 4.0 and 7.6 N/m for line widths of 36 and 50 nm respectively. If the usual length of a broken line (around 550 nm as shown in figure 5) is taken into account the model predicts a collapse force between 2.2 and 4.2  $\mu\text{N}$ . This fits well with the measured values between 2 and 5  $\mu\text{N}$ . However, the theoretical model applied for the calculation is very simple. Nevertheless, it provides an indication of the magnitude of the real collapse force.

The damage is very similar on all sites (see figure 5 as one selected example). The breaking shape of the line is exclusively round and narrowing at the bottom.

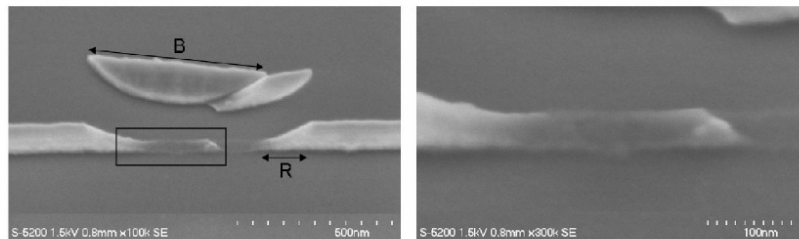


Figure 5. SEM micrographs of a collapsed line structure (left) with a magnification of the area marked by the black box on the left side showing the remaining bump of the line on the surface of the substrate.

The horizontal difference of the top to the bottom of one side of the rupture site (marked R in figure 5) is around 180 nm with a standard deviation of 25 nm (at one sigma) which is close to the measurement uncertainty of approximately 20 nm.

The structure breaks clearly in the polysilicon layer in our samples. Thus, there remains a small bump on the surface. This result is supported by TEM/EELS analysis. The EELS data show that the rupture did not occur at an interface of the stack but inside the polysilicon itself. Also, there were no bended lines observed. However, there are some rupture sites looking similar to bended lines especially at lower collapse speeds ( $<1 \mu\text{m/s}$ ) but more detailed SEM analysis reveals that in our case the structure was clearly broken away (figure. 6).

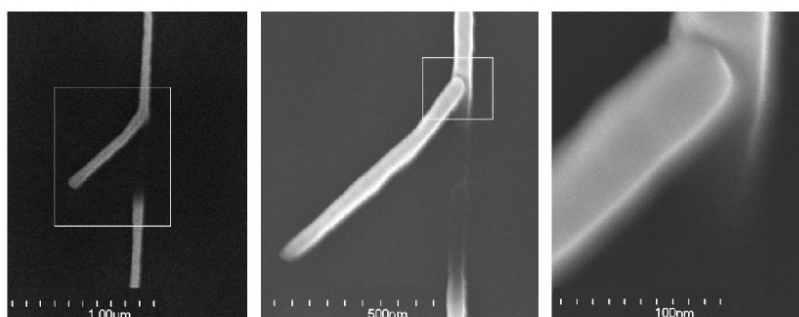


Figure 6. SEM micrograph of a quasi bended line with increasing magnification from left to right with the area of interest marked by the white box on the picture to the left.

The length of the overall broken line is varying but generally increasing with usage of the AFM tip. Thus, the AFM tip has a significant influence on the length of the broken line. Therefore, a replacement of the AFM tip is necessary as soon as significant wear occurs. At the top of the rupture site the length is normally between approximately  $0.5 \mu\text{m}$  and  $1 \mu\text{m}$ . The lower limit of approx.  $0.5 \mu\text{m}$  fits very well to the minimum length of damage published from Megasonic research on the same structures of  $0.55 \mu\text{m}$  (20). However, the length of the round broken piece (marked B in figure 5) is almost constant (average of 550 nm) only the number of pieces is increasing. At the position where the pieces are separated there is always a little bump as seen in figure 5. The bump still attached to the surface is another indicator that the polysilicon is the weakest layer in this stack in terms of the lateral stability and not the adhesion of the structure on the substrate.

It seems that the influence of the grain boundaries on the stability of the line is small because the long pieces exhibit almost the same constant length. Additionally, the round breaking shape, which is indicating a conchoidal fracture does not show any preferential breaking plane as would be expected when grain boundaries have a strong influence.



### Conclusion

An extensive set of AFM measurements yields a lateral stability for polysilicon line structures with a width of nominal 40 nm and a height of 150 nm between 2 and 5  $\mu\text{N}$ . The direct force balance method was applied for calibration of the AFM. The relatively large scatter for the collapsing forces can be explained with line width variations based on mechanical calculations.

SEM analyses of the collapsed patterns reveal a round breaking shape for all collapsed sites indicative for a conchoidal fracture. A strong influence of grain boundaries onto the lateral stability can be safely excluded. The results of the analyses demonstrate that the line structure breaks always in the polysilicon itself close to the interface but not at the interface. In addition, evidences are presented that the structures are broken and not bended as reported previously. The length of the broken lines is lower than 1  $\mu\text{m}$  with a lower limit of approximately 0.5  $\mu\text{m}$  which is similar to the smallest damage observed applying Megasonic or spray processes.

### References

1. Y. Park, Y. Ahn, S. Kim, K. Lee, C. Cho, T. Chung and K. Kim, *J. Kor. Phys.*, **44**(1), 112 (2004)
2. T. Tanaka, M. Morigami and N. Atoda, *J. Electrochem. Soc.* **140** (7), 115 (1993)
3. H. Cao, P. Nealey and W. Domke, *J. Vac. Sci. Technol. B*, **18** (6), 3303 (2000)
4. C. Brodsky, S. Bukofsky, D. Goldfarb and S. Halle, *U.S. patent*, 7229936 (2004)
5. J. Kitano and M. Honma, *Microlithography World*, (2004)
6. A. Kawai and Y. Kaneko, *Jpn. J. Appl. Phys.* **39**, 1426 (2000)
7. S. Kim, M. Jung, H. Kim, S. Woo and H. Lee, *Nanotechnology* **16**, 2227 (2005)
8. C. Gibson, G. Watson and S. Myhra, *Scanning*, **19**, 564 (1997)
9. C. Green, H. Lioe, J. Cleveleand, R. Proksch, P. Mulvaney and J. Sader, *Rev. Sci. Instrum.*, **75** (6), 1988 (2004)
10. E. Liu, B. Blanpain, and J. P. Celis, *Wear* **192**, 141 (1996)
11. P. Cumpson, J. Hedley and C. Clifford, *Vac. Sci. Technol. B* **23** (5), 1992 (2005)
12. R. Cannara, M. Eglin and M. Carpick, *Rev. Sci. Instrum.* **77**, 053701 (2006)
13. D. Ogletree, R. Carpick and M. Salmeron, *Rev. Sci. Instrum.* **67** (9), 3298 (1996)
14. M. Varenberg, I. Etsion, and G. Halperin, *Rev. Sci. Instrum* **74** (7), 3362 (2003)
15. D. Asay and S. Kim, *Rev. Sci. Instrum.* **77**, 043903 (2006)
16. T. Kim, K. Wostyn, P. Mertens, A. Busnainan and J. Park, *ECS Transactions*, **11** (2), 123 (2007)
17. J. Gere and S. Timoshenko, *Mechanics of Materials* PWS Publishing Company, 314 (1997)
18. F. Tardif and O. Raccurt, J. Barbé, F. de Crécy, P. Bessan and A. Danel, *ECS Proceedings* **26**, 153 (2003)
19. C. Muhlstein, S. Brown, *Mechanical Properties of Structural Films*, p. 67, ASTM International (2001)
20. C. De Marco, K. Wostyn, T. Bearda, K.-I. Sano, K. Kenis, T. Janssens, L. Leunissen, A. Eitoku and P. Mertens, et al., *ECS Transactions* **11** (2), 87 (2007)

## 4.2 Fracture Strength of Polysilicon in Nanostructures

The mechanical stability measurements with the LFM were extended to the line widths of 25 nm and 50 nm. Additionally, an FEA model was created resembling the line structure subjected to a point load, i.e., a force applied to a small area, in order to explain the fracture behavior of the line structures.

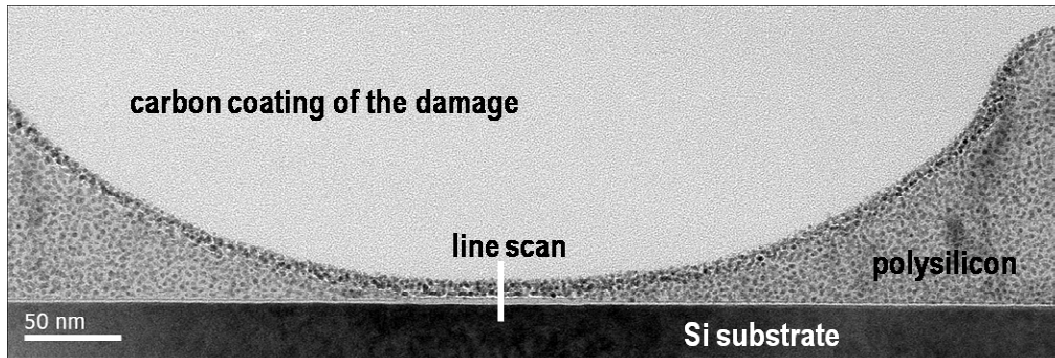


**Figure IV.1** TEM bright field image of a damage induced by AFM into the line structure. The viewing plane is orientated to the side of the line structure.

The damage generated by the AFM tip has a characteristic average length of 550 nm for all tested line widths (25, 40, 50 nm). TEM analysis of the damaged site confirmed the remaining socket at the bottom of the damage site (Figure IV.1), already described in section 4.1.

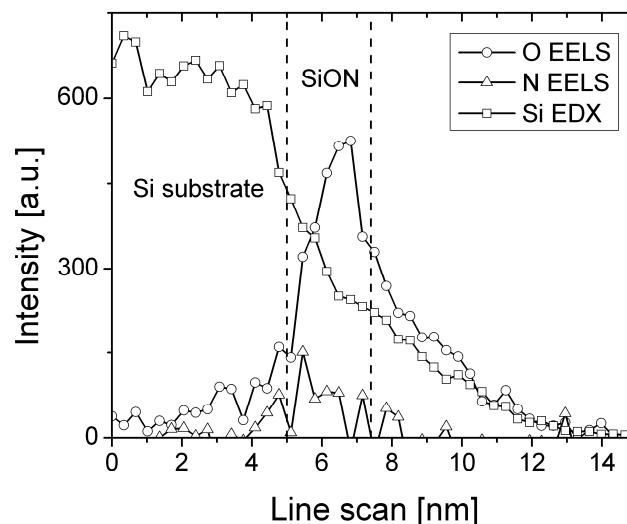


**Figure IV.2** TEM EELS scan at the bottom of the damage. Significant material remains above the silicon oxy-nitride layer.



An EELS line scan over this material with Si, O, and N signals showed that the silicon oxy-nitride layer remained intact and some oxidized polysilicon material was left on the top of that layer (Figure IV.2). Additionally, the TEM images established that the grain boundaries of the polysilicon did not influence the fracture line.

The three dimensional finite element models resembling the line structure under load were evaluated using the von Mises stress criterion. The stress distribution along the line is limited to approximately 200 nm in both directions of the area of force application. Hence, the average damage size may be attributed to the stress distribution. The maximum stress is found at the bottom of the structure at the interface with the substrate.

Using TEM analysis of the cross-section of the line structure, a corner rounding of 10 nm is found at the bottom of the structure (Figure III.2 b). Introducing the corner rounding to the finite element model shifts the maximum stress away from the bottom toward the top of the structure. Thus, the maximum stress did not occur at the material interfaces, which can explain the fracture inside the polysilicon.

The experimental data were compared to the theoretical model by calculating the mechanical force necessary for the reported fracture strength. A reasonable agreement was found for fracture strength of 3 GPa, which can be attributed to the reported fracture strength of polysilicon.

D. Peter, F. Holsteyns, M. Dalmer, H. Kruwinus, A. Lechner, and W. Bensch; *ECS Trans.*, vol. 25, no. 5, p 241, 2009.

Reproduced by permission of ECS – The Electrochemical Society.

ECS Transactions, 25 (5) 241-248 (2009)  
10.1149/1.3202659 ©The Electrochemical Society

### **Collapse Mechanisms for High Aspect Ratio Structures with Application to Clean Processing**

Daniel Peter<sup>a</sup>, Frank Holsteyns<sup>a</sup>, Michael Dalmer<sup>a</sup>,  
Hans Kruwinus<sup>a</sup>, Alfred Lechner<sup>b</sup>, and Wolfgang Bensch<sup>c</sup>

<sup>a</sup> LAM Research Corporation, SEZ Str. 1, 9500 Villach, Austria

<sup>b</sup> Department of Microsystems Engineering, University of Applied Sciences Regensburg,  
Seybothstr. 2, 93049 Regensburg, Germany

<sup>c</sup> Department of Inorganic Chemistry, Christian-Albrechts-Universität zu Kiel,  
Olshausenstr. 40, 24098 Kiel, Germany

The fabrication of semiconductor devices includes the generation of high aspect ratio structures which are prone to lateral mechanical forces. Therefore, the mechanical stability of polysilicon line structures has been tested by an AFM technique for several line widths. Additionally, the damage has been evaluated and shows a uniform size distribution. These experimental results have been compared to numerical models, in which the influence of specific geometries and material present in the stack has been studied. A stress concentration region at the bottom of the line was observed and could be removed by corner rounding (fillet). Besides, the maximum stress is shifted away from the substrate. The experimental damage showed a stump at the bottom of the damage, thus confirming the numerical results.

#### **Introduction & Background**

The fabrication of state of the art semiconductor devices includes the generation of high aspect ratio structures, i.e. the vertical dimension exceeds the lateral dimension multiple times. Such geometries are found e.g. in shallow trench insulation, capacitor over bitline and gate stacks. In the final devices the gaps between the structures are filled with e.g. dielectric materials for insulation and the filler can act as a mechanical support. During production, however, there are several process steps where such support has not been established yet. Consequently, these structures may be damaged if their lateral mechanical stability is exceeded during processing. A typical example is the wet cleaning step, which can produce such forces when ill adjusted. The most extreme forces are generated 1) during physical force assisted wet cleaning (1), such as droplet impact, exposure to transient cavitation and shock waves, and 2) during the subsequent drying step when capillary forces (2) are exerted on the structures. A good understanding of the mechanical stability of nanostructures is therefore essential to design a damage free particle removal and drying process. Additionally, due to the introduction of new geometries such as FinFET and the continuous downscaling to smaller technology nodes, the mechanical stability of the structures decreases and therefore damage free processing becomes more challenging (3). Thus, an accurate understanding of the damaging mechanisms of these structures is important for both the design of the structures itself (and its mechanical stability) and the tuning of the process steps such as wet cleaning.

In this paper, mechanical fracture tests were performed with an atomic force microscope (AFM) on polysilicon line structures to gain experimental data about its

mechanical stability (similar to 4, 5, 6, 7, 8). The lateral forces on three different line widths and the corresponding damages have been studied and compared to simulations of a lateral load on a beam. Furthermore, variations at the foot of the structures with the substrate, such as different materials and corner roundings are discussed with respect to stress distributions.

### Model & Experimental Procedure

#### Experimental Procedure & Material

A commercial AFM is used to apply a lateral mechanical force to the line structure to be tested (Figure 1). This force is set to exceed the mechanical stability of the structure and therefore generates damage. The lateral signal is recorded during this process and converted subsequently into the corresponding force value by using a calibration technique (9, 10). For more detailed information about the AFM induced collapse method the reader is referred to our previous publications (4, 5) and similar techniques in the literature (6, 7, 8).

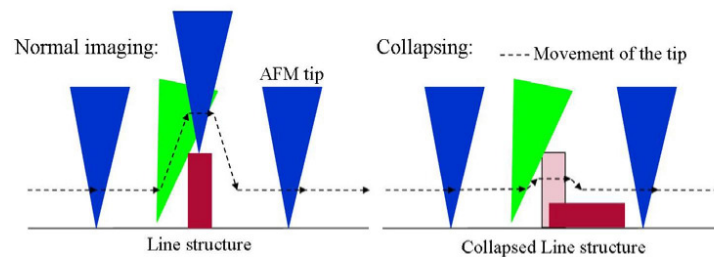


Figure 1. Normal AFM contact mode imaging (left) versus AFM collapsing principle (right).

The structures of interest are polysilicon line structures, which resemble gate stacks. The structures are stacks of 100 nm polysilicon on a 2.4 nm silicon-oxynitride layer with a 50 nm silicon oxide cap (hard mask) on top. The substrate is a 300 mm silicon (100) wafer. Three different line widths of nominally 25 nm, 40 nm, and 50 nm have been studied.

#### FEA Model

The finite element analysis (FEA) software Comsol Multiphysics was used for the simulation. The model (Figure 2) is based on a 3D beam, which resembles the gate stack used for the AFM experiments. It consists of a 100 nm polysilicon layer with a 50 nm silicon oxide hard mask layer on top. The line width is 40 nm when not noted differently. The overall beam is based on a 20 nm single crystal silicon layer with a clamped boundary condition at the bottom. For the corresponding material data see table 1. The other boundary conditions are free except for the force application area and the interfaces where a continuity condition applies. The symmetry of the force application allows the introduction of a symmetry plane to reduce the computational effort. The overall length of the structure is limited to 500 nm, where  $x = 500$  nm corresponds to the symmetry

plane. The force is applied perpendicular to the line structure (in y-direction (figure 2)) similar to the AFM experiment. The mesh consists of tetrahedral elements, which had to be constrained to a fixed number to limit the computational requirements to an acceptable level. The number of mesh elements was distributed non-homogenously with the densest mesh at the bottom of the polysilicon close to the force application area. The above description is for the standard model, deviations from this model are noted directly with the respective results. Nevertheless, the mesh element size could not be lowered sufficiently to resolve some effects in 3D e.g. corner rounding. For these cases two dimensional simulations were performed. The simulations itself are performed in quasi-static mode with increasing lateral force (0 to 10  $\mu\text{N}$ ).

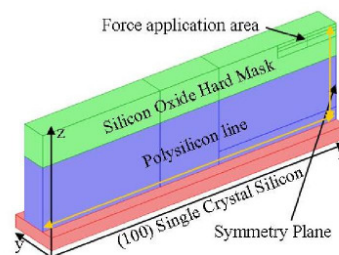


Figure 2. Three dimensional model of the simulated line structure with denoted orientations.

TABLE I. Material data for simulation.

Material	Elastic Modulus (used) [GPa]	Elastic Modulus (literature) [GPa]
Silicon oxide	70	74 (11)
Polysilicon	160	160 – 165 (12)
Single crystal silicon	170	130 (100) – 185 (111) (13)

## Results & Discussion

### Experimental Results

The AFM induced damage method generates a very uniform damage in the shape of a round rupture line as shown in Figure 3 (4, 5). Also, its size is constant with a length of the broken piece  $L$  (Figure 3) of around 550 nm in air with a point loading. Additionally, this length is independent of the line width between 20 and 50 nm and this characteristic length has been seen as a minimum damage size in Megasonics testing (1). Nevertheless, the literature reports various damage shapes with e.g. a flat rupture line at the bottom and almost perpendicular rupture lines, thus forming damage in the shape of a rectangle (6). Hence, there is a fundamental difference in the damage mechanism, which has been addressed by Wostyn et al. (14). Contrary to their results the polysilicon lines did not fail directly at the bottom but close to it. This has been confirmed by AFM measurements which show a stump of approximately 10 nm. TEM measurements also showed remaining material at the bottom of the round damage shape (figure 4) above the silicon substrate. Finite element analyses were performed in order to explain the root cause of the difference between the damage shapes.

ECS Transactions, 25 (5) 241-248 (2009)

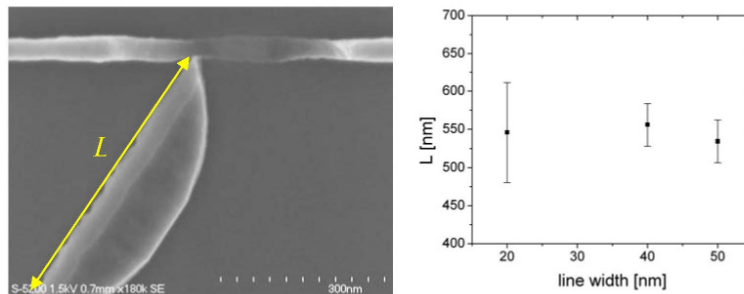


Figure 3. SEM micrograph picturing the characteristic round damage induced by AFM and the corresponding length of the damage distribution vs. line width (Error bar corresponds to  $1\sigma$ ).

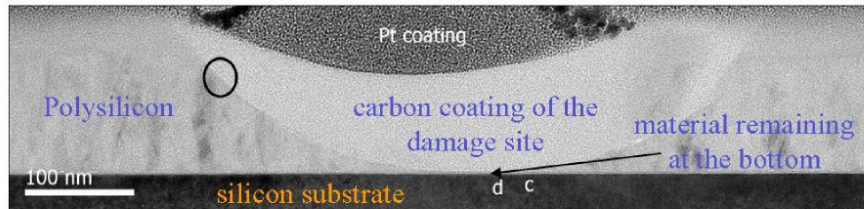


Figure 4. TEM micrograph of a damaged line structure with the point of view perpendicular to the line structure (viewing angle in y-direction).

Furthermore, for brittle materials such as polysilicon, the influence of notches on the fracture strength should not be ignored. So is the fracture strength of e.g. silicon already adversely influenced by small notches having a size of 1 nm (15). Nevertheless, the narrow distribution of size and shape of the experimental damage (Figure 2), indicates on the one hand only a very limited influence of small notches (seen in the standard distribution of the size of the damage). On the other hand the notches that have an influence are homogeneously distributed over the line structures (surface roughness) and therefore do not influence the damage shape.

The round shape of the rupture line (Figure 3 and 4) indicates a conchoidal fracture, which means that grain boundaries and defects have only a limited or negligible influence on the damage generation. This has been verified in TEM micrographs where different oriented grains can be seen as material contrast. The polysilicon grains are preferentially orientated perpendicular to the surface. The rupture line crosses these grain boundaries without any deviation from the round shape (e.g. circle in Figure 4). Thus, the grain structure of polysilicon does not effect the damage generation and shape in our samples.

#### Finite Element Analysis

**Basic model:** The numerical models were evaluated using the von Mises stress criterion, which allows a reduction of the general stress tensor to an uniaxial stress tensor at a fixed location. A smoothing function is applied to all spatially resolved stress distributions to



remove numerical instabilities from the simulation in order to allow the reader an easier understanding of the figures. The numerical instabilities may be resolved with higher mesh densities and hence higher computational effort. Nevertheless, the instabilities could be limited to a level which does not influence the results of this study and allow an efficient use of the computation time. The simulated results for the stress distribution, as a result of an applied force of  $3 \mu\text{N}$ , are shown in Figure 5 for the x- and z-direction (as indicated on figure 2). It can be observed that the maximum of the space-resolved stress distribution is located directly beneath the area where the force is applied and in this case situated directly at the interface of the silicon substrate, at the skin (in y-direction) of the structure. This indicates that the structure fails first at the bottom and then the rupture line continues to the top of the structure. The stress distribution shown for the x-axis is chosen just besides the maximum value in the z-height, since the maximum is difficult to solve numerically.

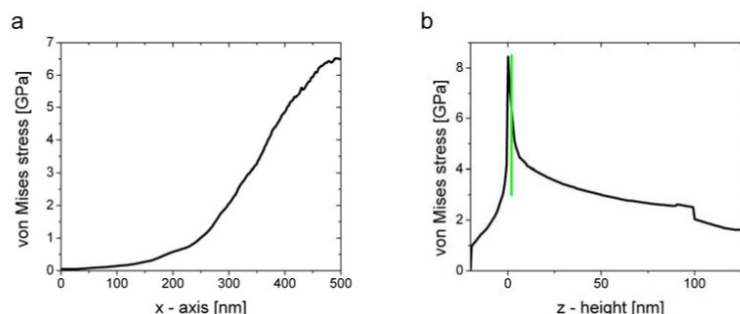


Figure 5. Stress distribution in x- (5a) and z-direction (5b) for an applied force of  $3 \mu\text{N}$  with the intersection marked by a vertical line. The location of the stress distributions is marked by arrows in figure 2.

**Materials & Interfaces:** The stress distribution given by the basic model differs from reality by variations of the stack material and corner rounding. Therefore, the influence of the materials on the maximum stress distribution normalized to the standard model is shown in Figure 6. According to the computation results the oxide hard mask increases the maximum stress compared to a line of polysilicon with the same dimensions. The hard mask introduces an abrupt change of the stress curve (Figure 5b) at a z-height of 100 nm. This can be explained by the drastic change in Young's modulus at the interface of polysilicon and silicon oxide in combination with similar strain conditions. The drop in the stress level can only be seen in a 3D model, it is absent in a 2D model, which represents only the cross section (Figure 7).

The introduction of the gate oxide layer (silicon oxy-nitride of 2 nm) to the model results in a lower maximum stress level. The reduction is influenced by the position of the gate oxide layer which is determined by the material loss in the real structures. In our structures this material loss was estimated to 2 nm by TEM measurement which was also used for the simulation (figure 6). Thus, the silicon oxy-nitride layer lowers the magnitude of the absolute stress. However, it also introduces two interfaces with lower fracture strength than the bulk material (14). Thus, it is more likely to result in a lower overall mechanical strength of the whole structure than without the small layer of silicon oxy-nitride.

ECS Transactions, 25 (5) 241-248 (2009)

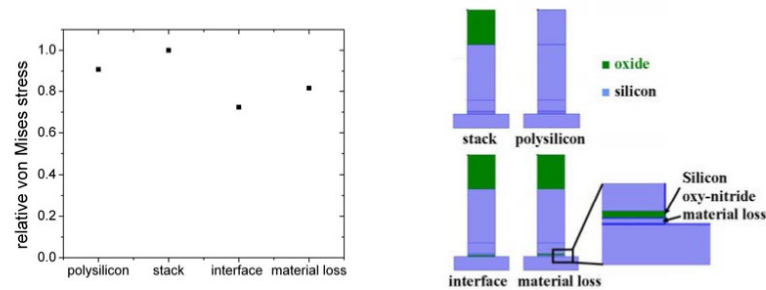


Figure 6. Influence of the materials on the maximum stress distribution normalized to the standard model of the stack.

**Corner Rounding:** The influence of the corner rounding on the stress distribution is shown in Figure 7 in terms of the location of the stress and the absolute maximum. The stress concentration at the bottom of the line structure (Figure 7b) can be removed by introducing a corner rounding also called fillet in mechanical engineering (16, 17) (figure 7b, inset). The largest effect in terms of reducing the maximum stress is seen with radii of the corner rounding above 8 nm in our model. Also, our structures showed a corner rounding of approx. 10 nm, which excludes large stress concentration effects in the experiments. The corner rounding influences certainly the location (in terms of z-direction, Figure 7) of the maximum stress, which is shifted in z-direction away from the interface. So, the corner rounding protects the interface from maximum stress and therefore reduces the chance for a rupture at the interface. TEM investigations confirmed that the rupture line does not touch the substrate, thus exhibiting this effect (Figure 4). This effect can explain the difference in the reported damage shapes in combination with the adhesion strength of the interface. On one hand the round rupture line is related to strong adhesion (or sufficient protection) at the interface. On the other hand a weak adhesion without protection (i.e. without corner rounding) would cause a straight rupture line because the interface is the weak layer (14) in addition to the location of the maximum stress which would make it more probable for the crack to propagate at the interface instead of the material. Hence, it would generate a flat rupture line. Nevertheless more efforts to support this hypothesis are required.

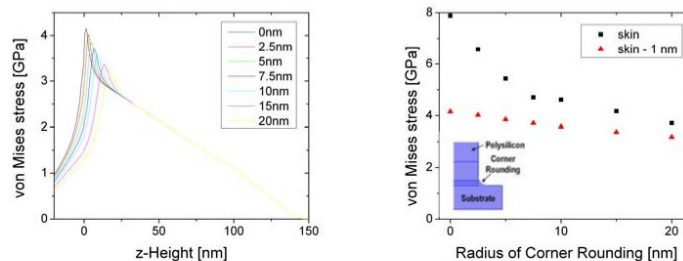


Figure 7. Von Mises stress distribution along the z-axis with varying corner rounding (left) and the maximum von Mises stress vs. the radius corner rounding (right).

**Fracture strength:** A comparison between the experimental collapse forces measured by the AFM induced damage technique and the calculated collapse forces by using the reported fracture strength is shown in Figure 8. The theoretical values are estimated by calculating the stress level vs. the corresponding applied forces. Then, the forces for the reported fracture stress levels ( $\sigma_F$ ) of 1 GPa (18), 2 GPa (19) and 3.3 GPa (20) are extracted and included into Figure 8 for the line width between 20 and 55 nm. There is a good agreement of the experimental values with fracture strength around 3 GPa, which is also an indication for a rupture inside the polysilicon. For comparison, there are reports on higher fracture strength of polysilicon (4.5 GPa (21)) and also on single crystal silicon with an even higher fracture strength of 7.7 GPa (22).

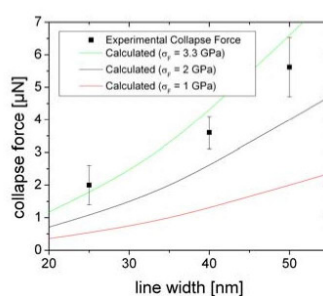


Figure 8. Comparison of experimental collapse force measured by the AFM induced damage method with the theoretical collapse forces by using reported fracture strength of polysilicon.

### Conclusion

A comparison between the experimental collapse force and theoretical fracture values has been performed on semiconductor line structures. The measured values were obtained by an AFM manipulating technique for several line widths (20 nm, 40 nm and 50 nm). Additionally, electron microscopy was done to analyze the damage shape, which showed an almost uniform size distribution independent of the line widths. The rupture line was exclusively round, which indicates a conchoidal fracture. Furthermore, detailed measurements revealed that the damage occurred inside the line and a stump remained at the bottom.

Finite element analyses have been performed to support the experimental results. The simulations show the maximum stress close to the interface between the line structure and the substrate. This maximum stress value is influenced positively by the gate dielectric material; however, the introduction of additional interfaces can reduce the fracture strength and therefore the mechanical stability. More pronounced is the effect of the corner rounding, which limits the stress concentration at the corner and also shifts the maximum stress level away from the interface. The results of the calculations are in full agreement with the experimentally observed damage occurring inside the line structures. Also, the combination of the experimental collapse forces and the expected theoretical values by using the fracture strength of polysilicon showed good agreement. Hence, the positive influences of the corner rounding of the line structure on the mechanical stability studied in this paper can also be applied to different structures for improved mechanical



ECS Transactions, 25 (5) 241-248 (2009)

stability. Nevertheless, attention should be paid to not adversely affect the electrical performance.

### References

1. C. De Marco, K. Wostyn, T. Bearda, K.-I. Sano, K. Kenis, T. Janssens, L. H.A. Leunissen, A. Eitoku and P.W. Mertens, *ECS Transactions*, **11** (2) 87 (2007)
2. H. Cao, P. Nealey and W. Domke, *J. Vac. Sci. Technol. B*, **18** (6), 3303 (2000)
3. F. Tardif, O. Raccurt, J.C. Barbé, F. de Crézy, P. Besson and A. Danel, *Proceedings - Electrochemical Society*, (26), 153 (2004)
4. D. Peter, M. Dalmer, H. Kruwinus, A. Lechner, L. Archer, E. Gaulhofer and W. Bensch, *ECS Transaction*, **13** (2), 323 (2008)
5. D. Peter, M. Dalmer, H. Kruwinus, A. Lechner, L. Archer, E. Gaulhofer, A. M. Gigler, R. W. Stark and W. Bensch, *ECS Transaction*, **16** (40), 13 (2008)
6. T. Kim, K. Wostyn, P. Mertens, A. Busnainan and J. Park, *ECS Transactions*, **11** (2), 123 (2007)
7. A. Kawai and Y. Kaneko, *Jpn. J. Appl. Phys.* **39**, 1426 (2000)
8. S. Kim, M. Jung, H. Kim, S. Woo and H. Lee, *Nanotechnology* **16**, 2227 (2005)
9. C. Green, H. Lioe, J. Cleveleand, R. Proksch, P. Mulvaney and J. Sader, *Rev. Sci. Instrum.*, **75** (6), 1988 (2004)
10. D. Asay and S. Kim, *Rev. Sci. Instrum.* **77**, 043903 (2006)
11. T. Yoshioka, T. Ando, M. Shikida and K. Sato, *Sensors and Actuators*, **82**, 291 (2000)
12. W.N. Sharpe Jr., B. Yuan and R.L. Edwards, *J Microelectromech S*, **6** (3), 193 (1997)
13. J.J. Wortman, R.A. Evans, *J. Appl. Phys.*, **36**, 153 (1965)
14. K. Wostyn, T.G. Kim, P. W. Mertens and J.G. Park, *Solid State Phenomena Vols.*, **145-146**, 55 (2009)
15. K. Minoshima, T. Terada and K. Komai, *Fatigue Fract Engng Mater Struct*, **23**, 1033 (2000)
16. J. D. Andrews, *Journal of Strain Analysis*, **26** (3), 153 (1991)
17. R. Solverson, *PhD thesis*, California Institute of Technology (1953)
18. S. Greek, F. Ericson, S. Johansson, M. Fürtsch and A. Rump, *J. Micromech. Microeng.*, **9**, 245 (1999)
19. W. N. Sharpe, Jr., K. T. Turner, and R. L. Edwards, *Experimental Mechanics*, **39** (3), 162 (1999)
20. J. Koskinen, J. E. Steinwall, R. Soave and H. H. Johnson, *J. Micromech. Microeng.*, **3**, 13 (1993)
21. C. Muhlstein and S. Brown, *Mechanical Properties of Structural Films*, p. 67, ASTM International (2001)
22. K. Komai, K. Minoshima and S. Inoue, *Microsystem Technologies*, **5**, 30 (1998)

### **4.3 Influence of the Chemicals Used for Semiconductor Drying on the Mechanical Stability of Nanostructures**

A similar procedure for the measurement of the mechanical stability of the nanostructures was employed as in the previous publications (sections 4.1 and 4.2). The 40 nm ASAP structures (section 3.1.1) were used as specimens for testing. The significant difference to the previous experiments was the immersion of the sample in liquids. Therefore, the influence of the chemicals on the collapse force of the polysilicon structures could be tested and compared to the previous results obtained in air.

When the sample was immersed in de-ionized water and propylene carbonate, only a negligible increase in the collapse force was observed. For the case of isopropanol, a significant increase by 50% of the mechanical stability was measured.

An explanation was found for the breaking of multiple pieces during the collapse procedure. The shape of the initial damage was always round. If the AFM tip at the contact point is smaller than the damage, it can pass through the previously generated hole in the line. However, if the tip is larger than the initial damage, e.g., due to tip wear, additional pieces will be ruptured from the line until the hole in the line is large enough to allow the passage of the tip.

The size of the initial damage was significantly influenced by the viscosity of the media, which was independent of the fracture forces. This could be shown by testing sucrose/water solutions and comparing the results with those obtained with de-ionized water. Both media have similar fracture forces around 4  $\mu\text{N}$ , but the initial damage size is 700 nm for the former and 780 nm for the latter. A maximum of the initial damage size is observed for de-ionized water with a viscosity of 0.9 mPas, and smaller rupture sizes were found for both lower and higher viscosities.

Finally, the influence of the speed of the AFM tip during the collapse procedure is tested with the three settings of 0.2, 2, 20  $\mu\text{m/s}$ . However, interestingly no influence on the fracture force could be observed.

D. Peter, M. Dalmer, H. Kruwinus, A. Lechner, L. Archer, E. Gaulhofer, A. M. Gigler, R. W. Stark, and W. Bensch; *ECS Trans.*, vol. 16, no. 40, p 13, 2009.

Reproduced by permission of ECS – The Electrochemical Society.

ECS Transactions, 16 (40) 13-21 (2009)  
10.1149/1.3108349 ©The Electrochemical Society

### Measurement of the mechanical stability of semiconductor line structures in relevant media

Daniel Peter<sup>a</sup>, Michael Dalmer<sup>a</sup>, Hans Kruwinus<sup>a</sup>, Alfred Lechner<sup>b</sup>, Leo Archer<sup>a</sup>, Ernst Gaulhofer<sup>a</sup>, Alexander M. Gigler<sup>c</sup>, Robert W. Stark<sup>c</sup> and Wolfgang Bensch<sup>d</sup>

<sup>a</sup> SEZ a division of LAM Research Corporation,  
SEZ Str. 1, 9500 Villach, Austria

<sup>b</sup> Department of Microsystems Engineering, University of Applied Sciences Regensburg,  
Seybothstr. 2, 93049 Regensburg, Germany

<sup>c</sup> Center for NanoScience (CeNS) and Department of for Earth and Environmental  
Sciences, Ludwig-Maximilians-Universität München,  
Theresienstr. 41, 80333 München, Germany

<sup>d</sup> Department of Inorganic Chemistry, Christian-Albrechts-Universität zu Kiel,  
Olshausenstr. 40, 24098 Kiel, Germany

Enhanced particle removal processes in wet cleaning of semiconductor wafers can cause significant lateral forces on surface structures. These forces have to be limited to below the stability of the (nano) structures on the surface to prevent damage. A mechanical fracture test based on atomic force microscope manipulation was used in liquid media (deionized water, isopropanol, and propylene carbonate) to measure the lateral stability of polysilicon line structures. The results are compared to previously reported results in air. All liquid media investigated here showed a stabilizing effect. Maximum stability was found for immersion in isopropanol. The size of the damage generated was mainly influenced by the viscosity of the liquids. The results do not support a stress corrosion cracking process.

### Introduction & Background

The process flow of a semiconductor wafer can include more than 100 cleaning steps as for example in a 65 nm DRAM process flow (1). Generally, the cleaning techniques can be categorized into two technologies: “dry” and “wet” cleaning. The former is based on plasmas or vapors and the latter on liquids e.g. the RCA cleaning sequence (2). Basically, three different types of material may have to be removed (cleaned) from the surface: metal ions, polymers, and particles. Etching the layer underneath the particles and stabilizing the particles in solution by an appropriate zeta potential is a successful method to remove particles. Since, the semiconductor industry is striving to smaller technology nodes, the requirements for material loss are getting increasingly strict, up to the point that under-etching alone will not be a feasible solution anymore (3). Therefore, the use of lateral forces for cleaning purposes on the wafer level was introduced by e.g. megasonic and aerosol systems in order to improve the particle removal. In order to prevent structural damage, however, the application of lateral forces has to be limited to below the stability threshold of the structures on the wafer. The structures that are most vulnerable to lateral forces are high aspect ratio structures such as stacked capacitors, shallow trench insulators, and gate structures. Besides the intentional forces there are also

ECS Transactions, 16 (40) 13-21 (2009)

inherent lateral forces during wet cleaning. Such lateral forces include drag forces by the fluid, centrifugal forces due to spin cleaning, and, most important, capillary forces during drying as modeled by Cao *et al* (4) for structures in close proximity. Their model assumes that the liquid is removed from the wafer surface except in-between the structures, where the capillary forces of the trapped fluid are exerting additional strain on the structures. The process window for successful particle removal by a non-destructive process is getting tighter with smaller technology nodes. In order to optimize the process parameters, a better understanding of the stability of high aspect ratio structures is required. The stability of nanostructures against lateral forces has mostly been characterized in air so far (5, 6, 7, 8).

However, wet processing takes place in liquid media which may affect the stability by a stress corrosion process or viscous effects that could affect the effective stability. In our contribution we present data on the stability of semiconductor line structures against lateral forces in liquid media.

### Material & Methods

#### AFM Induced Collapse

An atomic force microscope (alpha 300A; WITec, Ulm, Germany) was used in constant force mode as a lateral force microscope by recording the torsional signal (left – right signal) of the 4-segment photo detector (figure 1). We used commercially available silicon cantilevers (PPP-NCH; Nano-and-more GmbH, Wetzlar, Germany) with a lateral spring constant of approximately  $k_l = 1000$  N/m (figure 2). All cantilevers were backside coated by aluminum or gold for enhanced reflectivity. The tip was tracking the surface in permanent contact under a constant normal force by controlling the cantilever deflection induced by changes in sample topography.

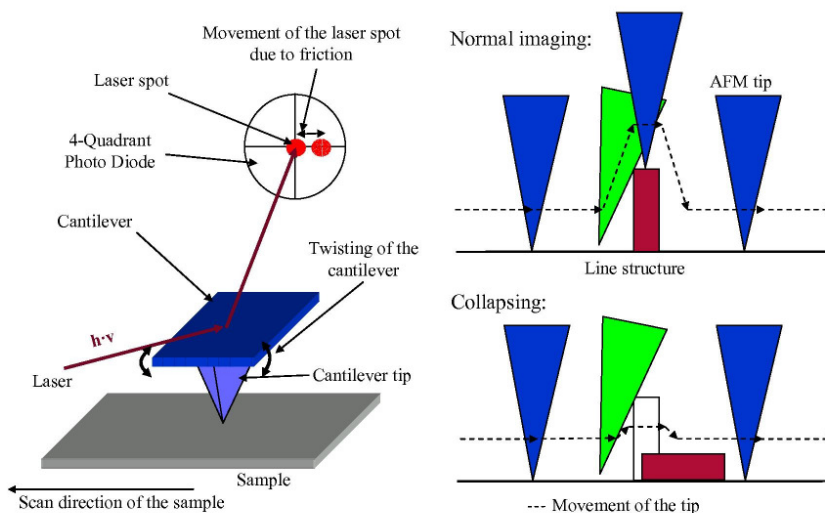


Figure 1. Principle of LFM (left) and proposed method of collapsing (right).

ECS Transactions, 16 (40) 13-21 (2009)

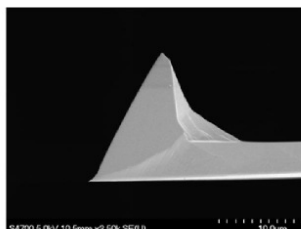


Figure 2. SEM picture of the type of AFM tip used for the collapsing experiments

The control parameters are changed for the collapse procedure. In this case, when the AFM tip comes into contact with the structure, it does not follow the topography, but exerts lateral forces on the structure. The following events occur:

1) The AFM tip touches the linear structure only on the top part, because of the high aspect ratio of the structure compared to the borderline of the AFM tip. Thus, all forces are applied on the top part of the structure (figure 1).

2) Without the topographic feedback, the tip is exerting a lateral force on the structure. The force is increasing proportional to the cantilever torsional stiffness up to the point where the stress induced by the AFM tip exceeds the fracture limit of the line structure. Thus, this technique allows a direct measurement of the lateral stability of nanostructures. However, for a quantitative analysis, a careful calibration is necessary. Each single cantilever has to be calibrated individually, because of changes in the optical detection system during the tip replacement and due to the significant tolerances of the cantilevers.

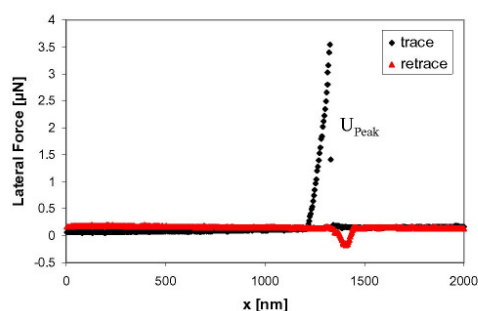


Figure 3. Lateral deflection signal of the AFM during the collapse procedure (trace). The retrace reveals the successful collapse.

The combination of the lateral calibration factor  $S_{lat}$  with the deflection during the collapse procedure (figure 3) gives the critical force  $F_{col}$  [1]

$$F_{col} = S_{lat} \cdot U_{peak} \quad [1]$$

#### Calibration Procedure

In literature, several ways to calibrate an AFM cantilever are documented. The most commonly used and widely accepted method for the normal deflection (top – bottom signal) is the Sader method (9). For the calibration of the torsional bending (left – right

signal) there are several different approaches. One approach is based on the theoretical calculation of the spring constant either from the geometry (10) or derived from the torsional resonance frequency of the cantilever (9). These methods only measure the lateral spring constant but do not provide an estimation of the optical transfer factor which has to be obtained separately (11). Another approach is the use of a reference spring with a known spring constant (12, 13) but these methods are either very extensive to manufacture or tedious to operate. A third approach is to use differently sloped surfaces to obtain a defined mixture of lateral and normal forces, commonly called “wedge methods”. The actual data can be obtained by either scanning across the surface (14, 15) or acquiring force distance curves on the respective slopes (16). Since a large number of AFM tips were used for the experiments discussed here, the latter method was used in the present work due to its experimental reproducibility and its simplicity. This so called “direct force balance” calibration requires force distance curves on three differently sloped surfaces (flat, positively, and negatively tilted). Such defined slopes were produced by anisotropic etching of a silicon-(100) wafer, causing pyramidal structures along the (111) crystal lattice.

#### Test structures

The structures under investigation were the so called “damage lines” of the “ASAP300” wafers from IMEC (Leuven, Belgium). The patterns were very long lines of polysilicon (9500  $\mu\text{m}$ ). The structures consist of a stack of 100 nm polysilicon on top of a thin silicon oxy-nitride (2.4 nm) layer with a  $\text{SiO}_2$  cap of 50 nm as shown in figure 4a. The nominal line width is 40 nm for the investigated structures with variation between 35 and 50 nm. Ten lines are grouped together with a spacing of 1  $\mu\text{m}$  (figure 4b).

The liquids used for the experiments include isopropanol (VLSI grade), propylene carbonate (UIPAC: 4-Methyl-1,3-dioxolan-2-one (Selectipur)), and de-ionized water (18.2 M $\Omega$ ) (Milli-Q). A solution of sugar in de-ionized water was prepared by mixing 30 wt% sacrose with de-ionized water, called sugar solution in the following.

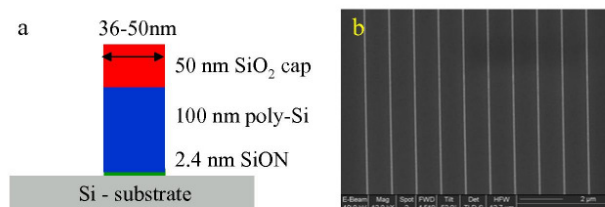


Figure 4. The principle design of the patterns (a) and a SEM micrograph showing a set of investigated ASAP line structures (b).

#### Experimental procedure

The general experimental procedure after calibration consisted of a preceding scan, followed by the controlled collapse of the structures and a subsequent assessment of the damage by another AFM-scan (figure 5). Preliminary defects of the line structures could be found in the preceding scan. The size and therefore the wear of the AFM tip can also be estimated from this picture. The apparent broadening of the line structures is due to the fact that an AFM image of any high aspect ratio structure is a convolution of the AFM tip



shape and the actual topography. In our experiments, the width of the line structures was smaller than the AFM tip. Therefore, the apparent width of the line structures was dominated by the geometry of the AFM tip.

The actual collapsing procedures described in literature are based on either single load (5, 8) or multiple load experiments (7, 17). A single load method was used as described in the section "AFM induced collapse". Subsequent analyses were performed on the collapsed line(s) by AFM and scanning electron microscopy (SEM) (Hitachi S4800). The SEM micrographs were used to obtain an accurate determination of the length of the fracture and the fragments broken off the lines (figure 7).

### Results and Discussion

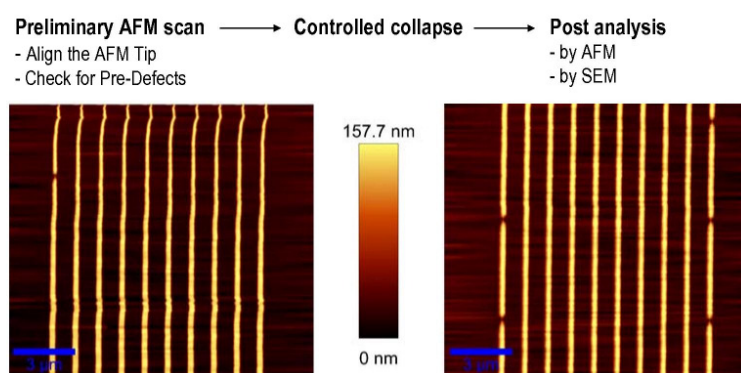


Figure 5. Experimental procedure including a preliminary (left) and a final analysis scan (right). The preliminary scan shows one pre-defect and the final analysis shows 5 collapsed sites.

To check the consistency of the lateral force calibration, a comparison was performed between the lateral calibration in air and in water. The experiments yielded lateral calibration factors of  $3.2 \mu\text{N/V}$  in air and  $2.6 \mu\text{N/V}$  in water. The difference may be attributed to the variation in the optical detection system due to the different refractive indices of the surrounding media. Thus, all lateral calibrations were performed in the respective media.

The combination of the calibration routine and collapse method yielded the actual collapse forces obtained in different liquid media which are shown in figure 6. A minor stabilization of the line structure was observed for de-ionized water ( $4.2 \mu\text{N}$ ), propylene carbonate ( $4.0 \mu\text{N}$ ), and sugar-solution ( $4.5 \mu\text{N}$ ) in comparison with its stability in air ( $3.8 \mu\text{N}$ ). In isopropanol the collapse force increased to almost  $6 \mu\text{N}$  which corresponds to an enhancement of about 50 %. However, the spread in isopropanol also increased by about 50 % compared to water. These results indicate that there was a stabilizing effect in liquid media compared to air.

ECS Transactions, 16 (40) 13-21 (2009)

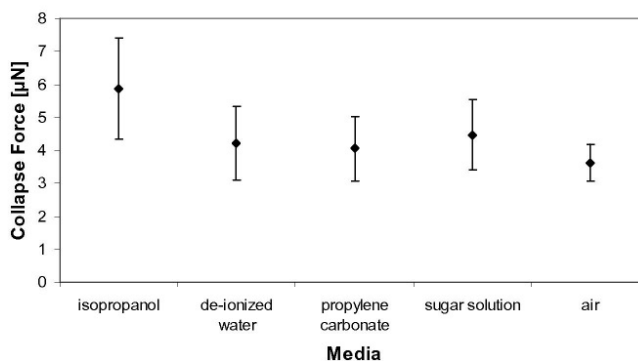


Figure 6. Average collapse forces of the experiments performed in various media. (error bars: standard deviation ( $1\sigma$ ))

The damage generated by the AFM tip was similar in all media including air. The yield line of the line structure was always round which indicated a conchoidal fracture. Differences were observed in the length of the broken line. The damage consists of up to 3 pieces (figure 7). The increase in the number of pieces coincides with the increasing wear of the AFM tip during measurements. This was especially experienced in de-ionized water (figure 5 left) in comparison to propylene carbonate (right). In a multi-piece breaking process, one piece always shows the round breaking shape similar to the one piece breaking process. The length of this piece (length of the longest broken piece) is very similar for the respective media (figure 9), especially in air where the standard deviation was in the range of the measurement uncertainty of the SEM pictures.

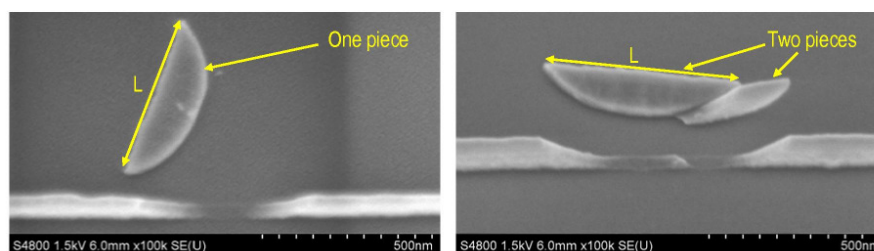


Figure 7. SEM micrographs of damage produced by AFM collapsing method using different sized tips

We explain the multi-piece breaking behavior by a two step breaking process. In the first step, the foremost point of the AFM tip (at 150 nm height) made contact with the line and breaks a single piece off the line (figure 8, step 2). However, the generated hole in the line was too small for the AFM tip to pass through the line (figure 8, step 3). Thus, the side of the AFM tip severed another piece of the line, which eventually allowed the passage of the AFM tip (figure 8, step 4). The corresponding lateral force signal (figure 8) showed two peaks, which is in accordance with the proposed model. Hence, the size of the AFM tip does not influence the initial formation of damage (step 2) and, thus, it does not affect the length of the longest (first) broken piece (marked L in figure 7).



ECS Transactions, 16 (40) 13-21 (2009)

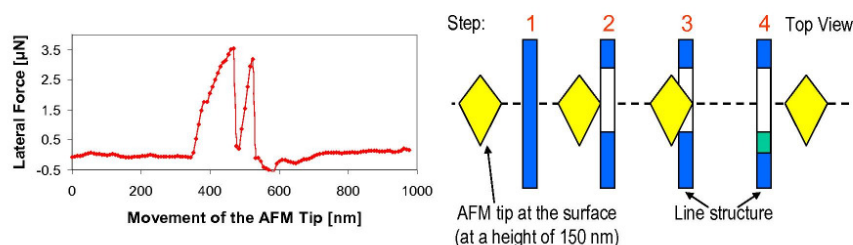


Figure 8. Lateral forces during a double fracture process and the corresponding model. The left side shows a lateral force curve during a two piece collapse experiment and the right side illustrates a cartoon of the proposed model of a multi-piece breaking process.

The length of the longest broken pieces (figure 7) shows a narrow distribution in the respective media especially in air, isopropanol, and the sugar solution (30 - 40 nm at  $1\sigma$ ). A small increase in the spread was observed for deionized water (60 nm at  $1\sigma$ ) (figure 9). The main influence on the length of the longest pieces broken off the line was the viscosity of the fluid. It decreased from an average of 780 nm for water ( $\nu = 0.9$  mPas at 298 K (20)) over 750 nm for isopropanol ( $\nu = 2.0$  mPas at 298 K (20)) to 700 nm for the sugar-solution ( $\nu = 2.9$  mPas at 298 K (21)). Nevertheless, there was no clear indication of a relationship between the viscosity and the fracture force which was similar for the sugar-solution ( $4.5 \pm 1.1$ )  $\mu\text{N}$  and for de-ionized water ( $4.2 \pm 1.1$ )  $\mu\text{N}$ .

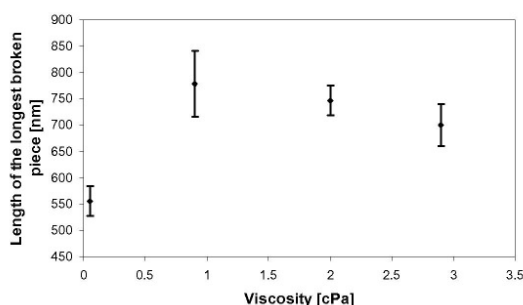


Figure 9. The length of the longest broken piece (figure 7) vs. the viscosity of the media.

Up to now, the fracture force (3.8  $\mu\text{N}$ ) determined in air was taken as the reference value and the results suggest a stabilization of the structures in liquid media. However, it is also possible to shift the reference to the maximum value in isopropanol and then a decrease would be observed in the sugar solution, deionized water, air, and propylene carbonate. This opens another possible way for explaining the fracture behavior by stress corrosion cracking (SCC) which has been reported for macro-scale  $\text{SiO}_2$  (20) in media with lone-pair electrons opposite proton donor sites (e.g. water). On the other side SCC was not observed for single crystal silicon in aqueous environments (21). In the case of polysilicon, SCC in humid air was observed in high-cycle fatigue experiments (22). Thus, as the structures under investigation consist of a stack of polysilicon and  $\text{SiO}_2$  it is not possible to rule out SCC from the material point of view.

ECS Transactions, 16 (40) 13-21 (2009)

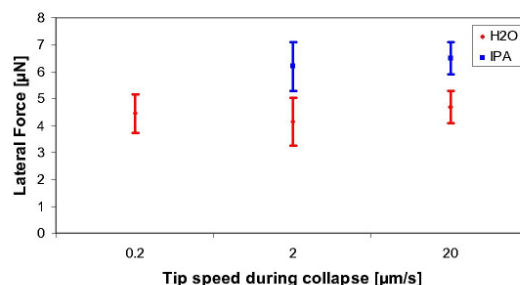


Figure 10. Average fracture force vs. AFM tip speed during collapse in deionized water and isopropanol.

An SCC process would also indicate a dependency of the fracture force on the respective tip velocity, because of the limited speed of the crack propagation. In our experiments such a dependency could not be observed (figure 10). With respect to the SCC process reported by Michalske (20), an essential element is the hydrogen donor possibility of the corrosive molecules. This is absent in the propylene carbonate case, but no significant difference in terms of fracture force could be observed for example to deionized water which can donate hydrogen atoms. The combination of our experimental results, the lack of velocity dependence as well as the absence of a chemical dependence (i.e. hydrogen donors), indicate that a SCC process does not occur, especially not the one reported by Michalske.

### Conclusion

The fracture of polysilicon nanostructures with a SiO<sub>2</sub> cap layer due to lateral forces has been investigated by AFM manipulation. Fracture forces were measured in various liquid media. An increased stability was observed for all liquids as compared to measurements in air. In de-ionized water this effect was less pronounced compared to isopropanol where an average increase of 50 % in the fracture force was observed with an increased spread.

The shape of the debris was round in all tested liquid media and air. This observation indicates a conchoidal fracture or clamp-shell-like fracture. Differences occurred in the length of the generated damage. An influence of the size of the AFM tip could safely be excluded on the initial damage formation. The length of the initial damage was mainly influenced by the viscosity of the liquid. Nevertheless, a relationship between the damage size distribution and the fracture force could not be found. In addition, experimental evidence was presented to exclude the stress corrosion phenomena from the observed breaking process (single loading).

ECS Transactions, 16 (40) 13-21 (2009)

## References

1. [http://www.solid-state.com/display\\_article/250829/5/none/none/Feat/Using-mixed-fluid-jet-bombardment-for-advanced-particle-remova](http://www.solid-state.com/display_article/250829/5/none/none/Feat/Using-mixed-fluid-jet-bombardment-for-advanced-particle-remova), Oct 22<sup>nd</sup>, 2008
2. W. Kern and D. A. Puotinen, *RCA Rev.*, **31**, 187, 1970
3. ITRS, Front End Processes, 3, 2007
4. H. Cao, P. Nealey and W. Domke, *J. Vac. Sci. Technol. B*, **18** (6), 3303 (2000)
5. D. Peter, M. Dalmer, H. Kruwinus, A. Lechner, L. Archer, E. Gaulhofer and W. Bensch, *ECS Transaction*, **13** (2) 323 (2008)
6. T. Kim, K. Wostyn, P. Mertens, A. Busnainan and J. Park, *ECS Transactions*, **11** (2), 123 (2007)
7. A. Kawai and Y. Kaneko, *Jpn. J. Appl. Phys.* **39**, 1426 (2000)
8. S. Kim, M. Jung, H. Kim, S. Woo and H. Lee, *Nanotechnology* **16**, 2227 (2005)
9. C. Green, H. Lioe, J. Cleveleand, R. Proksch, P. Mulvaney and J. Sader, *Rev. Sci. Instrum.*, **75** (6), 1988 (2004)
10. C. Gibson, G. Watson and S. Myhra, *Scanning*, **19**, 564 (1997)
11. E. Liu, B. Blanpain, and J. P. Celis, *Wear* **192**, 141 (1996)
12. P. Cumpson, J. Hedley and C. Clifford, *Vac. Sci. Technol. B* **23** (5), 1992 (2005)
13. R. Cannara, M. Eglin and M. Carpick, *Rev. Sci. Instrum.* **77**, 053701 (2006)
14. D. Ogletree, R. Carpick and M. Salmeron, *Rev. Sci. Instrum.* **67** (9), 3298 (1996)
15. M. Varenberg, I. Etsion, and G. Halperin, *Rev. Sci. Instrum* **74** (7), 3362 (2003)
16. D. Asay and S. Kim, *Rev. Sci. Instrum.* **77**, 043903 (2006)
17. B. Baumeister, T. Jung and E Meyer, *Applied Physics Letters*, **78** (17), 2485 (2001)
18. D. Lide, *CRC Handbook of Chemistry and Physics*, 6-241 – 6-245, CRC Press, London
19. M. Migliori, D. Gabriele, R. Sanzo, B. Cindio and S. Corraera, *J. Chem. Eng. Data*, **52**, 1347 (2007)
20. T. Michalske and S. Freiman, *J. Am. Ceram. Soc.*, **66** (4), 284 (1983)
21. B. Wong and R. Holbrook, *J. Electrochem. Soc. Solid-State Sci*, **134** (9), 2254 (1987)
22. H. Kahn, R. Ballarini, J. Bellante and A. Heuer, *Science*, **298**, 1215 (2002)

## 4.4 Influence of the Bulk Liquid Media vs. the Solid-Liquid Interface

The experimental technique of the AFM used in liquid media is the same as in section 4.3. Based upon our previous results on the polysilicon structures, further liquids and mixtures were tested.

The increase of the mechanical stability of polysilicon nanostructures in isopropanol compared to de-ionized water was confirmed by measurements in isopropanol/de-ionized water mixtures. By adding 2.5 %v/v isopropanol into the de-ionized water the same results as in 100 % isopropanol could be obtained. As isopropanol is accumulated on the solid-liquid interface of the silicon oxide, only the interface and not the bulk liquid influenced the fracture strength. Tests in propylene carbonate supported this assumption. First tests showed a similar collapse force as in de-ionized water due to condensation and subsequent accumulation of water molecules at the solid-liquid interface. Dipping the sample into isopropanol prior to the test in propylene carbonate gave the same values as for 100 % isopropanol. Thus, for the fracture strength, only the solid-liquid interface seems to be important.

The damage was mainly influenced by the viscosity of the media where the maximum damage was observed in de-ionized water. The decrease of the damage size at lower viscosities was confirmed by measurements in methanol ( $\eta_{vis} = 0.6$  mPas) leading to sizes of 680 nm for the damages. High viscosities were achieved by using a 40 %w sucrose/de-ionized water solution with  $\eta_{vis} = 6.0$  mPas, resulting in sizes of 580 nm. Similar collapse values for the de-ionized water and the sucrose/water solutions indicated that the damage size is independent from the collapse force.

A two-step rupture model is proposed, where the initial step determines the fracture strength and the second step determines the damage formation. For the fracture strength, only the solid-liquid interface is important, where a surface stress corrosion process probably supports the crack initiation. The subsequent damage is then determined by the viscosity of the liquid.

D. Peter, M. Dalmer, H. Kruwinus, A. Lechner, A. M. Gigler, R. W. Stark and W. Bensch, *J. Micromech. Microeng.*, in press

IOP Publishing Ltd. ©

## Measurement of the mechanical stability of semiconductor line structures in drying liquids with application to pattern collapse

Daniel Peter<sup>1</sup>, Michael Dalmer<sup>1</sup>, Hans Kruwinus<sup>1</sup>, Alfred Lechner<sup>2</sup>, Alexander M Gigler<sup>3</sup>, Robert W Stark<sup>4</sup> and Wolfgang Bensch<sup>5</sup>

<sup>1</sup> LAM Research AG, SEZ Str. 1, 9500 Villach, Austria

<sup>2</sup> Department of Microsystems Engineering, University of Applied Sciences Regensburg, Seybothstr. 2, 93049 Regensburg, Germany

<sup>3</sup> Center for NanoScience (CeNS) and Department of Earth and Environmental Sciences, Ludwig-Maximilians-Universität München, Theresienstr. 41, 80333 München, Germany

<sup>4</sup> Center of Smart Interfaces, TU Darmstadt, Petersenstr. 32, Darmstadt, Germany

<sup>5</sup> Department of Inorganic Chemistry, Christian-Albrechts-Universität zu Kiel, Olshausenstr. 40, 24098 Kiel, Germany

### Abstract

Enhanced particle removal processes in wet cleaning as well as drying processes of semiconductor wafers can cause significant lateral forces on surface structures. These forces, however, must not exceed the mechanical stability of structures on the wafer. Thus, a mechanical fracture test was used to assess the lateral mechanical stability of polysilicon line structures in relevant process liquids. The mechanical test was based on nanomanipulation with an atomic force microscope. Compared to fracture tests in air, data acquired in liquid media revealed a stabilizing effect. The size of the generated damage was influenced by the viscosity of the surrounding media. Best stability was found for immersion in isopropanol.

### Introduction

In the manufacturing process of a 65 nm DRAM product, each wafer is subject to more than 100 cleaning steps (1). Generally, the cleaning techniques can be categorized into two technologies: “dry” and “wet” cleaning. The former is based on plasmas or vapors, the latter on liquids such as the RCA cleaning sequence (2). A typical liquid cleaning technique is based on etching of the surface layer and rinsing the contamination e.g. polymers, particles, or metal ions from the surface. As the requirements for material loss are becoming increasingly strict, this limits the etching of the surface layer and therefore the choice of possible cleaning approaches (3). For example, physical force assisted cleaning systems such as megasonic and aerosol systems are currently under discussion. In particular in-plane forces, i.e. forces acting parallel to the wafer surface, are beneficial for particle removal. However, such forces have to be controlled to ensure damage-free processing of structured wafers.

High aspect ratio structures such as stacked capacitors, shallow trench insulators, and gate structures are very sensitive to lateral forces. These do not only occur in advanced cleaning processes, but also during basic wet processing due to drag forces in the fluid, centrifugal forces during spin cleaning, or capillary forces. The effects of capillary forces between structures in close proximity during drying were e.g. modeled by Cao et al. (4). This model is based on the

assumption that the liquid is removed from the wafer surface except in-between the structures, where the surface tension of the trapped fluid exerts additional strain on the structures.

All these forces need to be controlled for a non-damaging wet cleaning process. In order to ensure optimum process performance with future and therefore smaller technology generations, a better understanding of the stability of high aspect ratio structures is required. To this end, the stability of nanostructures with respect to lateral forces has been characterized mostly in air (5, 6, 7, 8). Nevertheless, the liquid media used in wet processing may also affect the stability of the nanostructures for example by stress corrosion processes or viscous effects. In the following we report the higher lateral stability of polysilicon line structures in isopropanol compared to water. Additionally, we found that the damage size is influenced by the physical properties of the liquid.

## Material & Methods

### AFM Induced Collapse

An atomic force microscope (alpha 300A; WITec GmbH, Ulm, Germany, [www.witec.de](http://www.witec.de)) was used to exert lateral forces on the nanostructures. The force was measured by recording the torsional signal (left – right signal) of the 4-segment photo detector. We used commercially available silicon cantilevers (PPP-NCH; Nano-and-more GmbH, Wetzlar, Germany) with a normal spring constant of approximately  $k_n = 30$  N/m and a lateral spring constant of about  $k_l = 1000$  N/m. All cantilevers were coated with gold on the detector side for enhanced reflectivity.

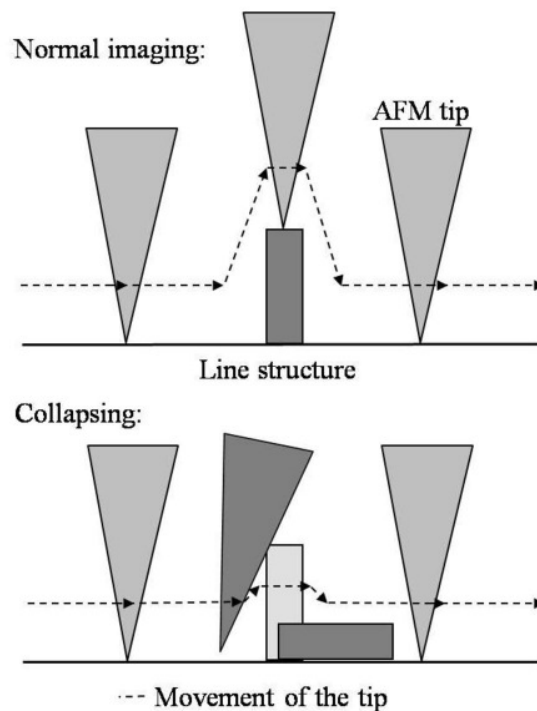


Figure 1. Principle of lateral force microscopy (above) and tip induced collapse (below)

To induce collapse of the line structures, low feedback parameters were used such that the AFM tip does not follow the local topography. Thus, the tip exerted lateral forces on the test structure. A schematic representation of the collapse procedure is shown in Fig. 1. Typically, the following events occurred:

1) The AFM tip touched the wall-like structure only on the top part, because of the high aspect ratio of the structure compared to the geometry of the AFM tip. Thus, all forces were applied on the top edge of the structure.

2) Without the topographic feedback, the tip was exerting a lateral force on the structure. The force increased proportional to the torsional stiffness of the cantilever up to the point where the stress induced by the AFM tip exceeded the fracture limit of the line structure (Fig. 2). Thus, the maximum lateral force signal provided a direct measure for the lateral stability of the nanostructures.

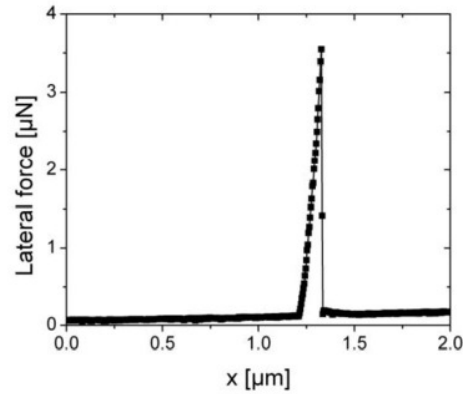


Figure 2. Torsion signal during the collapse procedure (trace). In the subsequent retrace in the opposite direction large lateral forces are absent indicating the collapse of the line structure.

#### Calibration Procedure

For a quantitative analysis, a calibration of every single cantilever is necessary. Thus, a unique lateral calibration factor  $S_{\text{lat}}$  was obtained for each AFM tip. The maximum lateral signal  $U_{\text{peak}}$ , which occurs shortly before rupture, is converted into the critical force  $F_{\text{col}}$  by [1]

$$F_{\text{col}} = S_{\text{lat}} \cdot U_{\text{peak}}. \quad [1]$$

The calibration of an AFM cantilever can be achieved for the normal (flexure) and lateral (torsion) direction of motion. The most commonly used and widely accepted method for the flexural bending (top–bottom signal) is Sader’s method (9). For the calibration of the torsional bending (left–right signal) various approaches exist (10, 11, 12, 13).

We calibrate our setup by measuring force-vs.-distance curves on differently sloped surfaces in order to obtain a defined mixture of normal and lateral forces. The original method is called “wedge method” and obtains the actual data by scanning on surfaces with different slopes (14, 15). A similar method, referred to as “direct force balance”, relies on the acquisition of force distance curves on the slopes (16). Three different slopes are needed with known angles to each other. Such defined slopes can be produced by anisotropic etching of a Si(100) wafer, which causes etch pits oriented along the (111) crystal lattice. A modified direct force balance technique was reported which utilizes both the approach and retract curves (17). As a large number of AFM tips were used in our experiments, the original direct force balance was chosen due to its experimental reproducibility.

#### Test Structures and Media

The structures for fracture testing were purchased from IMEC (Leuven, Belgium). The patterns consisted of lines with a length of a few millimeters. Each line consisted of a stack of 100 nm polysilicon on top of a thin silicon oxy-nitride (2.4 nm) layer with a  $\text{SiO}_2$  cap of 50 nm as shown in Fig. 3a. The nominal line width was 40 nm.

The liquids used for the experiments included isopropanol (IPA, VLSI grade), propylene carbonate (IUPAC: 4-Methyl-1,3-dioxolan-2-one (Selectipur), PC), and de-ionized water (DI water, 18.2 M $\Omega$ ) (Milli-Q). De-ionized water mixtures with sucrose were used to obtain higher



viscosities. Two solutions of 30 wt% and 40 wt% sucrose were prepared and are referred to as S30 and S40 in the following.

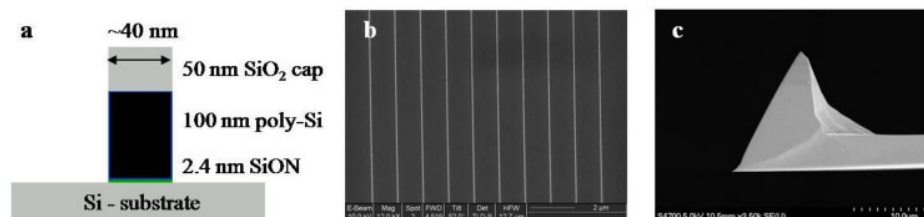


Figure 3. The design of the patterns (a) and two SEM micrographs showing a set of investigated line structures (b) and a typical AFM tip

### Experimental Procedure

The experimental procedure consisted of a preceding scan, a controlled collapse procedure and an evaluation of the damage by subsequent AFM-scan. The preceding scan was used to check the lines for defects and for the alignment of the tip and the line structures. It also confirmed that the lines were without defects. Prior to the collapse procedure, the AFM tip was aligned to the line structures.

The collapsing procedures described in literature are based on either single load (5, 8) or multiple load experiments (7, 18). A single load method was used as described in a previous publication (5). Subsequent analyses were performed on the collapsed line(s) by AFM and scanning electron microscopy (SEM). The SEM micrographs were used to determine the length of the fracture and the shape of the fragments broken off the lines.

## Results & Discussion

### Fracture Forces

As the optical path of the laser beam was affected by the refractive index of the medium, the lateral calibration had to be performed in the actual medium. In water, for example, the lateral sensitivity was 25% lower than for the same cantilever in air. The original direct force balance method was used for calibration. For comparison, also the modified method was applied and the results differed from the original one by a factor of 3. The relative results between the media, however, were not affected. In DI water, for example, this resulted in collapse forces of 4.2  $\mu\text{N}$  with the original method (16) and 12.6  $\mu\text{N}$  with the updated one (17). These values are similar to the results obtained in the media air, S30, S40, and propylene carbonate. All tests showed a standard deviation of less than  $\pm 20\%$ .

A significant variation in collapse force was observed when using IPA instead of water in the experiment. The collapse force increased by a factor of 1.4 compared to the force in pure DI water (Fig. 4). Additionally, 2.5 %v/v IPA in DI water showed similar results as for the 100 %v/v. This similarity indicates an accumulation of isopropanol at the surface. A similar effect may be causing the reduction of the etch rate of KOH on silicon with the addition of IPA (19, 20). Thus, the formation of a surface layer of IPA between the bulk liquid and the sample is reasonable, which affects the fracture strength.

For the tests in propylene carbonate, a significant difference to DI water was initially expected. However, similar results as for the latter were measured. As the tests were conducted in air, the humidity could condensate into the propylene carbonate and accumulated on the sample surface. For verification a sample was dipped into IPA and then immersed into propylene carbonate and tested. An increase of the collapse force to the levels of IPA was measured which confirmed the hypothesis that the main influence on the fracture strength is caused by the solid liquid interface.



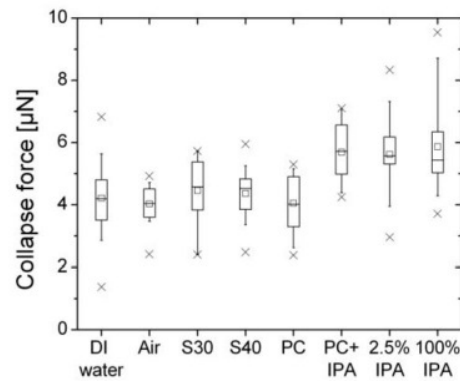


Figure 4. Box plot of the experimental collapse forces in various media. The box encloses 50 % and the whiskers start from 10 to 90 % of the data points closest to the average. The asterisks denote the extreme values which were measured. For every media there are data points from at least 20 different measurements except for S30 and PC+IPA (around 10).

#### Generated Damage

The shape of the damage generated by the AFM tip was similar in all tested media. The yield-line of the structure was always symmetrically curved which indicates a conchoidal fracture. Differences were observed in the lengths of the broken parts of the line. The corresponding debris usually consisted of a single piece only (Fig. 5). However, in the case of heavily worn tips, additional pieces were broken off from the line. The lateral force signal acquired during damage generation (Fig. 6, top) also showed multiple distinct peaks. The number of the force peaks matched the number of the debris pieces.

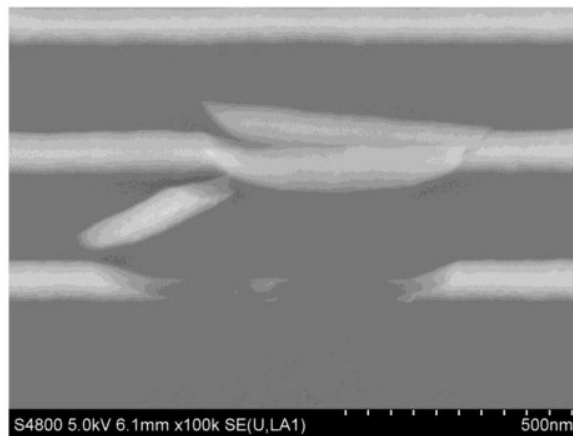


Figure 5. Visualization of the multiple piece fracture process by SEM. Here, only one piece was torn from the middle line and two pieces from the line at the bottom of the image. The AFM tip approached from the bottom of the picture. These damages correspond to step 2 for the middle and step 4 for the bottom line of the multiple piece fracture model.

This multi-piece breaking behavior can be explained by a multi step breaking process. In the first step, the foremost point of the AFM tip (at 150 nm height) gets into contact with the line and breaks a single piece away from the line (Fig. 6, step 2). The damage generated in the line is too small for the AFM tip to pass through (Fig. 6, step 3). Thus, the sides of the AFM tip sever additional pieces of the line, until the damage in the line is large enough to allow for the passage of the AFM tip (Fig. 6, step 4).

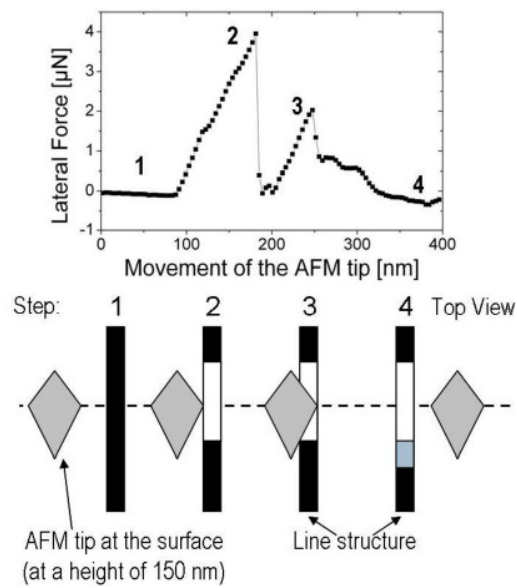


Figure 6. Lateral forces during a double fracture process and the corresponding model. The left side shows a lateral force curve during a two piece collapse experiment and the right side illustrates a cartoon of the proposed model of a multi-piece breaking process.

Nevertheless, wear is not an issue for the repeatability of the measurement because during step 2 of the damage formation the contact between the tip and the line structure can be considered as a point contact due to the wedge-form of the AFM tip. This condition is independent of the wear, because before the edge wears off a whole piece is broken from the tip resulting in a large wedge. Hence, the size of the AFM tip does not influence the initial formation of damage (step 2) and, thus, it does not affect the length of the longest (first) broken piece (marked  $L$  in Fig. 7 and 8).

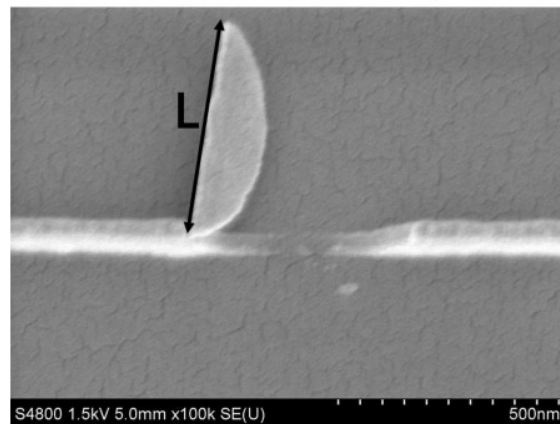


Figure 7. SEM micrograph of characteristic round damage as observed for tests in air. Sample covered in Pt for better contrast.

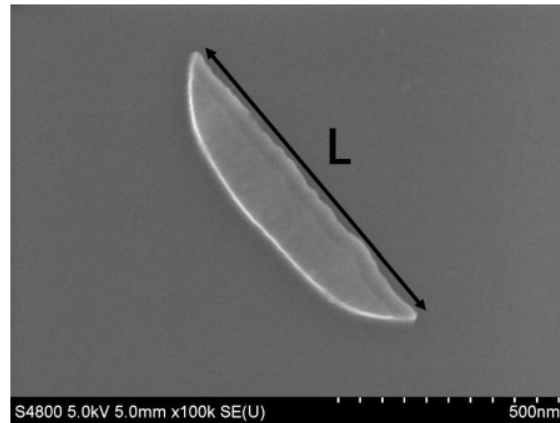


Figure 8. Characteristic generated damage piece for AFM tests in isopropanol.

The length of the first piece had a characteristic size in every medium (Fig. 7, 8, 9). The maximum average size of 780 nm was observed in DI water ( $\nu = 0.9$  mPas at 298 K (21)) and a slightly smaller average length of 750 nm for isopropanol ( $\nu = 2.0$  mPas at 298 K (21)). Further increase of the viscosity showed decreasing damage sizes of 700 nm and 580 nm for S30 ( $\nu = 2.9$  mPas at 298 K (22)) and S40 ( $\nu = 6.0$  mPas at 298 K (22)) respectively. Using methanol, which is less viscous than water, resulted in a decreasing length of the damage to 680 nm. The smallest damage was observed in air (550 nm) and the largest damage was observed for DI water with a viscosity of approximately 1 mPas.

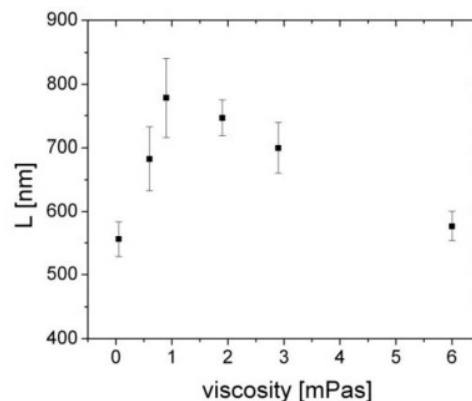


Figure 9. The lengths of the longest broken pieces (Fig. 5) vs. the viscosity of the media. Each data point consists of around 20 values (except at 2.9 and 6 mPas where 10 values were used).

#### Rupture Model

The experimental collapse force and the observed damage lengths do not correlate. The main influence on the damage size is the viscosity (Fig. 9) whereas it is negligible on the collapse force. A comparison of the collapse forces for DI water, S30, and S40 ( $0.9 < \nu < 6.0$  Pas) shows no significant variation (Fig. 4). However, the damage size distribution is significantly different, ranging from 780 nm in water to 580 nm in S40. Thus, two different mechanisms can be identified: One for the initial crack formation that determines the collapse force and the second one for the crack propagation determining the size of the damage. Apparently, the second one is mainly influenced by the bulk properties of the surrounding liquid.

The initial crack formation determines the collapse force because after the initial crack is established, stress concentration effects take place ensuring that the crack propagates through the whole structure. Usually, a crack initiates at a material defect or an interface in a high stress region. In this case it could be shown that the rupture line is located inside the polysilicon and

does not touch the polysilicon-SiON interface (23), i.e., the rupture occurs inside the polysilicon. Also the stress levels calculated by finite element analysis (3 GPa) corresponds to the reported fracture strength of polysilicon (23).

A stress corrosion crack (SCC) process lowers the absolute fracture strength. Such a process has been observed for polysilicon (24) and single-crystal silicon (25) in DI water. However, also the opposite was reported for the latter (26). Michalske et al. (27) suggested a model for a SCC process for silicon oxide. This process is applicable for DI water and to lesser extent for IPA, thus explaining the difference in collapse forces between these two liquids. An SCC process is a very slow process and crack tip velocities between  $10^{-6} - 10^{-7}$  m/s are expected (27) being much smaller compared to the Rayleigh wave propagation speed in silicon (2 - 3 km/s (28)) at which cracks usually propagate. Taking into account that the whole rupture process occurs within less than 2 ms allows only SCC assisted rupture lengths of several nm. Thus, SCC can only be applicable for a small part of the rupture line which is 40 nm perpendicular to the line and larger than 300 nm along to the line. This is another indication of a two step breaking behavior where SCC is dominating the crack initiation process, and the bulk physical properties of the media determine the damage formation and not the force / energy required to break the line. The significant difference to the previously reported results is that due to the small size of the structures, the stress corrosion process influences the fracture strength of polysilicon already for single load tests.

### Conclusion

We investigated the fracture of polysilicon nanostructures with a SiO<sub>2</sub> cap layer caused by lateral forces in various liquid media. The maximum fracture strength was observed for isopropanol which is 1.4 times higher compared to air or de-ionized water.

The shape of the damage was always round which indicates a conchoidal fracture or clamp-shell-like fracture. Characteristic differences occurred in the lengths of the generated damage depending mainly on the bulk properties of the liquid media. The fracture force and the damage size do not correlate with each other. A two step breaking model is proposed where the fracture force is determined by the crack initiation and the damage size in the second step by the bulk of the surrounding liquid. A stress corrosion crack process can be safely excluded from the second part due to the time scale of the rupture. For the crack initiation a stress corrosion crack process on the surface can explain the influence of the surrounding media. With further reduction of the line width in future structures a higher influence of the media on the mechanical stability is expected.

### References

1. [http://www.solid-state.com/display\\_article/250829/5/none/none/Feat/Using-mixed-fluid-jet-bombardment-for-advanced-particle-remova](http://www.solid-state.com/display_article/250829/5/none/none/Feat/Using-mixed-fluid-jet-bombardment-for-advanced-particle-remova), Oct 22<sup>nd</sup>, 2008
2. W. Kern and D. A. Puotinen, RCA Rev., **31**, 187, 1970
3. ITRS, Front End Processes, 3, 2007
4. H. Cao, P. Nealey and W. Domke, J. Vac. Sci. Technol. B, **18** (6), 3303 (2000)
5. D. Peter, M. Dalmer, H. Kruwinus, A. Lechner, L. Archer, E. Gaulhofer and W. Bensch, ECS Transaction, **13** (2) 323 (2008)
6. T. Kim, K. Wostyn, P. Mertens, A. Busnainan and J. Park, ECS Transactions, **11** (2), 123 (2007)
7. A. Kawai and Y. Kaneko, Jpn. J. Appl. Phys. **39**, 1426 (2000)
8. S. Kim, M. Jung, H. Kim, S. Woo and H. Lee, Nanotechnology **16**, 2227 (2005)
9. C. Green, H. Lioe, J. Cleveleand, R. Proksch, P. Mulvaney and J. Sader, Rev. Sci. Instrum., **75** (6), 1988 (2004)
10. C. Gibson, G. Watson and S. Myhra, Scanning, **19**, 564 (1997)
11. E. Liu, B. Blanpain, and J. P. Celis, Wear **192**, 141 (1996)
12. P. Cumpson, J. Hedley and C. Clifford, Vac. Sci. Technol. B **23** (5), 1992 (2005)
13. R. Cannara, M. Eglin and M. Carpick, Rev. Sci. Instrum. **77**, 053701 (2006)
14. D. Ogletree, R. Carpick and M. Salmeron, Rev. Sci. Instrum. **67** (9), 3298 (1996)

15. M. Varenberg, I. Etsion, and G. Halperin, *Rev. Sci. Instrum* **74** (7), 3362 (2003)
16. D. Asay and S. Kim, *Rev. Sci. Instrum.* **77**, 043903 (2006)
17. D. Asay, E. Hsiao and S. Kim, *Rev. Sci. Instrum.* **80**, 066101 (2009)
18. B. Baumeister, T Jung and E Meyer, *Applied Physics Letters*,**78** (17), 2485 (2001)
19. I. Zobel and M. Kramkowska, *Sensors and Actuators A*, **93**, 138 (2001)
20. I. Zobel, *Sensors and Actuators A*, **94**, 76 (2001)
21. D. Lide, *CRC Handbook of Chemistry and Physics*, 6-241 – 6-245, CRC Press, London
22. M. Migliori, D. Gabriele, R. Sanzo, B. Cindio and S. Corraera, *J. Chem. Eng. Data*, **52**, 1347 (2007)
23. D. Peter, F. Holsteyns, M. Dalmer, H. Kruwinus, A. Lechner, and W. Bensch, *ECS Trans.*, **25** (5), 241 (2009)
24. H. Kahn, R. Ballarini, J. Bellante and A. Heuer, *Science*, **298**, 1215 (2002)
25. K. Komai, K. Minoshima, and S. Inoue, *Microsystem Technologies*, **5**, 30 (1998)
26. B. Wong and R. Holbrook, *J. Electrochem. Soc. Solid-State Sci*, **134** (9), 2254 (1987)
27. T. Michalske and S. Freiman, *J. Am. Ceram. Soc.*, **66** (4), 284 (1983) 23
28. J. Hauch, D. Holland, M. Marder and H. Swinney, *Phys. Rev. Le.*, 82 (19), 3823 (1999)

## 4.5 Influence of Alcohols and the Solid-Liquid Interface

Based on the previous observation (section 4.3 and 4.4) that isopropanol has a significant beneficial influence on the fracture strength of polysilicon, further experiments were carried out in order to study this effect in more detail. The experimental conditions are identical with those presented in section 4.3.

The previously reported increase of the fracture strength by approximately 50 % in isopropanol compared to de-ionized water was confirmed by measurements in ethanol and 1-butanol. Taking into account the differences of the dielectric properties of the alcohols, indicated that there is no interface adhesion failure.

A significant difference between the alcohols and de-ionized water is the surface tension of 72 mN/m and around 20 mN/m, respectively. According to Griffith criterion for fracture [121], the interfacial energy term between the liquid and the solid can influence the fracture strength. Two surfactants (cationic and zwitter ionic) were used close to their respective critical micelle concentration (CMC) for the verification of this assumption. Both have a similar surface tension of around 35 mN/m. The zwitter ionic surfactant is cocoamidopropyl betaine ((CAPB), IUPAC: {[3-(dodecanoilamino)propyl] (dimethyl)ammonio}acetate) and the cationic surfactant is cetyltrimethyl ammoniumbromide (CTAB). The former enhanced the collapse force by only 10 % whereas with the latter caused an increase of more than 100 %. These results highly suggest that the surface tension of the liquid is not the only factor influencing the fracture force.

Both surfactants are accumulated at the surface of the solid. However, because the silicon oxide surface is negatively charged when immersed in de-ionized water, the CTAB molecules may form layers on the oxide surface. On the other hand, the negative charge of the CAPB molecules cause a repulsive force between the single molecules, and no dense layers can be formed on the silicon oxide surface. Hence, only the CTAB molecules protect the silicon oxide from the water molecules. The same effect is achieved by the deposition of a self assembled monolayer (SAM) which also increases the fracture strength to levels of the CTAB molecules.

Finally, a stress corrosion process which lowers the fracture strength of silicon is discussed. A qualitative explanation of the experimental results is given by assuming that such a process occurs only on the surface for the crack initiation.

Submitted to the proceedings of the UCPSS conference 2010. Publication will be in: Solid Stat Phenomena. Reproduced with permission of Trans Tech Publication Ltd.

## The influence of liquid media on the fracture strength of polysilicon nanostructures

Daniel Peter<sup>1,a</sup>, Michael Dalmer<sup>1,b</sup>, Alfred Lechner<sup>2,c</sup>, Alexander M. Gigler<sup>3,d</sup>, Robert W. Stark<sup>4,e</sup> and Wolfgang Bensch<sup>5,f</sup>

<sup>1</sup> Lam Research AG, SEZ-Str. 1, 9500 Villach, Austria

<sup>2</sup> University of Applied Sciences Regensburg, Seybothstr. 2, 93049 Regensburg, Germany

<sup>3</sup> Center for NanoScience (CeNS) and Ludwig-Maximilians-Universität München, Theresienstr. 41, 80333 München, Germany

<sup>4</sup> TU Darmstadt, Center of Smart Interfaces, Petersenstr. 32, 64287 Darmstadt, Germany

<sup>5</sup> Christian-Albrechts-Universität zu Kiel, Olshausenstr. 40, 24098 Kiel, Germany

<sup>a</sup>daniel.peter@lamresearch.com, <sup>b</sup>michael.dalmer@lamresearch.com,

<sup>c</sup>alfred.lechner@mikro.fh-regensburg.de, <sup>d</sup>gigler@lmu.de, <sup>e</sup>stark@csi.tu-darmstadt.de, <sup>f</sup>wbensch@ac.uni-kiel.de

**Keywords:** pattern collapse, fracture strength, damage, atomic force microscopy.

**Abstract.** The mechanical stability of nanostructures depends on the surrounding medium. Their stability was probed by lateral force microscopy in liquid media. Previously reported data on water and isopropanol showed an increase in the fracture strength for the latter. Further tests with other alcohols (ethanol, 1-butanol) also showed an increasing strength. The interface between the liquid and the surface is the decisive factor for the influence of the media. When altering the interface with a cationic surfactant or a self-assembled monolayer, an increase of the fracture force by 100 % compared to de-ionized water could be measured.

### Introduction

High aspect ratio structures in the semiconductor industry are prone to pattern collapse in cleaning and in release etching processes. Common structures include shallow trench insulators, capacitors over bitline, and gate structures. Pattern collapse during drying is usually attributed to surface tension forces, which are increasing with the spatial density of the structures. The combination of shrinking geometries and, in turn, decreasing mechanical strength, together with rising aspect ratios in future technology nodes will make surface tension forces even more dominant. Other forces can also contribute to damage generation during a cleaning process. This is particularly important for a physical-force-assisted cleaning process, such as megasonics or aerosol processes [1] which need to be carefully designed to avoid damage.

For the development of future cleaning processes, it is essential to understand the reason for generation of the respective damage to meet the damage-free requirement. In this work, the atomic force microscope (AFM) has been used to measure the mechanical stability of line structures. Mechanical stability measurements have been reported initially on photoresist structures [2] and more recently on polysilicon line structures [3, 4]. Mechanical analyses including finite element simulations also showed good agreement with the experimental data [5, 6]. A cleaning window was defined by comparing the forces for removing a particle and the mechanical stability of various structures [7]. Recently, the influence of the surrounding media on the mechanical stability of polysilicon line structures was shown [8]. A significant increase of the mechanical stability of these structures was observed in isopropanol as compared to air as medium. De-ionized water (DIW) showed similar results as air. Here we discuss the influence of alcohols, surfactants, and self-assembled monolayers (SAMs) on the mechanical stability of polysilicon nanostructures and compare these results to previous tests in DIW and air.



## Experiment

AFM was used in lateral force mode to apply and measure mechanical forces in order to generate damage in a defined way (Figure 1). The respective yield force was measured from the lateral force signal (Figure 2b). Calibration of the AFM as described in detail in [4] was conducted for each of the tips. The tips were used only in one specific medium (Figure 2c). A successful pattern collapse can be observed as a significant difference between the trace and retrace curves (Figure 2d).

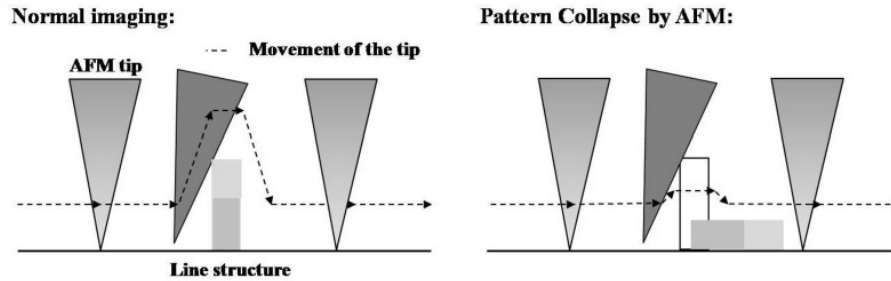


Figure 1: Principle of pattern collapse by AFM.

The structures under investigation were line structures with a nominal line width of 40 nm. In the z-direction, the lines consisted of a stack of a silicon oxide hardmask layer (50 nm) with 100 nm polysilicon on a 2.4 nm silicon oxy-nitride layer (Figure 2a).

Immersion media included alcohols (ethanol and 1-butanol) and solutions of surfactants with DIW (cocamidopropyl betaine (CAPB) and cetyl trimethylammonium bromide (CTAB)) close to their respective critical micelle concentrations. The surface modification of the nanostructure was also tested. To render the surface hydrophobic, a self-assembled monolayer of fluorooctatrchlorosilane (FOTS) was created on the surface. The modified structure was subsequently tested in DIW.

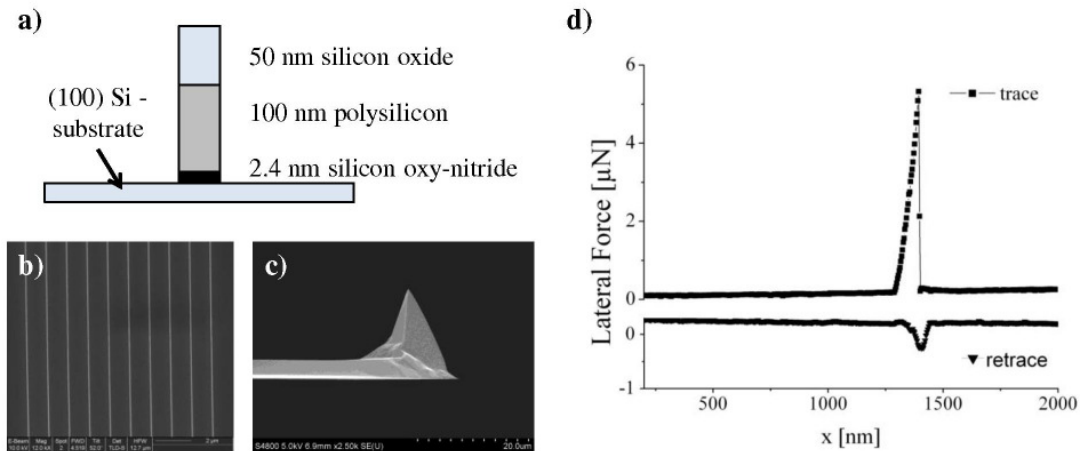


Figure 2: a) Schematic of the cross-section and b) top-down SEM micrograph of the line structures; c) SEM image of a typical AFM tip; d) lateral force signal recorded during a collapse procedure.

## Results and Discussion

Testing of polysilicon line structures in alcohols revealed consistent fracture forces of about 6  $\mu\text{N}$  and 4.2  $\mu\text{N}$  in DIW [8]. The average fracture forces were 6.2  $\mu\text{N}$  for ethanol, 5.9  $\mu\text{N}$  for isopropanol, and 6.3  $\mu\text{N}$  for 1-butanol. Furthermore, the distributions of the measured collapse forces did not show differences between the alcohols and DIW. SEM micrographs indicate an overall range between 36 nm and 50 nm for the line width. In combination with finite element analysis [6] more than 90 % of the values can be explained by the line width variations.



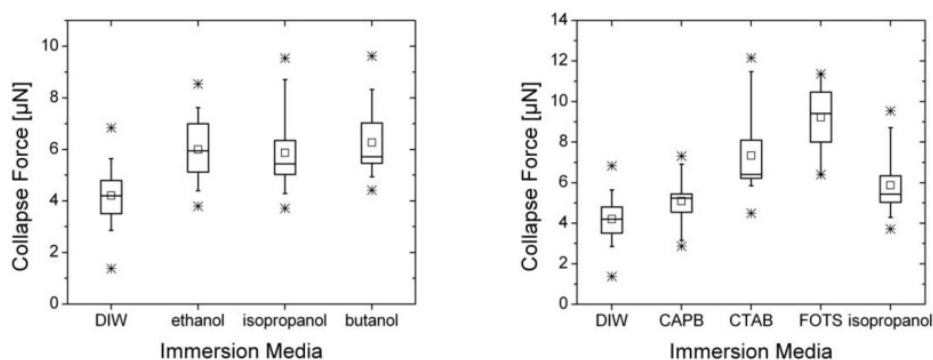


Figure 3: Box plot of lateral forces required for pattern collapse (a) in various alcohols and (b) for modified interfaces. Box starts from 25<sup>th</sup> to 75<sup>th</sup> percentile, tail from 10<sup>th</sup> to 90<sup>th</sup> percentile, and asterisks denote minimum and maximum values. Please note the different scale of the graphs.

The similar average collapse values from ethanol to 1-butanol (Figure 3a) indicate that the change in electric permittivity from 25 (ethanol) to 18 (butanol) does not affect the mechanical strength of the structures. Thus, an adhesion failure of the polysilicon on the silicon oxy-nitride is unlikely as it would be expected to depend on the dielectric property of the media. This is in accordance to the observed damage (Figure 4) which shows a conchoidal fracture (i.e. half moon shaped) in all media and no delamination at the material interface. TEM analysis confirmed that the structures break inside the polysilicon layer [6]. Only the size of the damage (marked L in Figure 4) was influenced by the immersion media. In fact, the fracture force is independent of the damage size, which is mainly due to the viscosity of the media [8].

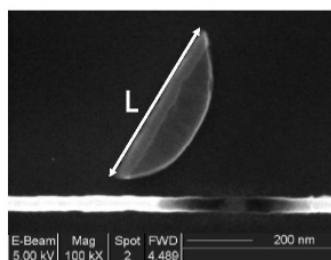


Figure 4: SEM micrograph of typical damage generated by the AFM pattern collapse method.

Griffins criterion for fracture includes an interfacial energy term for the determination of the fracture force. The significant difference between the results of DIW (72 mN/m) and the tested alcohols (20 – 25 mN/m) are in accordance with this theory. Another way of influencing the surface tension is the use of surfactants (CTAB and CAPB) in DIW, which lowers the surface tension to 35 mN/m. CTAB causes a high average collapse force (7.3 µN), whereas CAPB only increases the critical force from DIW by 4.2 to 5.1 µN. (Figure 3b). Hence, the influence of surface tension is negligible on the fracture force of the structures.

The difference between the two surfactants is that CTAB is a cationic surfactant and CAPB is a surfactant with a zwitter ion. As the silicon oxide surface in DIW is negatively charged at pH = 6, the cationic CTAB can form a bilayer on the surface [9]. On the other hand, CAPB can not form such a dense layer because of its additional positive charge which prevents a densely ordered packing. For the water molecules, CTAB is expected to act like a protective layer for the silicon oxide surface. A similar effect can be obtained by the deposition of a self-assembled monolayer like FOTS. The successful deposition was verified by the measurement of the contact angle. Further testing of the modified structure revealed the highest average collapse forces measured yet for these structures at 9.2 µN.

Water is known to cause a stress corrosion process on silicon oxide that lowers the overall fracture force. Nevertheless, this process is very slow and for the time scale of the fracture as observed by AFM

(< 2 ms), yields only a fissure length (few nanometers), far smaller than the width of the line structure. Thus, it cannot be responsible for the whole fracture process, though it is possible that the seed crack is generated with the help of corrosion. As the initial crack lowers the overall stability considerably by providing a stress concentration point, it directly affects the mechanical stability of the line structures. The relative collapse forces between the surface coatings, alcohols, and DIW are in qualitative agreement to the crack velocities at any fixed stress values reported by Michalske et al. [11]. Thus, the influence of the immersion media on the mechanical strength of polysilicon nano-structures indicates a stress corrosion process for the generation of the seed crack.

### Conclusion

Protecting a polysilicon nanostructure from corrosive chemistries such as DIW increases the mechanical stability of line structures. In alcohols, an increase of 50 % of the fracture force with respect to DIW was observed. An influence of surface tension could be excluded by the test of two surfactants with similar surface tension which resulted in dissimilar collapse forces. The formation of layers on the surface by cationic surfactant or self-assembled monolayer increased the fracture force by 100 % compared to DIW. The enhanced mechanical stability in absence of DIW could be utilized in advanced cleaning processes in order to prevent damage. Future research should extend to non-polar solvents where similar collapse force values as for CTAB are expected.

### References

- [1] C. De Marco, K. Wostyn, T. Bearda, K.-I. Sano, K. Kenis, T. Janssens, L. Leunissen, A. Eitoku, and P. Mertens, *ECS Trans.*, **11** (2), 2007, p 87
- [2] A. Kawai and Y. Kaneko, *Jpn. J. Appl. Phys.* **39**, 2000, p 1426
- [3] T. Kim, K. Wostyn, P. Mertens, A. Busnainan, and J. Park, *ECS Trans.*, **11** (2), 2007, p 123
- [4] D. Peter, M. Dalmer, H. Kruwinus, A. Lechner, L. Archer, E. Gaulhofer, and W. Bensch, *ECS Trans.*, **13** (2), 2008, p 323
- [5] K. Wostyn, T.G. Kim, P. W. Mertens, and J.G. Park, *Solid State Phenomena*, **145-146**, 2009, p 55
- [6] D. Peter, F. Holsteyns, M. Dalmer, H. Kruwinus, A. Lechner, and W. Bensch, *ECS Trans.*, **25** (5), 2009, p 248
- [7] T.G. Kim, K. Wostyn, T. Bearda, J.G. Park, P. Mertens, and M. Heyns, *ECS Trans.*, **25** (5), 2009, p 203
- [8] D. Peter, M. Dalmer, H. Kruwinus, A. Lechner, L. Archer, E. Gaulhofer, A. M. Gigler, R. W. Stark, and W. Bensch, *ECS Trans.*, **16** (40), 2008, p 13
- [9] Z. Bi, W. Liao, and L. Qi, *Applied Surface Science*, **221**, 2004, p 25
- [10] J. Han, J. M. Yang, S. C. Shin, Y. Kim, and S. Kang, *IEEE Transactions on Magnetics*, **45** (5), 2009, p 2288
- [11] T. A. Michalske and B. C. Bunker, *J. Appl. Phys.*, **56** (10), 1984, p 2686

## 4.6 Solid Bridging Studied with Silicon Nanoparticles

With the increasing aspect ratios of device structures, the likelihood of pattern collapse with bending of the structures increases. In that case, a “sticking” force is required after the complete removal of the liquid in order to compensate the elastic restoring momentum. In addition to van der Waals forces and hydrogen bonding interactions, solid bridging has been discussed for MEMS structures. In structures showing the solid bridging phenomenon, silicates are thought to be accumulated and deposited between the structures. Silicon nanoparticles with a nominal size of 50 nm were chosen to study this phenomenon in detail because of their comparable length scale to STI structures and their high surface-to-volume ratio.

Stable dispersions of the nanoparticles with de-ionized water were generated. Subsequently, the liquid was removed from the particles by freeze drying and evaporation drying. Analysis of the dispersion showed the presence of silicates and large particle agglomerations (with sizes up to 500 nm).

Analyses of the dried powders confirmed that the particles consisted of a core-shell system, where the core is composed of crystalline silicon and the shell of silicon dioxide. The average thickness of the shell was not influenced by the exposure time to de-ionized water. Thus, no significant oxide growth could be observed except for particles exposed to air for several months. The average size of the particles was determined by XRD and confirmed by TEM measurements. The XRD data indicated a size of about 60 nm, which slightly increased to 65 (64) nm after evaporation (freeze) drying. The growth of the particles may be explained by dissolution of the smaller particles forming silicates and the subsequent deposition of the material between the larger particles. These solid bridges were visualized using HRTEM. In the micrographs of the original particle, only some small bridges could be observed. An increase in bridging was found for the particles obtained after freeze drying and the most pronounced solid bridging phenomenon was seen for the particles that were subject to the evaporation drying process.

These results clearly indicate the drying process of semiconductor nanostructures is an important issue, and solid bridging has to be taken into account. In further studies methods should be explored to prevent the formation of silicates or their re-deposition between the structures in order to decrease pattern collapse phenomena.

D. Peter, M. Dalmer, A. Lotnyk, L. Kienle, A. Lechner, and W. Bensch, "Solid Bridging during Pattern Collapse (Stiction) Studied on Silicon Nanoparticles", in *Microelectromechanical Systems – Material and Devices IV*, edited by F. W. DelRio, M. P. de Boer, C. Eberl, and E. P. Gusev, (*Mater. Res. Soc. Symp. Proc.*, Vol. 1299, Warrendale, PA, 2011), 9.29, submitted, Material Research Society ©

### **Solid bridging during pattern collapse studied on silicon nanoparticles**

Daniel Peter<sup>1</sup>, Michael Dalmer<sup>1</sup>, Andriy Lotnyk<sup>2</sup>, Lorenz Kienle<sup>2</sup>, Alfred Lechner<sup>3</sup>, and Wolfgang Bensch<sup>4</sup>

<sup>1</sup> Lam Research Corporation, SEZ Str. 1, 9500 Villach, Austria

<sup>2</sup> Institute for Material Science, Technical Faculty, Christian-Albrechts-Universität Kiel, Kaiserstraße 2, 24143 Kiel, Germany

<sup>3</sup> Microsystems Engineering, University of Applied Sciences Regensburg, Seybothstr. 2, 93049 Regensburg, Germany

<sup>4</sup> Inorganic Chemistry, Christian-Albrechts-Universität Kiel, Max-Eyth-Str. 2, 24118 Kiel, Germany

#### **ABSTRACT**

The high surface to volume ratio of nanoparticles allows a detailed experimental study of the surface phenomena associated with solid bridging. Besides bulk analyses, the local view on the structure and composition via HRTEM is particularly essential. 50 nm core shell particles consisting of a silicon (Si) core and a SiO<sub>2</sub> shell were used as model system to understand surface phenomena appearing for Si-based nanostructures. Evaporative drying from de-ionized water shows the most significant bridging effect based on SiO<sub>2</sub>. There is only a localized deposition of oxides between the particles during the drying process and no overall oxidation. For the deposition material, silicates are the most likely candidates.

#### **INTRODUCTION**

The surface preparation of semiconductor wafers is an important part of the production process. One essential requirement for wet surface preparation (i.e., etching and cleaning) is to avoid any damage of the structured wafer surface. The most vulnerable patterns are high aspect ratio structures, which are typically capacitor over bitline, shallow trench insulator (STI), or future FinFET structures. The largest mechanical forces in a wet clean process are generally attributed to physical force assisted cleaning steps (e.g., megasonics, spray systems) [1] and the surface tension forces in the drying step [2].

The distinctive damage from surface tension forces is the connection of the former free ends of the structures after drying. The fixed end can either be ruptured or elastically bent (Figure 1). The latter case is important for micro-electromechanical systems (MEMS) [3], which differ from microelectronic structures mainly by the higher aspect ratios and the larger size of micrometers vs. nanometers.

For a permanent damage, a sufficiently large sticking force [3] has to keep the structures in place against the restoring elastic moment after the liquid, and therefore the surface tension force, is removed. On MEMS devices, the main adhesive force for hydrophilic surfaces is hydrogen bonding, and for hydrophobic surfaces, van der Waals forces (vdW) [4]. Additionally, after the collapse, residues (e.g., silica) can accumulate around the contact site and form a solid bond which is called solid bridging [4-7]. Corresponding adhesive energies are expected to be larger than hydrogen bonding and vdW forces; however, the determination of the characteristic

energies is complicated by the inhomogeneous deposition of the silica residues. The aspect ratios of microelectronic structures, such as STI, approach the aspect ratios of MEMS devices, and therefore elastic deformation is becoming more likely. Additionally, nano-scale effects can enhance the solid bridging effect by increasing the reactivity of the surface.

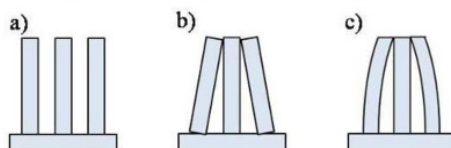


**Figure 1.** Pattern collapse of line structures: a) no collapse, b) rupture, c) bending.

## EXPERIMENTAL DETAILS

The solid bridging phenomenon was studied with Si nanoparticles in de-ionized water which were subsequently removed from the liquid by drying. Analyses were performed in the dispersion as well as with the dry powder.

The nanoparticles with a nominal diameter of 50 nm purchased from Nanostructured & Amorphous Materials Inc. were used in all the experiments in order to have a comparable length scale to STI structures and therefore similar nano-scale effects. Stable dispersions were created with de-ionized water (18.2 M $\Omega$ ) in polyethylene flasks using 10 min of ultrasonic sound (Allpax Palsson). The concentration of the Si particles was adjusted to the dispersion limit (0.3 g/L) where no sedimentation occurs.

Two drying techniques were employed: first, evaporation drying with air flow at elevated temperature and second, freeze-drying using liquid nitrogen. The latter was used in order to prevent oxidation during the drying step. Additionally, particles were aged in air for several months. A summary of the tested conditions is presented in Table I.

**Table I.** Experimental conditions of the characterized nanoparticles.

Name	Aging condition	Drying
A (reference)	none	none
B	air	none
C	dispersion (DIW)	freeze-drying
D	dispersion (DIW)	evaporation drying

The sizes of the dispersed particles were determined by light scattering techniques, and the presence of silicates was examined with electro-spray ionization mass spectroscopy (ESI-MS).

The sizes and overall compositions of the particles were characterized by X-ray powder diffraction (XRD) with the Debye-Scherrer equation (using Cu-K $\alpha_1$  and K $\alpha_2$ ) [8] and transmission electron microscopy (TEM) (Tecnai F30 G<sup>2</sup> ST), respectively. In order to increase the accuracy of the XRD experiments, an internal standard of aluminum oxide ( $\alpha$ -phase) was used. The intensity data were quantified via Rietveld refinement (FullProf [9]). For the study of the surface of the particles, X-ray photo electron spectroscopy (XPS) was applied, and solid state <sup>29</sup>Si NMR with magic angle spinning (MAS) was employed for the determination of the chemical composition of the silicon oxide. The local accumulation of SiO<sub>2</sub> was visualized by energy-filtered TEM (EFTEM) and high-resolution TEM (HRTEM).

## RESULTS & DISCUSSION

### Dispersion

The dispersions of the Si nanoparticles were stable in de-ionized water for more than 6 months without showing sedimentation. Light scattering measurements showed a zeta potential of about -30 mV; thus electrostatic interaction between the particles probably stabilizes the dispersion. The broad distribution of particle sizes as determined by the optical methods indicated a large increase of the average value of ~500 nm compared to the original sizes of ~50 nm. Sizes larger than 200 nm are due to agglomerates of the original particles as evidenced by TEM analyses. Nevertheless, as the optical methods are more sensitive to the larger particles/agglomerates, these methods could not be used for tracing the change of the small particles.

ESI-MS has been used to study the formation of silicates in water [10, 11] without disrupting the Si–O bonds. In the dispersion liquid, silicates could also be measured and a trend of condensation was observed from the initially formed mono-silicates.

### Silicon Oxide

The chemical composition of the nanoparticles was determined by XPS (Figure 2) with the excitation energy of 1487 eV and  $^{29}\text{Si}$  MAS-NMR (Figure 3). A shift of the energies by 7 eV was observed in the XPS spectra (using O 1s signal) and attributed to sample charging. The characteristic energies of Si 2p for  $\text{Si}^0$  ( $\text{Si}^{4+}$ ) were shifted to 106.5 eV (111 eV). For the calculation of the oxide thickness [12], the intensities of the Si 2p peaks were fitted by two Gaussian peaks. Only negligible signal intensity for  $\text{Si}^0$  could be found for particles B, which corresponds to an oxide thickness in excess of 10 nm. All other particles, including the reference particles, showed an oxide thickness of ~5 nm. Hence no net oxide growth could be observed for the particles treated with de-ionized water. The calculated curve for particles A (Figure 2) using the two Gaussian functions closely follows the experimental values except for a small part in between the peaks (box in Figure 2).

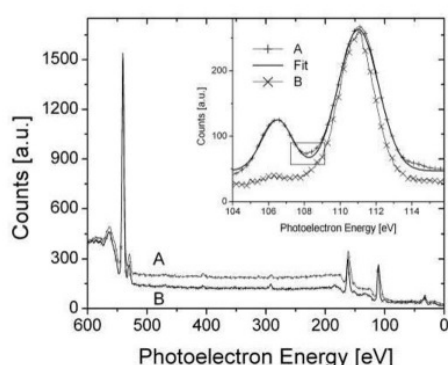


**Figure 2.** XPS spectra of Si of particles A and B with the typical energy range of the Si 2p region amplified in the inset.

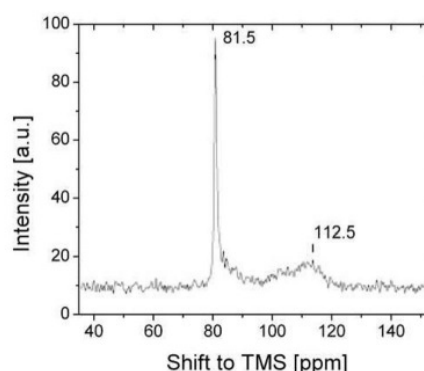


**Figure 3.** Particles A measured with  $^{29}\text{Si}$  MAS-NMR.



This difference indicates the presence of a negligible amount of suboxides. In addition, NMR data did not show significant contribution from suboxides. The broad peak between 108 to 114 ppm (Figure 3) is assigned to  $\text{SiO}_2$  showing some variation of the Si-O-Si angles of neighboring  $\text{SiO}_4$  tetrahedra [13]. Thus, the oxide present on the particles is identified as  $\text{SiO}_2$ . The core of the particles consisted of crystalline Si due to the peak at 81 ppm [14] in the NMR data, which was also confirmed by TEM measurements (Figure 8).

### Size and Structure Analysis

X-ray powder diffraction and TEM micrographs were used supplementarily for the measurement of the sizes and the characterization of the microstructures. The former established data of the average size over a large ensemble of particles and the latter localized measurements of individual particles. The XRD data (Figure 4) were evaluated with Rietveld refinement because of the small differences in the reflection profiles and hence particle sizes (Figure 5).

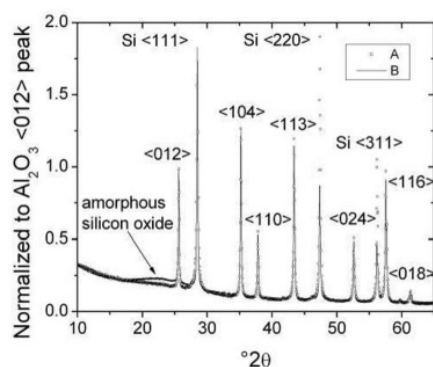


**Figure 4.** XRD pattern of the Si nanoparticles with  $\text{Al}_2\text{O}_3$  ( $\alpha$ -phase) as standard.

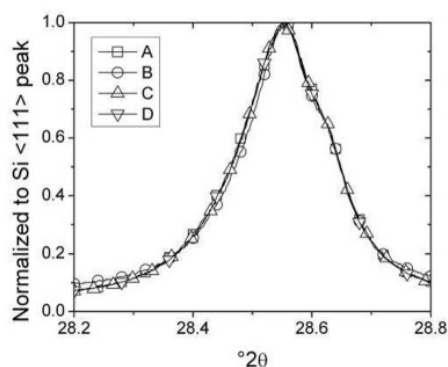


**Figure 5.** (111) reflection of Si measured by XRD for the various particle conditions. Only every 20<sup>th</sup> point is marked for better visibility.

Significant amorphous  $\text{SiO}_2$  was found only on the particles B with XRD (Figure 4), which is consistent with the XPS observations on these particles. Due to the long time scale of several months, the oxidation in air appears more significant than the oxidation in de-ionized water. Nevertheless, the particles B provided the proof that the other particles (A, C, D) are not at their native oxide limit, as well as that the XRD measurement is sensitive enough to show significant amorphous oxide growth.

According to the XRD data, the average sizes of the particles were found to increase by 4 nm for particles C and 5 nm for particles D. However, the size difference can not be due to the growth of  $\text{SiO}_2$  on the surface of the particles, as indicated by the XPS data.

**Table II.** Sizes of the particles calculated from XRD data applying the Scherrer equation.

Particles	A	C	D
Size [nm]	60	64	65

The average sizes of the particles estimated from XRD data were confirmed by TEM bright field micrographs, which showed mostly spherical particles, generally in the range between 20 nm to 100 nm (Figure 6). The particles exhibit a core-shell microstructure. SiO<sub>2</sub> forms the shell as highlighted by the bright intensity at the particle edges in the EFTEM image of Figure 7. The Si in the core is crystalline (cf. lattice fringes in the HRTEM micrograph of Figure 8), which is consistent with the NMR data.

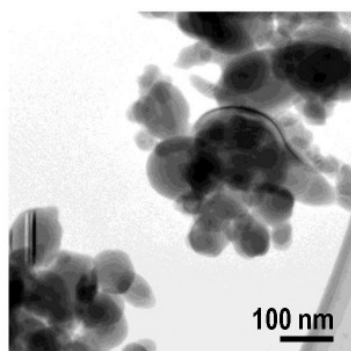


**Figure 6.** TEM micrograph of agglomerates of particles on the sample grid.

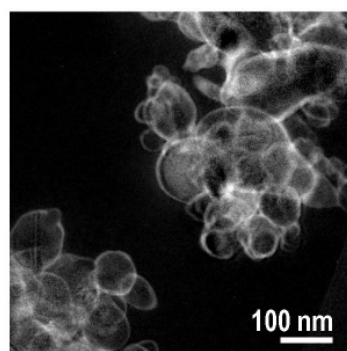


**Figure 7** EFTEM image of oxygen distribution in the Si particles.

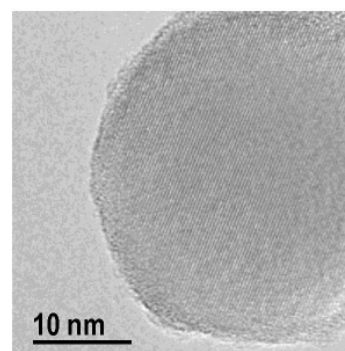


**Figure 8.** HRTEM showing the crystalline nature of the core Si particles.

### Local Oxide Growth

The dependence of the sizes of the particles and the aging conditions suggests dissolution of the smallest particles and of the asperities into silicates, with the subsequent deposition as SiO<sub>2</sub> onto the larger particles. As there was no homogenous oxide growth on the surface of the particles, only a localized oxide growth was possible. This was confirmed by TEM measurements on the edge of the particle agglomerates (Figure 9-11), which showed SiO<sub>2</sub> accumulation between the particles, i.e., solid bridging. The size and the number of the solid bridges increase depending on the aging conditions. For the particles A, solid bridges were found rarely and with small sizes (<5 nm), whereas for particles D, their amount was large and in the 10 nm size range.

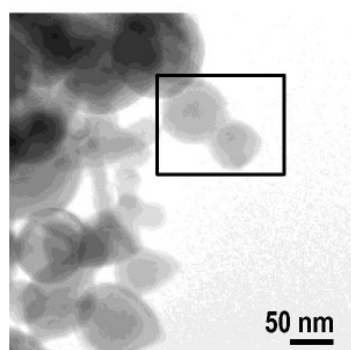


**Figure 9.** TEM bright field of particles D with solid bridging.

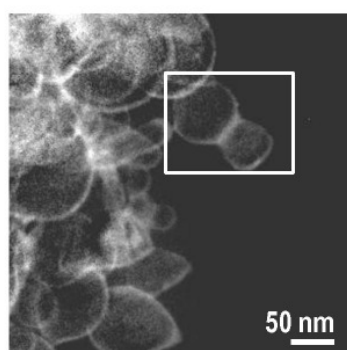


**Figure 10.** EFTEM image of oxygen distribution in the Si particles shown in Figure 9.

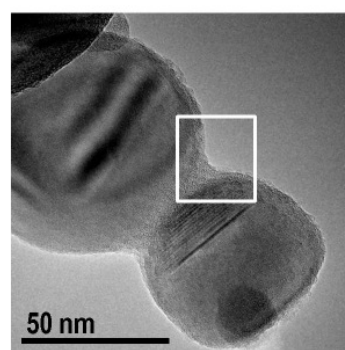


**Figure 11.** HRTEM of area A in Figures 9 and 10 with a solid bridge.



As the location of the preferential deposition is between the particles, the XPS as a surface-sensitive technique cannot detect the additional SiO<sub>2</sub>, which explains the similar oxide thicknesses for the aged particles. However, the overall increase of amorphous oxide is very limited because no significant amorphous oxide was observed in the XRD patterns. Significant solid bridging was found for particles D, with limited bridges for particles C. Thus, the dominant step for solid bridging is the drying step. Freeze drying prevents an accumulation of SiO<sub>2</sub> between the particles probably because the ice can not transport the (silicate) solute to the area between the particles.

## CONCLUSIONS

Solid bridging between Si nanoparticles was found especially after evaporative drying processes as determined by TEM examinations. The bridging material was SiO<sub>2</sub> that was deposited during the drying process, most likely from silicates. For a semiconductor drying process where pattern collapse of nano-scale structures occurs, solid bridging has to be expected.

## ACKNOWLEDGMENTS

The author would like to thank Dirk Meyer for the ESI-MS measurements. For the XPS measurements, the authors owe special thanks to Dr. V. Zaporozhchenko. The NMR data are courtesy of Prof. J. Senker (University of Bayreuth).

## REFERENCES

1. C. De Marco, K. Wostyn, T. Bearda, K.-I. Sano, K. Kenis, T. Janssens, L. H. A. Leunissen, A. Eitoku, and P.W. Mertens, *ECS Transactions*, **11** (2) 87 (2007).
2. H. Cao, P. Nealey, and W. Domke, *J. Vac. Sci. Technol. B*, **18** (6), 3303 (2000).
3. C. H. Mastrangelo, *J. Microelectromech. S.*, **2** (1), 33 (1993).
4. K. Komvopoulos, *Wear*, **200**, 305 (1996).
5. R. L. Alley, G. J. Cuan, R. T. Howe, and K. Komvopoulos, *Solid-State Sensor and Actuator Workshop, 5<sup>th</sup> Technical Digest.*, (IEEE, Hilton Head Island, SC, 1992) pp. 202-207.
6. R. Maboudian and R. T. Howe, *J. Vac. Sci. Technol. B*, **15** (1), 1 (1997).
7. R. Legtenberg, H. A. C. Tilmans, J. Elders, and M. Elwenspoek, *Sensors and Actuators A*, **43**, 230 (1994).
8. A. L. Patterson, *Physical Review*, **56**, 978 (1939).
9. J. Rodriguez-Carvajal, Fullprof.2k, Version 4.6c – Mar 2002, *Physica B*, **55**, 192 (1993).
10. S. A. Pelster, R. Kalamajka, W. Schrader, and F. Schüth, *Angew. Chem.*, **119**, 2349 (2007).
11. B. B. Schaack, W. Schrader, and Ferdi Schüth, *Angew. Chem.*, **120**, 9232 (2008).
12. F. J. Himpsel, F. R. McFeely, A. Taleb-Ibrahimi, J. A. Yarmoff, and G. Hollinger, *Physical Review B*, **38** (9), 6084 (1988).
13. E. Dupre and R. F. Pettifer, *Nature*, **308** (5), 523 (1984).
14. W.-L. Shao, J. Shinar, and B. C. Gerstein, *Phys. Rev. B*, **41** (3), 9491 (1990).

## V Conclusions and Outlook

During the production of semiconductor device structures, there is the damage phenomenon of pattern collapse. The tops of the structures (free ends) are connected together via bending or rupture. This is the distinctive damage shape associated with pattern collapse. The most important cause for this damage is attributed to surface tension forces. During wetting or de-wetting, when the structures are only partially immersed in the liquid, capillary pressure is assumed to pull the structures together. In the semiconductor industry, the question has been raised whether this model, originally developed for micron-sized structures, is still valid and sufficient to describe the phenomenon for structures on the nanometer scale. In addition to surface tension forces other forces like spin forces occurring during the drying processes have been suggested.

The large unknown property for the evaluation of the forces acting on the nanostructures was their mechanical stability. The atomic force microscope was used to apply lateral forces onto the nanoscale line structures until fracture of the lines occurred, in order to measure their mechanical stability. The forces were recorded by the combination of the lateral signal of the segmented photo diode and a calibration procedure using the direct force balance method. The tested lines were made of polysilicon with a silicon oxide hard-mask on top.

Collapse forces in the low  $\mu\text{N}$  range have been measured for these structures. The average forces were  $2\ \mu\text{N}$ ,  $4\ \mu\text{N}$ , and  $5.5\ \mu\text{N}$  for the 25 nm, 40 nm, and 50 nm structures, respectively. Finite element models of the structures confirmed the relationship between the line width and the collapse forces. A breaking strength of approximately 3 GPa yielded the best agreement between experiment and theory.

This strength is typical for polysilicon, which is between the yield stress of an interface and a failure in single-crystal silicon.

The mechanical stability of nanostructures is significant, and forces that take the mass of the body of the structure into account, like spin forces, can therefore be neglected. The hypothesis of significant residual stress reducing the mechanical stability is not applicable in this case. The protection of the material interfaces is feasible by including corner rounding at the bottom of the structure, which effectively increases the mechanical stability of the respective structure. In general, the cross-section of the structure should be properly designed in order to decrease the pattern collapse phenomena.

Because pattern collapse occurs while the structures are still partially immersed in the liquid, the influence of the liquid onto the mechanical stability of the nanostructures must be taken into account. De-ionized water only had a negligible influence on the collapse force, whereas isopropanol increased the value by about 50 %. Other alcohols, such as ethanol and 1-butanol, were also tested and yielded similar results. When a small amount of isopropanol was added to de-ionized water, the same effect as with the other alcohols was obtained, i.e., the collapse force increased. Because the mixture of isopropanol/water can be regarded as a type of surfactant, the isopropanol molecules cover mainly the silicon oxide surface and, thus, only the solid-liquid interface is influencing the mechanical stability. The comparable results of tests in de-ionized water and in air indicate the same behavior due to water covering the oxide surface in an ambient atmosphere. The solid-liquid interface was additionally chemically altered with a cationic surfactant and a self-assembled monolayer (SAM), both of which shields the silicon oxide, thus suppressing full coverage of the surface with water molecules. With the cationic surfactant respectively the SAM on the surface cases the collapse forces increased by roughly 100 %. All results are in qualitative agreement with a surface stress corrosion process discussed in the literature. When taking into account the time scale of the rupture, only the initial crack generation may benefit from such a corrosion process. Nevertheless, this initial crack is sufficient to provide a stress concentration point, therefore limiting the mechanical stability of the structure. The difference to the previously reported stress corrosion cracking is that the corrosive effect can be seen already at a single force event, instead of a wear-down scenario.

The damage obtained in the experiments showed a characteristic shape and size for the nanostructure test lines. The shape was round, which indicated a conchoidal fracture. Thus, the fracture did not follow any defects or separation planes like the grain boundaries within the polysilicon material. The negligible influence of the grain boundaries on the yield line could be visualized with TEM measurements, which also confirmed, that the rupture occurred inside the polysilicon line. The corner rounding at the bottom of the structure shifts the maximum stress away from the interfaces into the polysilicon material, which explains the fracture behavior of these structures.

The size of the damage is influenced by the viscosity of the surrounding media. The maximum size of the damage was observed for a viscosity of 0.9 mPas, which is the value for de-ionized water. For both larger and lower viscosities, an almost linear decrease to smaller damages down to 500 nm was found. An exact model relating viscosity and damage size remains to be developed. There was no indication for a relationship between the collapse force and the damage size.

For the “sticking” forces that prevent the structures from relaxing to their original state after the removal of the liquid, the solid bridging concept has been introduced for MEMS devices. Some publications suggest that silicon oxide is accumulated between the structures and bonds them via solid bridging. In order to verify this assumption for microelectronic nanostructures, silicon nanoparticles with a size of 50 nm were used. These particles have the advantage of a comparable length scale with STI structures and a high surface-to-volume ratio. The latter allowed the usage of NMR and XRD techniques which would otherwise not be sensitive enough for the surface phenomenon of solid bridging. A cleaning process was simulated by exposing the particles to de-ionized water with a subsequent drying procedure. The core-shell particles with a silicon dioxide surface did not experience significant oxide growth. The average size of the particles increased for both the freeze drying and the evaporative drying procedures, which indicated dissolution of smaller particles. Silicon oxide material was found between the particles as a solid bridge, probably through the formation of silicates that were deposited during the drying step. The largest solid bridges were found for the evaporation drying procedure with less significant bridging seen for the freeze drying technique. These results give clear hints that the most important step for the generation of solid bridging is the drying step.

For pattern collapse of sub-50 nm semiconductor structures, the prediction of the stability by continuum mechanics is still useful. An important and new result is that the surrounding media has a significant influence on the stability of nanoscale structures for non-cyclic loads, which has only been reported for cyclic loads in macro-scale structures. For the prevention of pattern collapse, bending and the subsequent solid bridging by silicates also have to be taken into account. All results obtained during the thesis suggest that surface tension alone is not sufficient for the explanation of the pattern collapse phenomena of the latest semiconductor nanostructures.

---

## List of Figures

Figure I.1 Simplified cross-section through early bipolar transistor geometries. Original drawings published by Riordan [1]. .....	4
Figure I.2 Historic review of Moore's Law (transistor count doubling every two years) with Intel® products and the corresponding technology sizes (node) [8].....	5
Figure I.3 SEM cross sections of DRAM cells a) during production before the deposition of the dielectrics (includes hemi-spherical grained silicon (HSG) electrode), and b) post production with fully formed capacitor and contacts. SEMs courtesy of [21] with permission from Elsevier®. ....	7
Figure I.4 Gate structure of a flash memory cell. ....	8
Figure I.5 Simplified 3D model of a flash memory cell. Note the isolation features around the floating gates (red) which are the STI in x-direction and the word line dielectric in y-direction. Model courtesy of D. Preiml (Lam Research AG) using the model of J. Postel-Pellerin et al. [28] as a guideline. ....	8
Figure I.6 Definition of the aspect ratio for line structures (a) and cylinders (b).....	9
Figure I.7 Cylindrical DRAM capacitors. a) top view of bottom electrode (black) and b) side view along AA' of finished capacitors with dielectrics (blue) and top electrode (grey). ....	10
Figure I.8 Aspect ratios of capacitor-over-bitline and STI structures based on data from ITRS [12]. ....	10
Figure I.9 TEM cross section of 110 nm stacked capacitor DRAM structures. Reprinted from [31] with permission from Elsevier®. ....	11

---

Figure I.10 Process flow for the formation of STI structures; a) starting with the patterned photoresist and ending with d) the fully etched STI trench. Please note: Schematics are not shown to scale. ....	12
Figure I.11 SEM micrographs of STI structures from 51 nm flash memory from Samsung for 32 (a) and 44 (b) cell structures. Taken from [36] with permission from Elsevier®. ....	13
Figure I.12 Particle (left) and post etch residue (right, courtesy of Lam Research)..	14
Figure I.13 SEM micrograph of water mark on silicon surface. Diameter is approx. 0.5 $\mu\text{m}$ . Courtesy of Lam Research.....	15
Figure I.14 Principal shapes of pattern collapse: a) no collapse, b) ruptured in the material, c) delaminated at the interface, d) bending (elastically). ....	16
Figure I.15 Pattern collapse of <110> silicon test structures. Reprinted with permission from Elsevier® [46].....	17
Figure I.16 Surface tension of typical and proposed drying liquids in the semiconductor industry.....	19
Figure I.17 DRAM capacitors with MESH structure. Reprinted with permission from Elsevier® [26]. ....	20
Figure II.1 Scheme of balanced (C) and unbalanced capillary forces in dense structures (dark) by a variation in fill height (A) or spacing (B). ....	27
Figure II.2 Horizontal component of the surface tension force.....	28
Figure II.3 Comparison of van der Waals, electrostatic, and capillary forces between two plates. ....	29
Figure II.4 The bending case of pattern collapse with the area of adhesion and the Kelvin radius. ....	29
Figure II.5 Distributed load (a) and one end load (b) model for beam mechanics. ...	31
Figure II.6 Beam deflections of ASAP and STI structures (Table 1) calculated with Euler Bernoulli beam theory (equations [22] and [23]).....	32
Figure II.7 STI structure simulated by finite element analysis using the one end load model (rotated by 90 degrees, i.e., clamped on the left, force on the right). The deformed shape is shown with the von Mises stress criterion (scale corresponds to $10^8$ Pa) and the original shape in denoted in the background. ....	33

---

Figure II.8 Maximum mechanical stress during displacement <i>done</i> of the beam with one end loading. ....	33
Figure II.9 Comparison of relevant forces during drying with the corresponding restoring forces (equation [23]) for the ASAP and STI structures. ....	34
Figure III.1 SEM micrography of line structures defined with the ASAP 300 mask. The lines are organized into sets of ten lines with different spacing per set (here: 1 $\mu\text{m}$ ). ....	37
Figure III.2 (a) Schematic cross-section through the line structures and (b) a TEM micrograph. The structure in (b) was covered with platinum for mechanical protection. TEM image courtesy of FELMI TU Graz. ....	37
Figure III.3 High magnification SEM micrographs of (a) a nominal 20 nm line and (b) of a 40 nm line. ....	38
Figure III.4 SEM micrographs of AFM tip (side view and bottom-up view).....	38
Figure III.5 Setup of AFM in liquid media (left) and cantilevers fixed to the magnetic holder ring with adhesive (right).....	39
Figure III.6 TEM brightfield image of the silicon nanoparticles. The length scale marked on the lower left corner equals 50 nm. TEM image courtesy of Technical Faculty CAU Kiel. ....	40
Figure III.7 Scheme of a rectangular cantilever with a sharp tip. ....	43
Figure III.8 AFM measurement of the pyramidal calibration structure consisting of (111) surfaces in (100) silicon. The picture is inverted for better visibility (the pyramid is actually etched into the silicon). Blue scale bar corresponds to 5 $\mu\text{m}$ . ....	46
Figure III.9 Lateral signal (approach part only) of the force distance curves on three different surfaces. The linear curve of the contact part is denoted with solid lines. ..	47
Figure IV.1 TEM bright field image of a damage induced by AFM into the line structure. The viewing plane is orientated to the side of the line structure.....	62
Figure IV.2 TEM EELS scan at the bottom of the damage. Significant material remains above the silicon oxy-nitride layer. ....	62



## Bibliography

- [1] Michael Riordan, "From Bell Labs to Silicon Valley: A Saga of Semiconductor Technology Transfer, 1955-61," *Interface*, vol. 7, no. 3, 1997.
- [2] R. N. Noyce, "Semiconductor Device-and-Lead Structure," US2981877, 1959.
- [3] J. E. Lilienfeld, "Method and apparatus for controlling electric currents," US 1745175, 1926.
- [4] Bo Lojek, *History of Semiconductor Engineering*. Berlin: Springer, 2007, vol. 1.
- [5] D. Kahng and M. M. Atalla, "Silicon-silicon dioxide field induced surface devices," in *Solid State Research Conf.*, Pittsburgh, PA, 1960.
- [6] F.M. Wanlass, "Low stand-by power complementary field effect circuitry," 3356858, 1967.
- [7] Intel. (2010, April) Intel 4004 fun facts. [Online].  
<http://www.intel.com/museum/archives/4004facts.htm>
- [8] Intel. (2010, June) 60 Years of the transistor: 1947 – 2007. [Online].  
<http://www.intel.com/technology/timeline.pdf>
- [9] Gordon E Moore, "Cramming more components into integrated circuits," *Electronics*, vol. 38, no. 6, 1965.
- [10] Gordon E. Moore, "Progress in Digital Integrated Electronics," in *International Electron Devices Meeting*, 1975, p. 11.

- [11] Scott E. Thompson and Srivatsan Parthasarathy, "Moore's law: the future of Si microelectronics," *Materials today*, vol. 9, no. 6, p. 20, 2006.
- [12] ITRS, *International Technology Roadmap for Semiconductors: Front End Processes.*: www.itrs.net, 2007.
- [13] Laszlo B. Kish, "End of Moore's law: thermal (noise) death of integration in micro and nano electronics," *Phys. Lett. A*, vol. 305, p. 144, 2002.
- [14] Minoru Sugawara, Akira Chiba, Hiromasa Yamanashi, Hiroaki Oizumi, and Iwao Nishiyama, "Attenuated phase-shift mask for line patterns in EUV lithography," *Microelectron. Eng.*, vol. 67-68, p. 10, 2003.
- [15] Julius Santillan et al., "A study of 193-nm immersion lithography using novel high refractive index fluids," *Microelectron. Eng.*, vol. 83, p. 651, 2006.
- [16] M. C. Chiu et al., "Challenges of 29nm Half-Pitch NAND FLASH STI Patterning with 193nm Dry Lithography and Self-Aligned Double Patterning," *Proc. of SPIE*, vol. 7140, p. 714021, 2008.
- [17] Robert Chau et al., "Application of high- $\kappa$  gate dielectrics and metal gate electrodes to enable silicon and non-silicon logic nanotechnology," *Microelectron. Eng.*, vol. 80, p. 1, 2005.
- [18] R. H. Dennard, "Field-Effect Transistor Memory," US3387286, 1968.
- [19] Juergen W. Faul and Dietmar Henke, "Transistor challenges - A DRAM perspective," *Nucl. Instrum. Meth. B*, vol. 237, p. 228, 2005.
- [20] Kinan Kim, "Technology for sub-50nm DRAM and NAND flash manufacturing," in *IEDM Technical Digest.* , 2005, p. 323.
- [21] Eric Gerritsen et al., "Evolution of materials technology for stacked-capacitors in 65 nm embedded-DRAM," *Solid-State Electronics*, vol. 49, p. 1767, 2005.
- [22] Fujio Masuoka, "Semiconductor Integrated Circuit Device with Low Power Consumption in Standby Mode Using an On-Chip Substrate Bias Generator,"

4460835, 1984.

- [23] Intel corp., "Intel StrataFlash™ Memory Technology Overview," *Intel Technology Journal*, vol. Q4, 1997.
- [24] Roberto Bez, Emilio Camerlenghi, Alberto Modelli, and Angelo Visconti, "Introduction to Flash Memory," *Proceedings of the IEEE*, vol. 91, no. 4, 2003.
- [25] Roberto Bez and Emilio Camerlenghi, "Flash Memory Technology Evolution," in *ULSI Process Integration III*, Pennington, New Jersey, 2003, p. 136.
- [26] Kinan Kim and S. Y. Lee, "Memory technology in the future," *Microelectron. Eng.*, vol. 84, p. 1976, 2007.
- [27] Chih-Yuan Lu, Kuang-Yeu Hsieh, and Rich Liu, "Future challenges of flash memory technologies," *Microelectron. Eng.*, vol. 86, p. 283, 2009.
- [28] J. Postel-Pellerin et al., "Extraction of 3D parasitic capacitances in 90 nm and 22 nm NAND flash memories," *Microelectron. Reliab.*, vol. 49, p. 1056, 2009.
- [29] Sherif A. Tawfik and Volkan Kursun, "FinFET domino logic with independent gate keepers," *Microelectr J*, vol. 40, p. 1531, 2009.
- [30] Cheol Seong Hwang, "(Ba,Sr)TiO<sub>3</sub> thin films for ultra large scale dynamic random access memory. A review on the process integration," *Mat. Sci. Eng. B-Solid*, vol. 56, p. 178, 1998.
- [31] Seong-Goo Kim et al., "Fully integrated 512 Mb DRAMs with HSG-merged-AHO," *Solid-State Electronics*, vol. 50, p. 1030, 2006.
- [32] Roger H French and Hoang V Tran, "Immersion Lithography: Photomask and Wafer-Level Materials," *Annu. Rev. Mater. Res.*, vol. 39, p. 93, 2009.
- [33] Franz Laermer and Andrea Schilp, "Method of Anisotropically Dry Etching," US 5501893, 1996.
- [34] C. J. D. Craigie et al., "Polymer thickness effects on Bosch etch profiles," *J. Vac. Sci. Technol. B*, vol. 20, no. 6, p. 2229, 2002.

- [35] Anchuan Wang et al., "Extending HDP for STI Fill to 45nm with IPM," in *ISSM*, 2007, p. 247.
- [36] Tao-Kyung Kim, Sungnam Chang, and Jeong-Hyuk Choi, "Floating gate technology for high performance 8-level 3-bit NAND flash memory," *Solid-State Electronics*, vol. 53, p. 792, 2009.
- [37] W P Eaton and J H Smith, "Micromachined pressure sensors: review and recent developments," *Smart Mater. Struct.*, vol. 6, p. 530, 1997.
- [38] L. J. Hornbeck, "Digital Light Processing™ for High-Brightness, High-Resolution Applications," in *Electronic Imaging, EI '97, Projection Displays III*, San Jose, CA, 1997.
- [39] R Hopkins et al., "The silicon oscillating accelerometer: A MEMS inertial instrument for strategic missile guidance," in *AIAA Missile Sciences Conference*, 1998, p. P3804.
- [40] J. C. Eloy, E. Mounier, and P. Roussel, "Status of the Inertial MEMS-based Sensors in the Automotive," in *Advanced Microsystems for Automotive Applications*. Berlin Heidelberg: Springer, 2005, ch. 1, p. 43.
- [41] W Kern and D. A. Puotinen, "Cleaning solutions based on hydrogen peroxide for use in silicon semiconductor technology," *RCA Rev.*, vol. 31, p. 187, 1970.
- [42] Harumi Matsuzaki, Isao Ookouchi, Hideaki Kurokawa, Katsuya Ebara, and Sankichi Takahashi, "A Study of the Formation of Water Marks from Membrane-Distilled Water and Ultrapure Water," *J. Chem. Eng. Jpn.*, vol. 21, no. 5, p. 490, 1988.
- [43] Hiromitsu Namba, Takehiko Orii, Hiroki Ohno, and Glenn W. Gale, "Insights into Watermark Formation and Control," *Solid State Phenomena*, vol. 103-104, p. 83, 2005.
- [44] Katsuhiko Miya, Takuya Kishimoto, and Akira Izumi, "Effective Rinse Aiming at Water-Mark-free Drying for single-spin Wet Cleaning Process," *Solid State Phenomena*, vol. 103-104, p. 79, 2005.

- [45] Y.K. Park et al., "Effective Capacitance Enhancement Methods for 90-nm DRAM Capacitors," *J. Korean Phys. S.*, vol. 44, no. 1, p. 112, 2004.
- [46] Hideo Namatsu, Kenji Yamazaki, and Kenji Kurihara, "Supercritical Drying for Nanostructure Fabrication without Pattern collapse," *Microelectron. Eng.*, vol. 46, p. 129, 1999.
- [47] Toshihiko Tanaka, Mitsuaki Morigami, and Nobufumi Atoda, "Mechanism of Resist Pattern Collapse during Development Process," *Jpn. J. Appl. Phys.*, vol. 32, no. 12B, p. 6059, 1993.
- [48] Heidi B. Cao, Paul F. Nealey, and Wolf-Dieter Domke, "Comparison of resist collapse properties for deep ultraviolet and 193nm resist platforms," *J. Vac. Sci. Technol. B*, vol. 18, no. 6, p. 3303, 2000.
- [49] Toshihiko Tanaka, Mitsuaki Morigami, and Nobufumi Atoda, "Mechanism of Resist Pattern Collapse," *Journal of the Electrochemical Society*, vol. 140, no. 7, p. L115, 1993.
- [50] Sang-Kon Kim, "Pattern Collapse for Nanoline Formation," *J. Korean Phys. Soc.*, vol. 42, p. 371, 2004.
- [51] Hyung-Joo Lee, Jun-Taek Park, Ji-Yong Yoo, Il-sin An, and Hye-Keun Oh, "Resist Pattern Collapse Modeling for Smaller Features," *J. Korean Phys. Soc.*, vol. 42, p. S202, 2003.
- [52] Sang-Hu Park, Kwang Ho Kim, Tae Woo Lim, Dong-Yol Yang, and Kwang-Sup Lee, "Investigation of three-dimensional pattern collapse owing to surface tension using an imperfection finite element model," *Microelectron. Eng.*, vol. 85, p. 432, 2008.
- [53] Alexandre Chau, Stiphane Rignier, Alain Delchambre, and Pierre Lambert, "Three-dimensional model for capillary nanobridges and capillary forces," *Modelling Simul. Mater. Sci. Eng.*, vol. 15, p. 305, 2007.
- [54] M. Kotera and N. Ochiai, "Three-dimensional simulation of resist pattern deformation by surface tension at the drying process," *Microelectron. Eng.*, vol.

- 78-79, p. 515, 2005.
- [55] Kimiyoshi Deguchi, Kazunori Miyoshi, Tetsuyoshi Ishii, and Tadahito Matsuda, "Patterning Characteristics of a Chemically-Amplified Negative Resist in Synchrotron Radiation Lithography," *Jpn. J. Appl. Phys.*, vol. 31, no. 9A, p. 2954, 1992.
- [56] Akira Kawai and Yoshihisa Kaneko, "Analysis of Resist Pattern Collapse by Direct Peeling Method with Atomic Force Microscope Tip," *Jap. J. Appl. Phys.*, vol. 39, no. 3A, p. 1426, 2000.
- [57] Akira Kawai, "Collapse Behavior of KrF Resist Line Pattern Analyzed with Atomic Force Microscope Tip," *Jap. J. Appl. Phys.*, vol. 39, no. 12B, p. 7044, 2000.
- [58] Sung-Kyoung Kim, Myoung-Ho Jung, Hyung-Woo Kim, Sang-Gyun Woo, and Haiwon Lee, "Measurement of the strength of adhesion of resist patterns using an atomic force microscope," *Nanotechnology*, vol. 16, p. 227, 2005.
- [59] Akira Kawai and Norio Moriike, "Analysis of pattern collapse of ArF excimer laser resist by direct peeling method with atomic force microscope tip," *Microelectron. Eng.*, vol. 2001, p. 683, 2001.
- [60] Bettina Baumeister, Thomas A. Jung, and Ernst Meyer, "Nanoscale fracture studies using the scanning ofrce microscope," *Appl. Phys. Lett*, vol. 78, no. 17, p. 2485, 2001.
- [61] B Baumeister, T. A. Jung, and E. Meyer, "Tribological studies on fracture and erosion of nanostructures," *Tribol. Lett.*, vol. 11, no. 2, p. 107, 2001.
- [62] Bettina Baumeister, *PhD thesis: Elementare Prozesse der Nanotribologie in Rasterkraftmikroskopieexperimenten*. Basel: Universität Basel, 2001.
- [63] C. H. Mastrangelo and C. H. Hsu, "Mechanical Stability and Adhesion of Microstructures Under Capillary Forces - Part I: Basic Theory," *J. Microelectromech. S.*, vol. 2, no. 1, p. 33, 1993.

- [64] C. H. Mastrangelo and C. H. Hsu, "Mechanical Stability and Adhesion of Microstructures Under Capillary Forces - Part II: Experiments," *J. Microelectromech. S.*, vol. 2, no. 1, p. 44, 1993.
- [65] Rob Legtenberg, Harrie A. C. Tilmans, Job Elders, and Miko Elwenspoek, "Stiction of surface micromachined structures after rinsing and drying: model and investigation of adhesion mechanisms," *Sensors and Actuators A*, vol. 43, p. 239, 1994.
- [66] R. L. Alley, R. T. Howe, and K. Komvopoulos, "The effect of release-etch processing on surface microstructure stiction," in *Proc. of the IEEE Solid-State Sensor and Actuator Workshop*, Hilton Head, SC, USA, 1992, p. 202.
- [67] K. Komvopoulos, "Surface engineering and microtribology for microelectromechanical systems," *Wear*, vol. 200, p. 305, 1996.
- [68] A. Torii, M. Sasaki, K. Hane, and S. Oluma, "Adhesive force of the microstructures measured by the atomic force microscope," in *Proc. IEEE Micro Electro Mechanical Systems*, Fort Lauderdale, FL, USA, 1993, p. 111.
- [69] Niels Tas, Tonny Sonnenberg, Henri Jansen, Rob Legtenberg, and Miko Elwenspoek, "Stiction in surface micromachining," *J. Micromech. Microeng.*, vol. 6, p. 385, 1996.
- [70] Roya Maboudian and Roger T. Howe, "Critical Review: Adhesion in surface micromechanical structures," *J. Va. Sci. Technol. B*, vol. 15, p. 1, 1997.
- [71] Yoshio Yamashita, "Sub-0.1  $\mu\text{m}$  Patterning with High Aspect Ratio of 5 Achieved by Preventing Pattern Collapse," *Jap. J. Appl. Phys.*, vol. 35, no. 4A, p. 2385, 1996.
- [72] Ye Jincao, Michael A. Matthews, and Charles H. Darwin, "Prevention of Photoresist Pattern Collapse Using Liquid Carbon Dioxide," *Ind. Eng. Chem. Res.*, vol. 40, no. 24, p. 5858, 2001.
- [73] Hideo Namatsu, "Supercritical Drying for Nanostructure Fabrication," *Journal of Photopolymer Science and Technology*, vol. 15, no. 3, p. 381, 2002.

- [74] Gina L. Weibel and Christopher K. Ober, "An overview of supercritical CO<sub>2</sub> applications in microelectronics processing," *Microelectron. Eng.*, vol. 65, p. 145, 2003.
- [75] Toshihiko Tanaka et al., "Prevention of Resist Pattern Collapse by Resist Heating during Rinsing," *J. Electrochem. S.*, vol. 141, no. 12, p. L169, 1994.
- [76] Jong-Sun Kim, Wook Chang, Ilsin An, and Hye-Keun Oh, "32 nm Pattern Collapse Modeling with Radial Distance and Rinse Speed," *Jpn. J. Appl. Phys.*, vol. 46, no. 8A, p. 5101, 2007.
- [77] Jacob Israelachvili, *Intermolecular & Surface Forces*, 2nd ed. London: Elsevier Ltd, 1991.
- [78] G. A. C. M. Spierings, J. Haisma, and T. M. Michielsen, "Surface-related phenomena in the direct bonding of silicon and fused-silica wafer pairs.," *Philips J. Res.*, vol. 49, p. 47, 1995.
- [79] Yury Gogotsi, Joseph A. Libera, Almila Güvenc-Yazicioglu, and Constantine M. Megaridis, "In situ multiphase fluid experiments in hydrothermal carbon nanotubes," *Appl. Phys. Lett.*, vol. 79, no. 7, p. 1021, 2001.
- [80] Hans-Jürgen Butt and Michael Kappl, *Surface and Interfacial Forces.*: Wiley-VCH, 2010.
- [81] S. Farshid Chini and A. Amirfazli, "Understanding Pattern collapse in Photolithography Process Due to Capillary Forces," *Langmuir*, vol. 26, no. 16, p. 13707, 2010.
- [82] Ioffe Physico-Technical Institute. (2010, July) New Semiconductor Materials. Characteristics and Properties. [Online]. <http://www.ioffe.ru/SVA/NSM/>
- [83] D. Maugis, *Contact, Adhesion and Rupture of Elastic Solids*. Heidelberg, Germany: Springer, 2000.
- [84] W. N. Sharpe, K. T. Turner, and R. L. Edwards, "A new technique for measuring the mechanical properties of thin films," *Exp. Mech.*, vol. 39, no. 3, p.



---

162, 1999.

- [85] J. Koskinen, J. E. Steinwall, R. Soave, and H. H. Johnson, "Microtensile testing of free-standing polysilicon fibers of various grain sizes," *J. Micromech. Microeng.*, vol. 3, p. 13, 1993.
- [86] C. L. Muhlstein, S. B. Brown, and R. O. Ritchie, "High-Cycle Fatigue of Single-Crystal Silicon Thin Films," *J. Microelectromech. S.*, vol. 10, no. 4, p. 593, 2001.
- [87] J. Olivares-Roza, O. Sanchez, and J. M. Albella, "Plasma assisted chemical vapor deposition silicon oxynitride films grown from SiH<sub>4</sub>+NH<sub>3</sub>+O<sub>2</sub> gas mixtures," *J. Vac. Sci. Technol. A*, vol. 16, no. 5, p. 2757, 1998.
- [88] M. Morita, T. Ohmi, E. Hasegawa, M. Kawakami, and M. Ohwada, "Growth of native oxide on a silicon surface," *J. Appl. Phys.*, vol. 68, p. 1272, 1990.
- [89] David R Linde, *Handbook of Chemistry and Physics*, 75th ed. London: CRC Press, 1994.
- [90] Gösta Akerlöf, "Dielectric constants of some organic solvent-water mixtures at various temperatures," *J. Am. Chem. Soc.*, vol. 54, no. 11, p. 4125, 1932.
- [91] Jin-Goo Park et al., "Interfacial and Electrokinetic Characterization of IPA Solutions Related to Semiconductor Wafer Drying and Cleaning," *J. Electrochem. Soc.*, vol. 153, no. 9, p. G811, 2006.
- [92] Sean X. Liu and Jun-Tae Kim, "Study of adsorption kinetics of surfactants onto polyethersulfone membrane surface using QCM-D," *Desalination*, vol. 247, p. 355, 2009.
- [93] Zhichu Bi, Wensheng Liao, and Liyun Qi, "Wettability alteration by CTAB adsorption at surfaces of SiO<sub>2</sub> film or silica gel powder and mimic oil recovery," *Applied Surf. Sci.*, vol. 221, p. 25, 2004.
- [94] Edward W. Washburn et al., Eds., *International critical tables of numerical data, physics, chemistry and technology*. New York: National research council by McGraw-Hill Company, Inc., 1928, vol. 4.

- [95] Massimo Migliori, Domenico Gabriele, Bruno de Cindio, and Sebastiano Corra, "Viscosity of Multicomponent Solutions of Simple and Complex Sugars in Water," *J. Chem. Eng. Data*, vol. 52, p. 1347, 2007.
- [96] Michael Van Sint Jan, Marcelo Guarini, Andrés Guesalaga, J. Ricardo Pérez-Correa, and Yolanda Vargas, "Ultrasound based measurements of sugar and ethanol concentrations in hydroalcoholic solutions," *Food Control*, vol. 19, p. 31, 2008.
- [97] M. Dominguez, C. Lafuente, M. C. Lopez, F. M. Royo, and J. S. Urieta, "Speed of sound and isentropic compressibility of (1-butanol + n-hexane + 1-chlorobutane) and the constituent binary mixtures at the temperatures 298.15 K and 313.15 K," *J. Chem. Thermodynamics*, vol. 32, p. 155, 2000.
- [98] J. Rodriguez-Carvajal, Fullprof.2k, and Version 4.6c - Mar 2002, *Physica B*, vol. 55, p. 192, 1993.
- [99] David B. Asay and Seong H. Kim, "Direct force balance method for atomic force microscopy lateral force calibration," *Rev. Sci. Instrum.*, vol. 77, p. 043903, 2006.
- [100] Manuel L.B. Palacio and Bharat Bhushan, "Normal and Lateral Force Calibration Techniques for AFM Cantilevers," *Crit. Rev. Solid State*, vol. 35, p. 73, 2010.
- [101] Martin Munz, "Force calibration in lateral force microscopy: a review of the experimental methods," *J. Phys. D: Appl. Phys.*, vol. 43, p. 063001, 2010.
- [102] John Elie Sader, "Frequency response of cantilever beams immersed in viscous fluids with applications to the atomic force microscope," *J. Appl. Phys.*, vol. 84, no. 1, p. 64, 1998.
- [103] J. L. Hutter and J. Beckhoefer, "Calibration of atomic force microscope tips," *Rev. Sci. Instrum.*, vol. 64, p. 1868, 1993.
- [104] David-A Mendels et al., "Dynamic properties of AFM cantilevers and the calibration of their spring constants," *J. Micromech. Microeng.*, vol. 16, p. 1720,

2006.

- [105] Christopher P. Green et al., "Normal and torsional spring constants of atomic force microscope cantilevers," *Rev. Sci. Instrum.*, vol. 75, no. 6, p. 1988, 2004.
- [106] E. Liu, B. Blanpain, and J. P. Celis, "Calibration procedures for frictional measurements with a lateral force microscope," *Wear*, vol. 192, p. 141, 1996.
- [107] Rachel J. Cannara, Michael Eglin, and Robert W. Carpick, "Lateral force calibration in atomic force microscopy: A new lateral force calibration method and general guidelines for optimization," *Rev. Sci. Instrum.*, vol. 77, p. 053701, 2006.
- [108] Dukhyun Choi, Woonbong Hwang, and Euisung Yoon, "Improved lateral force calibration based on the angle conversion factor in atomic force microscopy," *Journal of Microscopy*, vol. 228, no. 2, p. 190, 2007.
- [109] Peter J. Cumpson, John Hedley, and Charles A. Clifford, "Microelectromechanical device for lateral force calibration in the atomic force microscope: Lateral electrical nanobalance," *J. Vac. Sci. Technol. B*, vol. 23, no. 5, p. 1992, 2005.
- [110] Q. Li, K.-S. Kim, and A. Rydberg, "Lateral force calibration of an atomic force microscope with a diamagnetic levitation spring system," *Rev. Sci. Instrum.*, vol. 77, p. 065105, 2006.
- [111] D. F. Ogletree, R. W. Carpick, and M. Salmeron, "Calibration of frictional forces in atomic force microscopy," *Rev. Sci. Instrum.*, vol. 67, no. 9, p. 3298, 1996.
- [112] M. Varenberg, I. Etsion, and G. Halperin, "An improved wedge calibration method for lateral force in atomic force microscopy," *Rev. Sci. Instrum.*, vol. 74, no. 7, p. 3362, 2003.
- [113] David B. Asay, Erik Hsiao, and Seong H. Kim, "Corrected direct force balance method for atomic force microscopy lateral force calibration," *Rev. Sci. Instrum.*, vol. 80, p. 066101, 2009.

- [114] L. A. Giannuzzi et al., "FIB Lift-Out Specimen Preparation Techniques - Ex-Situ and In-Situ Methods," in *Introduction to Focused Ion Beams.*: Springer US, 2005, ch. 10.
- [115] F. J. Himpsel, F. R. McFeely, A. Taleb-Ibrahimi, J. A. Yarmoff, and G. Hollinger, "Microscopic structure of the SiO<sub>2</sub>/Si interface," *Phys. Rev. B*, vol. 38, no. 9, p. 6084, 1988.
- [116] E. Lippmaa, M. Mägi, A. Samoson, G. Engelhardt, and A.-R. Grimmer, "Structural Studies of Silicates by Solid-State High-Resolution <sup>29</sup>Si NMR," *J. Am. Chem. Soc.*, vol. 102, p. 4889, 1980.
- [117] E. O. Stejskal and J. D. Memory, *High Resolution NMR in the Solid State: Fundamentals of Cp/Mas*. Oxford: Oxford University Press, Inc., 1994.
- [118] Stefan A. Pelster, Rainer Kalamajka, Wolfgang Schrader, and Ferdi Schüth, "Monitoring the Nucleation of Zeolites by Mass Spectrometry," *Angew. Chem.*, vol. 119, p. 2349, 2007.
- [119] Stefan A. Pelster, Wolfgang Schrader, and Ferdi Schüth, "Monitoring Temporal Evolution of Silicate Species during Hydrolysis and Condensation of Silicates Using Mass Spectrometry," *J. Am. Chem. Soc.*, vol. 128, p. 4310, 2006.
- [120] Bernd Bastian Schaack, Wolfgang Schrader, and Ferdi Schüth, "Detection of Structural Elements of Different Zeolites in Nucleating Solutions by Electrospray Ionization Mass Spectrometry," *Angew. Chem.*, vol. 120, p. 9232, 2008.
- [121] Yu Ya Meshkov, "Griffith energy criterion in the fracture micro- and macromechanics of brittle bodies," *Metall Science and Heat Treatment*, vol. 38, p. 28, 1996.

# Curriculum Vitae

## Personal

Name Daniel PETER  
Date of birth June 29<sup>th</sup>, 1984 in Hemau  
Family status single

## Education

Since Oct. 2006 **Christian-Albrechts-Universität zu Kiel**  
PhD student in the department of inorganic chemistry  
(Prof. Dr. W. Bensch)

Oct. 2002 – Sep. 2006 **University of Applied Sciences Regensburg**  
Microsystems engineering with the degree of Dipl. Ing. (Fh)

Sep. 2000 – Sep. 2002 **Staatliche Fachoberschule Regensburg**  
Direction of science

## Professional Experience

Since Oct. 2006 **Lam Research AG (formerly SEZ AG)**  
PhD student with the topic of pattern collapse during  
semiconductor device manufacturing.

Mar. 2006 – Sep. 2006 **OSRAM Opto Semiconductors GmbH**  
Diploma thesis on the measurement and simulation of the ESD  
stability of optoelectronic devices.